Aircraft Stall Dynamics

Improved Longitudinal Stall Modeling with Separable Nonlinear Least Squares and Dynamic Stall Maneuvers

Joey A. Herbold

TU Delft

Aircraft Stall Dynamics

Improved Longitudinal Stall Modeling with Separable Nonlinear Least Squares and Dynamic Stall Maneuvers

Thesis report

by

Joey A. Herbold

to obtain the degree of Master of Science
at the Delft University of Technology
to be defended publicly on January 24, 2025 at 13:00

Thesis committee:

Chair:	Dr. Ir. D.M. Pool
Supervisor:	Dr. Ir. C.C. de Visser
External examiner:	Dr. Ir. B.W. van Oudheusden
Place:	Faculty of Aerospace Engineering, Delft
Project Duration:	March, 2024 - January, 2025
Student number:	4838351

An electronic version of this thesis is available at `http://repository.tudelft.nl/`.

Faculty of Aerospace Engineering · Delft University of Technology

Preface

This is the final result of six and a half years in Delft, of which the last year was spent on this project. Where aerospace engineering started for me as a way to challenge myself, it turned into a passion. Who would have thought six years ago that I would open FlightRadar anytime a plane passes over?

About a year ago in December 2023, I approached Coen for a thesis topic. After he told me about the stall task force, I knew this would be an exciting journey. A journey that has been ten years in the making. My first gratitude goes out to my predecessors in the stall task force. What did Newton say again? Standing on the shoulders of giants. I could not have achieved the outcome of this research without the people who came before me.

Next, I want to thank Coen and Daan for their input during the bi-weekly stall meetings. These meetings helped me stay grounded when results were too good to be true, or motivated me when results were bad. You provided me with great feedback that helped me shape this research project.

About five months into the project, I asked Menno, if I could see the aircraft at the hangar in Rotterdam. During my time at the hangar, I had the opportunity to see the aircraft from every angle, inside and out. I talked to Fred and Menno, the aircraft technicians, who were happy to take time out of their day to answer my questions. That day, was the first moment I realized the stall strips might have an effect. Although a regular day for Fred and Menno, it was a special day for the research project. Thanks for all your input during this project!

During the project, I had the pleasure of conducting two flight tests. These tests would not have been possible without the help of Hans and Xander. I want to thank you for your eagerness to help during the design phase of the test flights. Your enthusiasm puts into perspective how special it is that we can conduct this research. I also want to thank you, alongside Tjipke, for flying the aircraft during the tests.

I could count on many other people around the flights. Thank you, Andries, for helping me out with a GoPro. I want to thank Ferdinand for his help in extracting the data from the aircraft, as well as providing other data necessary for analysis. Furthermore, I want to thank Pietro, who is also part of the stall task force, for his input during the preparation of the flights and his help during the flight.

Working on a project alone for an entire year is an incredibly lonely endeavor. But apparently, it is a rite of passage for aerospace engineers. I am very grateful for the people who shared this journey with me. Special thanks to Aman, Korneel, and Ole, it is almost poetic that we are all graduating within a month. I also want to thank the other people who were in SIM0.04 over the past months, thank you for the support, fun coffee breaks, and lunches in the sun.

Lastly, I want to thank my girlfriend and family for their love and support during this challenging and time-intensive part of my studies. As this chapter closes, I am looking forward to spending more time with you again. I couldn't have achieved this without you!

Joey Herbold
Delft, December 15, 2024

Contents

Nomenclature

List of Abbreviations

BEW	Basic Empty Weight
DLR	German Aerospace Center Deutsches Zentrum für Luft- und Raumfahrt
DSV	Dynamic Stall Vortex
EASA	European Union Aviation Safety Agency
FAA	Federal Aviation Administration
IATA	International Air Transport Association
ICAO	International Civil Aviation Organization
ICATEE	International Committee for Aviation Training in Extended Envelopes
KKT	Karush-Kuhn-Tucker
LOC-I	Loss of Control In-flight
MAC	Mean Aerodynamic Chord
MSE	Mean Square Error
NASA	National Aeronautics and Space Administration
NLR	Netherlands Aerospace Center
OLS	Ordinary Least Squares
QR	Quasi-random
SNLS	Separable Nonlinear Least Squares
SUPRA	Simulation of Upset Recovery in Aviation
TU Delft	Delft University of Technology Technische Universiteit Delft
UPRT	Upset Prevention and Recovery Training

List of Symbols

α	Angle of attack
α^*	Stall separation parameter
β	Angle of sideslip
$\boldsymbol{\Phi}$	Nonlinear regression matrix
$\boldsymbol{\theta}$	Nonlinear parameters
$\boldsymbol{b}$	Barycentric coordinates
$\boldsymbol{c}$	Linear parameters
$\boldsymbol{D}$	Frechet derivative
$\boldsymbol{x}$	Cartesian coordinates
δ_a	Aileron deflection angle
δ_e	Elevator deflection angle
δ_r	Rudder deflection angle
Γ	Smoothness matrix null-space
Λ	Auto-correlation matrix
λ	Auto-correlation sequence
τ_1	Stall time lag parameter
τ_2	Stall hysteresis parameter
$\mathcal{T}$	Triangulation
a_1	Stall abruptness parameter
b	Wing span
c	B-coefficients
c	Chord length
C_c	Chordwise force coefficient
C_D	Drag coefficient
C_L	Lift coefficient
C_l	Roll moment coefficient
C_m	Pitch moment coefficient
C_N	Normal force coefficient
C_n	Yaw moment coefficient
C_X	Longitudinal force coefficient
C_Y	Side force coefficient

C_Z	Normal force coefficient (aircraft)
$C_{\hat{\theta}}$	Parameter covariance matrix
H	Smoothness matrix
$P^{\perp}_{\mathbf{\Phi}(\boldsymbol{\theta})}$	Projector onto the orthogonal complement of the column space of $\mathbf{\Phi}(\boldsymbol{\theta})$
S	Wing area
t	Simplex
u	Wind component x-direction
v	Vertex
v	Wind component y-direction
w	Wind component z-direction
X	Flow separation parameter
X_0	Static flow separation parameter
y_w	Spanwise wing center of pressure

List of Figures

List of Tables

Part I

Literature Review & Research Definition

1

General Introduction

Loss of control in-flight (LOC-I) remains a critical safety concern in aviation, responsible for a majority of fatal accidents over the past decades [1, 2, 3, 4]. LOC-I occurs when a pilot is unable to maintain control and the aircraft deviates from its intended flight path. Stalls have been shown to be a common precursor to LOC-I incidents [5, 6, 7]. If not correctly recognized, a stall can escalate into a more severe upset. Therefore, recognition is seen as a fundamental aspect of accident prevention [8]. The critical nature of stall recognition in LOC-I scenarios underscores the importance of effective upset prevention and recovery training (UPRT). Training goals have been put forward by the International Committee for Aviation Training in Extended Envelopes (ICATEE) [9] and are adopted by ICAO, FAA and EASA [10, 11, 12]. Analysis of training goals showed that it is necessary to improve the aerodynamic models in stall regimes for flight simulator training devices [13].

Two methods exist for the creation of stall models. The first is based on extensive wind tunnel testing and CFD analysis, for example, the simulation of upset recovery in aviation (SUPRA) project [14]. These projects are expensive due to the high complexity and extensive use of wind tunnels. Alternatively, identification methods are used on flight test data. Stall model identification has been extensively researched at different research institutes and universities, such as the German Aerospace Center (DLR) [15, 16, 17, 18], NASA [19], the Flight Test and Research Institute of the Brazilian Air Force [20, 21], and Delft University of Technology (TU Delft) [22, 23, 24, 25, 26, 27, 28, 29].

Specifically in Delft, a system identification workflow has been created for the creation of stall models of the Cessna Citation II. A longitudinal stall model was created by Van Ingen [23] and an asymmetric stall model by De Fuijk [29]. Both methods use a combination of linear models for the aerodynamic coefficients and an embedded separation state that depends on a nonlinear model.

This thesis builds upon the existing system identification workflow by improving the nonlinear parameter optimization process. The primary objective of this research is to enhance the Citation II aerodynamic stall models by developing a more efficient nonlinear system identification routine. It does so by exploring the use of separable nonlinear least squares to reduce computational complexity.

This thesis is organized as follows: Part I presents the initial research phase, in which a literature review is performed and the scope of the research is defined. Part II is the result of this thesis, a scientific article contributing to safer flight, by proposing improved methods to create stall models. Further research elements, beyond the scope of the paper are discussed in Part III. Lastly, a reflection on the work and recommendations for future work is given in Part IV.

2

Literature Review

This chapter covers the relevant literature used as a starting point for the work in this thesis. The relevance of stall modeling is introduced in Section 2.1. Information on the test vehicle, available data, and data preprocessing is provided in Section 2.2. A background of stall and its modeling is covered in Section 2.3. In Section 2.4, the multivariate simplex spline is introduced. Lastly, Section 2.5 covers separable nonlinear least squares which is a special variant of nonlinear least squares that will be used in this thesis.

2.1. Stall Modeling Relevance

LOC-I remains a critical safety concern in aviation, responsible for a majority of fatal accidents over the past decades [1, 2]. LOC-I occurs when an aircraft deviates from its intended flight path and the pilot is unable to regain control, resulting in a crash. This category of accidents includes situations such as stalls, spins, and unintentional maneuvers that place the aircraft outside its normal flight envelope.

From 2013 to 2022, LOC-I accidents accounted for the most crash-related fatalities compared to other causes like controlled flight into terrain or runway excursions [3]. The International Air Transport Association reports that LOC-I incidents have been the most severe, giving passengers the lowest chance of surviving such accidents [4]. These incidents are often linked to poor pilot response to unusual flight conditions and failures in preventing or recovering from stalls and other aerodynamic upsets [30, 31].

Stalls are a common precursor to LOC-I incidents [8, 5, 6, 7]. A stall occurs when the aircraft's angle of attack increases beyond a critical point, leading to a loss of lift due to flow separation [32]. If not correctly recognized, a stall can escalate into a more severe upset, therefore, recognition is seen as a fundamental aspect of accident prevention [8]. The critical nature of stall recognition in LOC-I scenarios underscores the importance of effective UPRT.

UPRT is designed to address skill deficiencies identified in LOC-I accidents [9]. The training objectives have been established by ICATEE [13] and adopted by ICAO in the Manual on Aeroplane Upset Prevention and Recovery Training [10]. Furthermore, the American and European flight authorities amended their pilot training requirements to reflect the same [11, 12].

In an analysis of current state-of-the-art simulator capabilities, 56% of the training objectives were found to be achievable. However, 26% of tasks require upgraded Level D / Type 7 simulators. These enhancements should be made to the instructor station, stall buffet models and post-stall aerodynamics models [13]. This research aims to take further steps in improving post-stall aerodynamic modeling.

2.2. Flight Experiments

At different research institutes flight test experiments have been performed to study aircraft stall. Most notably are the German Aerospace Center (DLR) [15, 16, 17, 18], NASA [19], the Flight Test and Research Institute of the Brazilian Air Force [20, 21], and TU Delft [22, 23, 24, 25, 26, 27, 28, 29]. In this section, past experiences of stall modeling in Delft are discussed specifically. This is done by introducing the flight vehicle in Subsection 2.2.1. Then, in Subsection 2.2.2 the past flight tests are summarized. Lastly, the concept of flight path reconstruction is introduced in Subsection 2.2.3, which is an integral part of the data preprocessing.

2.2.1. Flight Test Vehicle

The PH-LAB, a Cessna Citation II, is a flight test vehicle jointly owned by TU Delft and the Netherlands Aerospace Center (NLR). The aircraft is used for academic and research purposes. It is outfitted with a modern fly-by-wire system and multiple data collection systems. The aircraft schematics can be found in Fig. 2.1. The aircraft's general dimensions, mass, and inertia properties can be found in Table 2.1. Information on the installed data collection systems is listed in Table 2.2. The most notable instrument is the air-data boom installed that measures the angle of attack and sideslip. This is the flight vehicle modeled in this research.

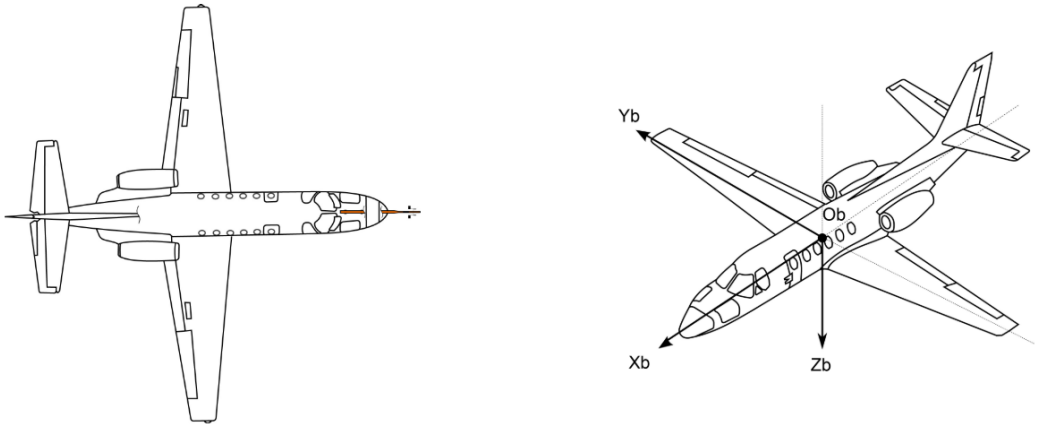

Figure 2.1: Schematic views of the PH-LAB, including the body-fixed reference frame axes definition. The left schematic also illustrates the installed air data boom. (adapted from [23])

Table 2.1: PH-LAB dry mass and dimensions (adapted from [23])

Dimensions		Mass and Inertia	
b	15.9	m	4,157 kg
$\bar{c}$	2.09 m	I_{xx}	12,392 kgm^2
S	30.0 m^2	I_{yy}	31,501 kgm^2
		I_{zz}	41,908 kgm^2
		I_{xz}	2,252.2 kgm^2

Table 2.2: List of flight test equipment installed in the Cessna Citation II aircraft PH-LAB including the variables they measure, which are relevant to this research (adapted from [23])

Name	Explanation	Measures	Variables	Units
GPS	Global Positioning System	Position in F_E	x_E, y_E, z_E	m
		Velocity in F_E	$\dot{x}_E$, $\dot{y}_E$, $\dot{z}_E$	m/s
DADC	Digital Air-Data Computer	Total airspeed	V_{TAS}	m/s
AHRS	Attitude and Heading Reference System	Aircraft attitude	ϕ, θ, ψ	rad
		Body rotation rates	p, q, r	rad/s
		Body specific forces	A_x, A_y, A_z	m/s^2
Synchro	Angle Measurements	Contr.surf.defl	δ_a, δ_e, δ_r	rad
Boom	Air data boom	Air incidence angle	α, β	rad

2.2.2. Stall Database

Over the years, the stall research group at TU Delft performed multiple stall tests. These tests were performed using the flight vehicle discussed in Subsection 2.2.1. This chapter provides an overview of these tests.

- **2015 stall data**: The first stall dataset was obtained through test flights performed for the course flight dynamics in the third year of the Aerospace Engineering Bachelor's degree at Delft University of Technology. All aerospace students have an opportunity to be part of a flight test, in which data is collected for their projects. Van Horssen [22] used data collected during these flights for his Master Thesis work. The dataset consisted of 69 stalls.
- **2016 stall data**: Van Horssen [22] recognized that a lack of data on the angle of sideslip limits the modeling capabilities. In 2017 specific stall tests were performed with an air data boom measuring both angle of attack and sideslip. Van Ingen [23] analyzed the performance of an updated Kalman filter, which revealed that the 2015 stall data will be unreliable when a sideslip is present. The reliability can not be verified as there is no data on the sideslip during those tests. It is thus unwise to use the data from 2015.
- **2018 stall data**: In 2018 another test was performed. In this case, audio and video were recorded for later use in the flight simulator. Furthermore, multiple stalls were recorded for identification purposes. The logbook shows that problems were encountered with the autopilot and fly-by-wire system. However, this data was still used by Delfosse [27] in his work on asymmetric stall modeling.
- **2019 stall data**: In 2019 a test was performed that mainly gathered data in the landing configuration of the aircraft. Delfosse [27] used this data to create a stall model in this configuration.
- **2022 stall data**: In 2022 extra data was gathered on stalls with high angles of sideslip. This was done as part of the research effort by De Fuijk [29], who focused on improving the asymmetric stall model of the Citation.
- **2023 stall data**: In 2023 the research group started researching multivariate splines as a method for full envelope stall modelling. For this reason, a test flight was performed gathering data at different flight levels. At all flight levels stalls and normal maneuvers were performed.
- **2024 stall data**: In 2024 another stall test was performed to gather data for accelerated stalls of 1.4g. This equates to a bank angle of 45 degrees. This data has been used by Van Wezel [33] to combat $\dot{\alpha}$ and q^* correlations. This resulted in a new method for modeling the pitch moment coefficient.

The data compiled over the years can be combined to create new data sets. However, it is worth mentioning two sets as they have been used in the past by Van Ingen [23] and De Fuijk [29]. These are referred to as the *Van Ingen* and the *Asym* datasets. The former includes 34 stalls and was used by Van Ingen [23] for identification purposes. This set includes the stalls performed in the 2016 stall data, an overview is provided in Table 2.3. De Fuijk [29] used a part of the data in the *Van Ingen* dataset, supplemented with data collected in the test flight of 2022. An overview of this dataset is given in Table 2.4.

Table 2.3: An overview of the manoeuvres included in the *Van Ingen* data set. (Adapted from [29])

Flight Level	Load factor	Intended sideslip (°)	Input(δ_a|δ_e)	Number of data sets
80-110	1.0g	0	QR | QR	2
110-150	1.0g	0	QR | QR	4
150-200	1.0g	0	QR | QR	11
150-200	1.1g	0	QR | QR	10
150-200	1.3g	0	QR | QR	7

Table 2.4: An overview of the manoeuvres included in the *Asym* data set. (Adapted from [29])

Flight Level	Load factor	Intended sideslip (°)	Input(δ_a|δ_e)	Number of data sets
150-200	1.1g	0	QR | QR	12
150-200	1.1g	0	3211 | QR	5
150-200	1.1g	5	QR | QR	1
150-200	1.1g	5	3211 | QR	5
150-200	1.3g	0	QR | QR	7

2.2.3. Flight Path Reconstruction

Flight path reconstruction is an essential part of any aircraft system identification routine. The sensors discussed in Subsection 2.2.1 will include bias and noise. Moreover, some states can not be directly measured. In Delft, the two-step method was developed to perform system identification when such biases, noise and unmeasured states are present. The two-step method first estimates the aircraft states and then uses the aircraft states as input for system identification. The motivation behind this choice comes from the common use of linear flight models. By splitting the steps, only the state estimation is nonlinear. This allows for the use of easier linear system identification methods, such as ordinary least squares. Furthermore, the trouble of setting up a state estimation method such as a Kalman filter does not need to be repeated when different model structures are explored. The use of Kalman filters has been well covered in the stall research group and is therefore not a focus in this research. An unscented Kalman filter is used and more information on the implementation of such a filter can be found in, for example, Van Ingen [23].

2.3. Aerodynamic Stall Modeling

Aerodynamic stall modeling has been extensively researched in the context of aircraft stability analysis [34] and rotor load analysis [35]. This section introduces the current state of the field. First, a recap of stall types and phenomena is given in Subsections 2.3.1 and 2.3.2. Then, an introduction to the Goman-Khrabrov stall model [34] is given in Subsection 2.3.3, which is the major model in aircraft stall modeling. Lastly, the Leishman-Beddoes model is introduced in Subsection 2.3.4, this model is the largest in rotor loads analysis.

2.3.1. Types of Stall

In this section, an introduction is given to different types of stall. The types discussed are associated with low speeds and the information is taken from Anderson [32, pp. 395-400]. At high speeds stall can also occur, Vos and Farokhi [36] discuss this in more detail. The low-speed stall types are:

- **Leading edge stall:** A stall phenomenon associated with thin airfoils, between 10% and 16% of the chord length. As the name suggests, stall is initiated at the leading edge. The complete flow separation results in a sharp decrease in lift coefficient.
- **Trailing edge stall:** Alternatively, stall can be initiated from the trailing edge. This type of stall is characteristic for thicker airfoils. The lift decrease is more gradual due to the separation creeping forward on the airfoil.
- **Thin airfoil stall:** This stall happens for extremely thin airfoils. The high rate of curvature at thin airfoil leading edges causes early separation. Opposed to leading edge stall, the flow reattaches and forms a separation bubble. As the angle of attack is increased the reattachment point moves backwards and reaches the trailing edge, after which complete separation takes place. This type of stall is very subtle and can be similar to trailing edge stall.

2.3.2. Dynamic Stall Phenomenology

The previous section introduced three types of stall. These are measured under static conditions. During dynamic maneuvers, additional effects are introduced. Before diving into the detailed models that represent the stall, the phenomena involved during the dynamic stall are discussed. Figure 2.2 shows the

lift curve for an airfoil following a ramp in the angle of attack. Multiple phases can be extracted from the curve, which are numbered. These numbers relate to the airfoils presented in Fig. 2.3, which shows the flow fields at the specific stage. The stages can be explained as follows:

- **Point 1:** There are slight differences observed in the linear part of the lift curve. The lift is slightly higher due to the rotation of the airfoil. This is due to a starting vortex that is formed on the top surface. This is a well-known phenomenon and is modeled by the Wagner function [37].
- **Point 2:** This is the point where the static stall is observed, it can be seen that the unsteady lift curve extends beyond the static lift curve. This continuation of the lift curve is attributed to a vortex at the trailing edge that induces suction at the trailing edge. As can be seen in Fig. 2.3. The trailing edge suction leads to an additional positive pressure gradient over the top of the airfoil, which allows the flow to stay attached.
- **Point 3:** There is a plateau visible which happens as the trailing edge vortex separates. The suction at the trailing edge disappears and flow reversal starts from the trailing edge.
- **Point 4:** After the plateau another increase in lift is visible. This is caused by the creation of a dynamic stall vortex (DSV). This vortex is formed due to an accumulation of reverse flow causing the shear layer to roll up. The existence of a vortex causes additional suction pressure.
- **Point 5:** At this point the maximum lift is achieved. This is caused by the separation of the DSV which convects over the airfoil. The maximum lift is achieved as the DSV reaches the mid-chord.
- **Point 6:** As the DSV separates a large reduction in lift is observed. If the increase in angle of attack continues beyond this point additional stall vortices can be formed causing further fluctuations in the lift.

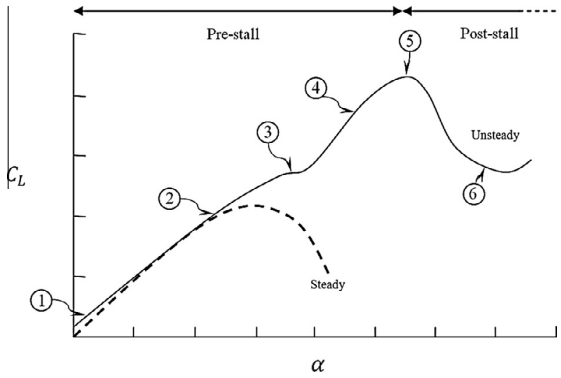

Figure 2.2: Lift coefficient during a progressive dynamic stall. Angle of attack follows a ramp profile. (adapted from [38])

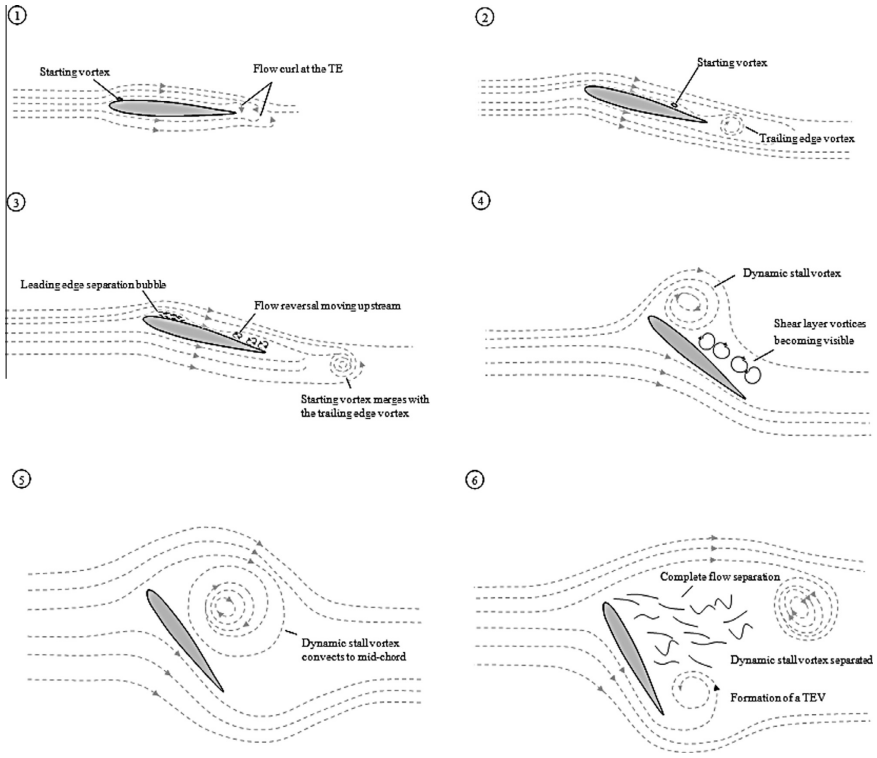

Figure 2.3: Flow fields around an airfoil during dynamic stall (adapted from [38])

2.3.3. Goman-Khrabrov Model

Introduced by Goman and Khrabrov [34] with flight dynamics simulation and stability analysis in mind, this model is a simple representation of some of the effects that take place during flow separation and vortex breakdown. Specifically, it is used to model trailing edge flow separation and its effect on the aircraft lift.

Longitudinal Modeling

To model trailing edge stall Goman and Khrabrov [34] used Kirchhoff's theory of flow separation for flat plates. It stipulates that the lift coefficient depends on an internal variable X. This variable describes the state of flow separation as the chord-wise separation point, 0 describes a fully separated flow at the leading edge and 1 describes a fully attached flow. Equation (2.1) describes the dependence of the lift coefficient on the flow separation variable [15]. This is a relatively simple model for illustration, but during model identification, an iterative procedure to find model terms can be used [23].

$$C_L(\alpha, X) = C_{L_\alpha} \left(\frac{1+\sqrt{X}}{2} \right)^2 \alpha \tag{2.1}$$

From the equation above, it can be seen that when the airflow is fully attached ($X = 1$) the equation reduces to $C_L(\alpha) = C_{L_\alpha}\alpha$, which describes the lift coefficient as a linear function of the angle of attack. However, when the flow separates the lift is reduced, this is in line with expectations of a stall. Fischenberg [15] suggests a formulation for the steady flow separation point described in Eq. (2.2). Here a_1 and α^* are fitting parameters that will be explained later.

$$X_0(\alpha) = \frac{1}{2}\left\{1 - \tanh\left(a_1(\alpha - \alpha^*)\right)\right\} \tag{2.2}$$

With Eqs. (2.1) and (2.2) the static lift curve can be created. This is the curve created when taking static measurements at different angles of attack. An example can be seen in Fig. 2.4. However, it is known that during unsteady conditions the separation point will be significantly different from the static measurements.

This can be attributed to two categories of effects. Firstly, due to circulation and boundary layer effects and secondly, because of time lag in the response to a new flow condition. These two effects are accounted for by the first-order differential equation in Eq. (2.3). The differential equation is a simple approximation of the Wagner or Theodorsen function [15].

$$\tau_1 \frac{dX}{dt} + X = X_0 \left(\alpha - \tau_2 \dot{\alpha}\right) \tag{2.3}$$

The differential equation above introduces two time constants, τ_1 and τ_2. These account for the unsteady effects mentioned before. To visualise the effect each parameter has, Figs. 2.4 to 2.7 are created. A summary of the model parameters with a description of the influence it has is presented:

- **Abruptness parameter (a_1):** This parameter determines the abruptness of the separation and lift drop-off. The effect of this parameter is visualized in Fig. 2.4. It can be seen that an increase in the magnitude of this parameter speeds up the transition from fully attached to fully separated. As a result, it can be seen that the drop-off in lift is sharper.
- **Separation parameter (α^*):** This parameter defines the 50% separation point in a steady condition. The effect of this parameter is visualized in Fig. 2.5. It can be seen that an increase of this parameter shifts the curve for X as a function of α to the right. As a result, the maximum lift coefficient is larger.
- **Time lag parameter (τ_1):** This parameter describes a phase delay in the separation point X. The effect of this parameter is visualized in Fig. 2.6. It can be seen that the separation and attachment are delayed under a periodic excitation of the angle of attack.
- **Hysteresis parameter (τ_2):** This parameter describes the hysteresis effect caused by the angle of attack rate. The effect of this parameter is visualized in Fig. 2.7.

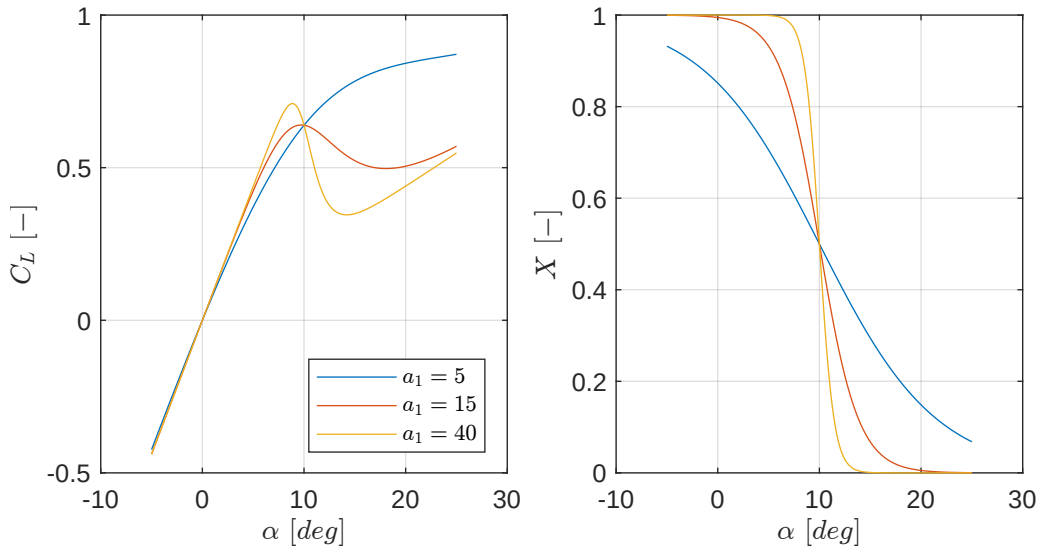

Figure 2.4: Effect of parameter a_1 on the lift curve and flow separation point. With lift curve slope $C_{L_\alpha} = 1.6\pi$ $[rad^{-1}]$, separation parameter $\alpha^* = 10$ $[deg]$, time lag and hysteresis parameters $\tau_1 = \tau_2 = 0$ $[s]$

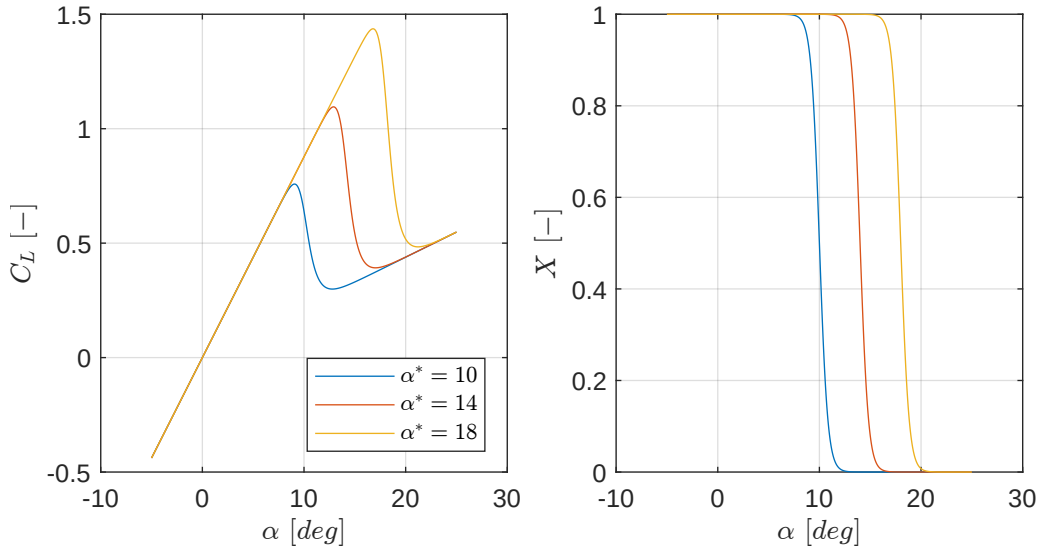

Figure 2.5: Effect of parameter α^* on the lift curve and flow separation point. With lift curve slope $C_{L_\alpha} = 1.6\pi\ [rad^{-1}]$, abruptness parameter $a_1 = 70\ [-]$, time lag and hysteresis parameters $\tau_1 = \tau_2 = 0\ [s]$

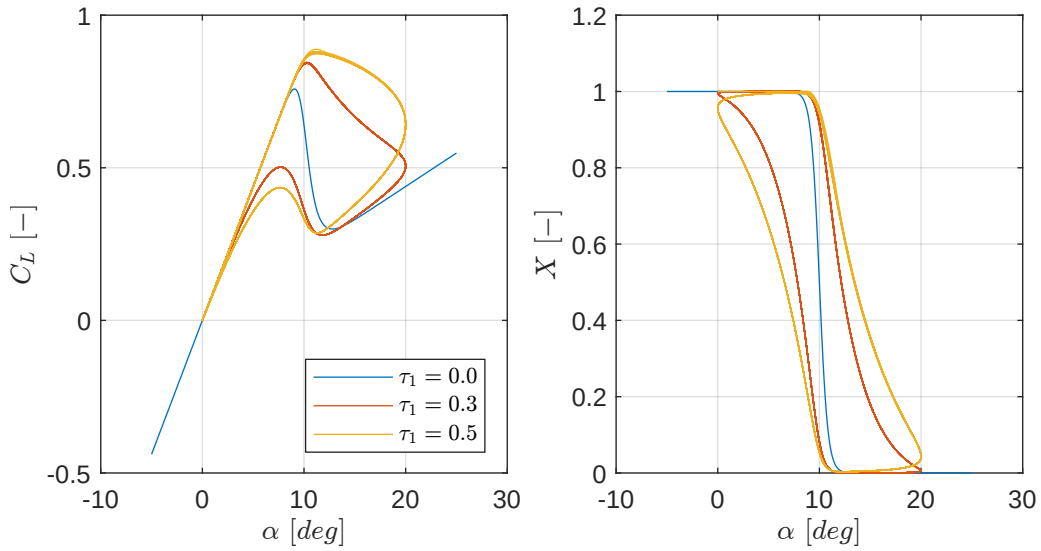

Figure 2.6: Effect of parameter τ_1 on the lift curve and flow separation point. With lift curve slope $C_{L_\alpha} = 1.6\pi\ [rad^{-1}]$, separation parameter $\alpha^* = 10\ [deg]$, abruptness parameter $a_1 = 70\ [-]$ and hysteresis parameter $\tau_2 = 0\ [s]$

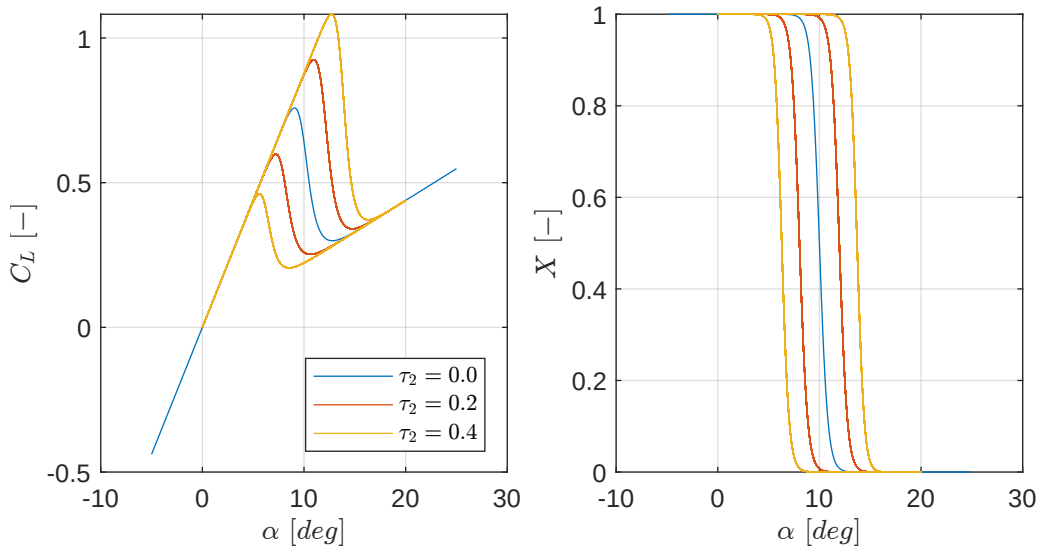

Figure 2.7: Effect of parameter τ_1 on the lift curve and flow separation point. With lift curve slope $C_{L_\alpha} = 1.6\pi\ [rad^{-1}]$, separation parameter $\alpha^* = 10\ [deg]$, abruptness parameter $a_1 = 70\ [-]$ and time lag parameter $\tau_1 = 0\ [s]$

Asymmetric Modeling

The model described above can only treat the longitudinal aspects of a stall. It was found by Van Ingen [23] that stall modelling with the separation point X does not identify stall contributions to the asymmetric dynamics. During testing, large roll-offs were observed. In the literature, these roll-offs are described as being caused by differential lift on lifting surfaces [29, 18, 17]. In mathematical terms, it can be said that the difference in the roll and yaw moment coefficients is described by Eqs. (2.11) and (2.12) respectively.

$$\Delta\hat{C}_l = \left[(C_L)_l - (C_L)_r\right]\frac{y_w}{b} \tag{2.4}$$

$$\Delta\hat{C}_n = \left[(C_D)_l - (C_D)_r\right]\frac{y_w}{b} \tag{2.5}$$

To model differences between the left and right wing, De Fuijk [29] proposes using a local angle of attack as seen in Eq. (2.6). This local angle of attack is determined at the mean aerodynamic chord (MAC), with $\Delta y_P = \pm y_{MAC}$. An additional effect of the difference in the angle of attack is that the separation is also different. Now the left and right wings have separate governing flow separation points as can be seen in Eq. (2.7). This will propagate further into the lift formulation, as can be seen in Eq. (2.1).

$$\alpha_P = \text{atan}\left(\frac{w_P}{u_P}\right) = \text{atan}\left(\frac{w - q\Delta x_P + p\Delta y_P}{u - r\Delta y_P + q\Delta z_P}\right) \tag{2.6}$$

$$\tau_1\frac{dX_{l,r}}{dt} + X_{l,r} = \frac{1}{2}\left\{1 - \tanh\left(a_1\left(\alpha_{l,r} - \tau_2\dot{\alpha}_{l,r} - \alpha^*\right)\right)\right\} \tag{2.7}$$

In the work by De Fuijk [29] two different models for the roll moment were proposed. Firstly, Eq. (2.1) is used to define the difference in lift. The resulting formula can be seen in Eq. (2.8). Furthermore, by assuming symmetric wings, the coefficients $(C_{L_\alpha})_L$ and $(C_{L_\alpha})_R$ are identical and can be reduced to $C_{l_{\Delta K_a}}$. Furthermore, ΔK_a is introduced leading to the reformulation in Eq. (2.9).

$$\Delta\hat{C}_l = \left[(C_{L_\alpha})_l\left(\frac{1+\sqrt{X_l}}{2}\right)^2\alpha_l - (C_{L_\alpha})_r\left(\frac{1+\sqrt{X_r}}{2}\right)^2\alpha_r\right]\frac{y_w}{b} \tag{2.8}$$

$$\Delta\hat{C}_l = C_{l_{\Delta K_a}} \Delta K_a \frac{y_w}{b} \quad \text{with} \quad \Delta K_a = \left(\frac{1+\sqrt{X_l}}{2}\right)^2 \alpha_l - \left(\frac{1+\sqrt{X_r}}{2}\right)^2 \alpha_r \tag{2.9}$$

Alternatively, Eq. (2.10) is proposed. The reason for this simpler model is that it was not known if the Kirchhoff model could be used for a single wing. This model takes the difference between the separation parameters as a regressor for the roll moment coefficient. De Fuijk [29] determined that this second model was more effective in fitting the data.

$$\Delta\hat{C}_l = C_{l_{\Delta X}} \Delta X \frac{y_w}{b} \quad \text{with} \quad \Delta X = X_l - X_r \tag{2.10}$$

Singh and Jategaonkar [17] propose a slightly different model structure, they argue that the roll and yaw moments are not a function of the lift and drag coefficients, but of the normal and chord-wise coefficient. The difference between these two reference frames is the angle of attack. For the dataset used by De Fuijk [29] this difference leads to a maximum error of 4.5%, calculated at the maximum angle of attack.

$$\Delta\hat{C}_l = \left[(C_N)_l - (C_N)_r\right] \frac{y_w}{b} \tag{2.11}$$

$$\Delta\hat{C}_n = \left[(C_c)_l - (C_c)_r\right] \frac{y_w}{b} \tag{2.12}$$

In the original paper by Goman and Khrabrov [34], the authors proposed a different method for including asymmetric effects. They included an effect of sideslip to the separation parameter as follows:

$$\tau_1 \frac{dX_{l,r}}{dt} + X_{l,r} = X_0 \pm \frac{\partial X_0}{\partial \beta}\left(\beta - \tau_3 \dot{\beta}\right), \tag{2.13}$$

where a third time delay is included for the angle of sideslip. By assuming the roll moment induced by the vortex breakdown will be proportional to the difference between the left and right separation parameters, a new differential equation can be created:

$$\tau_1 \frac{dC_l^{vor}}{dt} + C_l^{vor} = \frac{dC_l^{vor}}{dX} \frac{dX_0}{d\beta}\left(\beta - \tau_3 \dot{\beta}\right). \tag{2.14}$$

It should be noted that this analysis was performed for a delta wing and the application to an aircraft should be analyzed.

2.3.4. Leishman-Beddoes Model

As a quick note, the Goman-Khrabrov model is not the only existing stall model. It is merely the one commonly used in aircraft stall modeling. In the field of helicopter and wind turbine load analysis, different models exist. Perhaps the most influential work has been by Leishman and Beddoes [35]. Melani et al. [39] provides a review of the current landscape in the field of rotor stall models, an adapted figure from their work has been included in Fig. 2.8. Due to the highly dynamic nature of rotors, more effects have been included in the stall models, such as leading-edge stall, center of pressure corrections, and first and second-order vortex shedding.

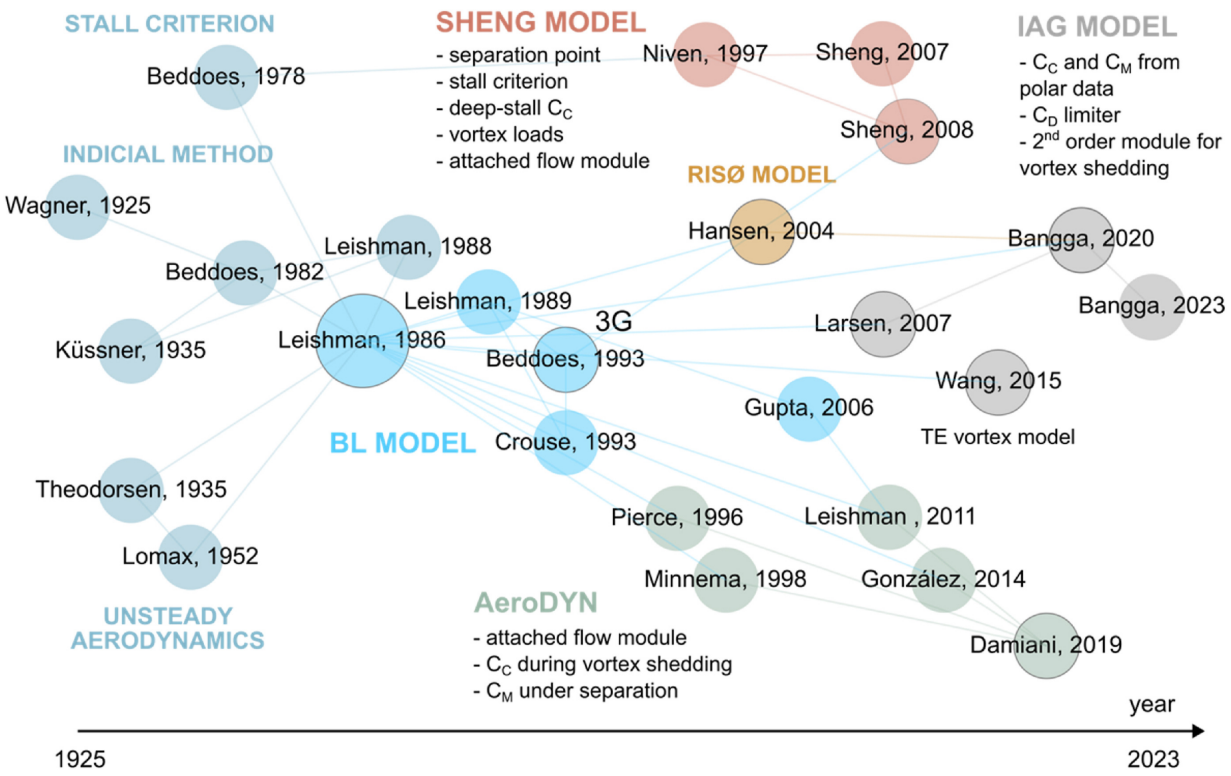

Figure 2.8: A review of stall models in the field of rotor load analysis (Adapted from [39])

2.4. Multivariate B-splines

Multivariate B-splines are an advanced nonlinear modeling structure, that has been well-researched at Delft University of Technology. Due to its stable local basis it is ideal for global nonlinear model estimation. Multivariate B-splines are seen as a potential method for merging nominal and stall flight regimes.

The foundation of simplex multivariate B-splines is the simplex. A simplex is defined as a geometrical structure that minimally spans a set of dimensions. The simplex of dimension n is uniquely defined by $n+1$ non-degenerate vertices. Simplices have a local coordinate system called the Barycentric coordinate system. To convert Cartesian coordinates $\boldsymbol{x} = (x_0, x_1, \cdots, x_{n-1})$ to barycentric coordinates $\boldsymbol{b} = (b_0, b_1, \cdots, b_n)$ on a n-simplex $t_j = \langle v_0, v_1, \cdots, v_n \rangle$, the transformation for a given x can be done using the equations below, where first $b1$ through b_n are calculated using Eqs. (2.15) and (2.16) and subsequently b_0 is calculated using Eq. (2.17). Finally, these calculations are given a shorthand notation: $b = b_{t_j}(x)$.

$$\begin{bmatrix} b_1 & b_2 & \cdots & b_n \end{bmatrix}^\top = A_{t_j}^{-1} \cdot \left(x^\top - v_0^\top\right) \tag{2.15}$$

$$A_{t_j} = \begin{bmatrix} (v_1 - v_0)^\top & (v_2 - v_0)^\top & \cdots & (v_n - v_0)^\top \end{bmatrix} \tag{2.16}$$

$$b_0 = 1 - \sum_{i=1}^{n} b_i \tag{2.17}$$

The simplex polynomial basis functions are derived from the multinomial expansion presented in Eq. (2.18). Some notation can be introduced to simplify this formulation. Firstly, the multi-index $\kappa = (\kappa_0, \kappa_1, \cdots, \kappa_n)$ is introduced. The multi-index has the following properties: $|\kappa| = \kappa_0 + \kappa_1 + \cdots + \kappa_n$ and $\kappa! = \kappa_0! \kappa_1! \cdots \kappa_n!$.

$$(b_0 + b_1 + \cdots + b_n)^d = \sum_{\kappa_0+\kappa_1+\cdots+\kappa_n=d} \frac{d!}{\kappa_0! \kappa_1! \cdots \kappa_n!} b_0^{\kappa_0} b_1^{\kappa_1} \cdots b_n^{\kappa_n} \tag{2.18}$$

Using the multi-index properties the basis functions of Eq. (2.18), $B_\kappa^d(b)$, can be simplified as described in Eq. (2.19). Additional simplification is done using the following notation: $b^\kappa = b_0^{\kappa_0} b_1^{\kappa_1} \cdots b_n^{\kappa_n}$.

$$B_\kappa^d(b) = \frac{d!}{\kappa!} b_0^{\kappa_0} b_1^{\kappa_1} \cdots b_n^{\kappa_n} = \frac{d!}{\kappa!} b^\kappa \tag{2.19}$$

Using the basis functions a simplex polynomial can be created by multiplying the basis functions defined in Eq. (2.19) by a polynomial coefficient. This formulation is given in Eq. (2.20). Additionally, the vector notation of the simplex polynomial is given in Eq. (2.21).

$$p(b) = \sum_{|\kappa|=d} c_\kappa^{t_j} B_\kappa^d(b_{t_j}(x)) \tag{2.20}$$

$$p(b) = B_{t_j}^d(b_{t_j}(x)) c^{t_j} \tag{2.21}$$

This formulation is called the B-form of a simplex polynomial. The polynomial coefficients are also named B-coefficients. These coefficients locally control the shape of the simplex polynomial and a spatial location can be assigned to them. The Barycentric coordinates of these locations are calculated using Eq. (2.22). The spatial locations have been visualized for increasing orders one through four in Fig. 2.9.

$$b(c_\kappa) = \frac{\kappa}{d} \tag{2.22}$$

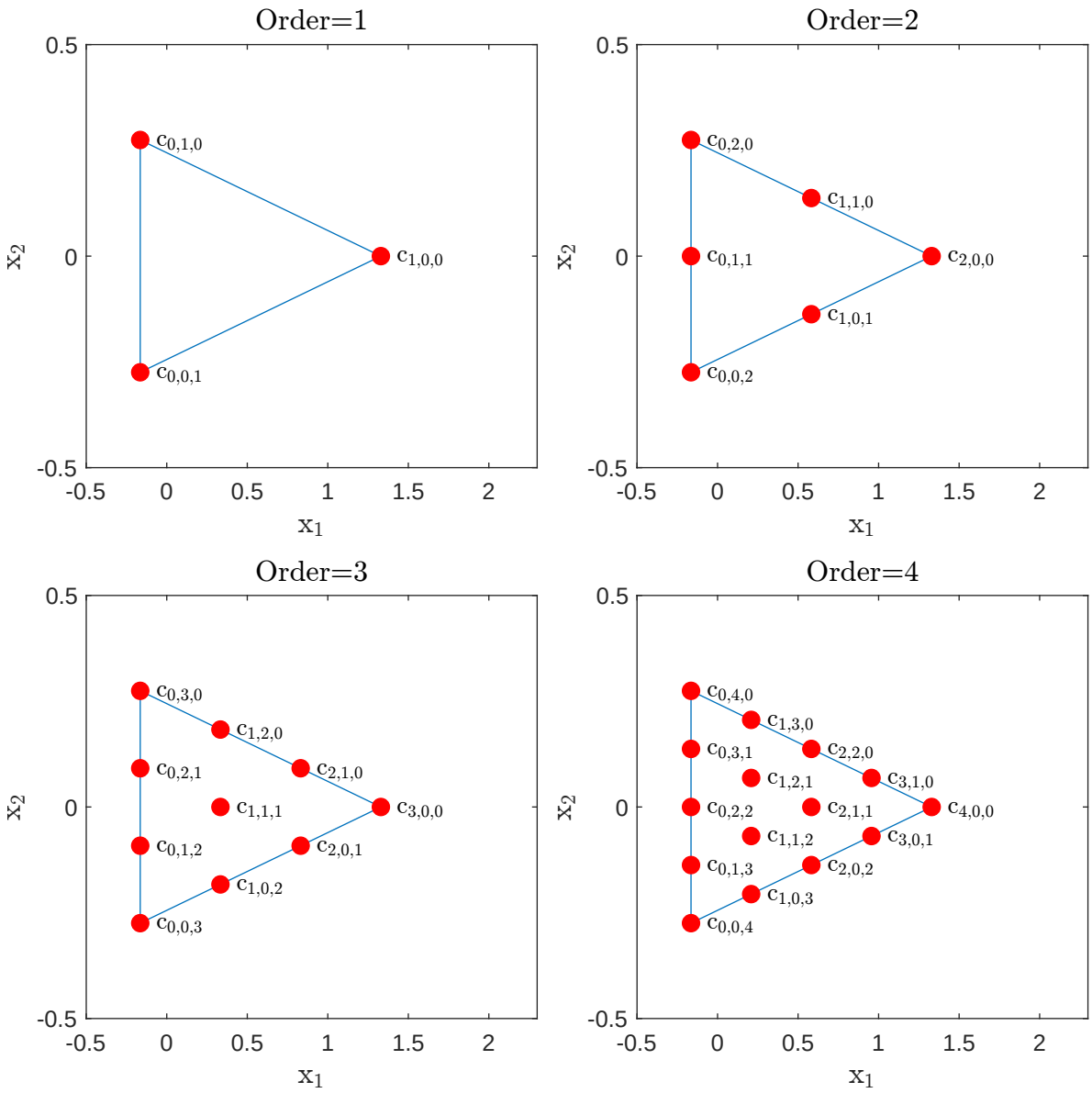

Figure 2.9: Visual representation of the B-coefficient spatial locations for increasing order of simplex polynomial

To move from a single simplex polynomial to a simplex spline, the concept of triangulation needs to be explained. A triangulation $\mathcal{T}$ is the partitioning of an n-dimensional domain into a set of J n-simplices that do not overlap. The intersection of two simplices t_i and t_j is defined as the null space or a k-simplex $\tilde{t}$ with $0 \leq k \leq n-1$ [40].

$$\mathcal{T} \coloneqq \bigcup_{i=1}^{J} t_i, \quad t_i \cap t_j \in \left\{\emptyset, \tilde{t}\right\}, \quad \forall t_i, t_j \in \mathcal{T} \tag{2.23}$$

For a triangulation $\mathcal{T}$ consisting of J simplices, the spline function can be defined:

$$s_d^r(x) = B^d(b(x)) \cdot c \in \mathbb{R} \tag{2.24}$$

where B^d is a row vector that contains the basis function of every simplex t_j, as

$$B^d\left(b\left(x\right)\right) \coloneqq \left[\begin{array}{cccc} B^d_{t_1}\left(b\left(x\right)\right) & B^d_{t_2}\left(b\left(x\right)\right) & \cdots & B^d_{t_J}\left(b\left(x\right)\right) \end{array}\right] \in \mathbb{R}^{1\times J\cdot\hat{d}}, \tag{2.25}$$

and c is a column vector that contains all B-coefficients for each simplex t_j, as

$$c \coloneqq \left[\begin{array}{cccc} c^{t_1^\top} & c^{t_2^\top} & \cdots & c^{t_J^\top} \end{array}\right]^\top \in \mathbb{R}^{J\cdot\hat{d}\times 1}. \tag{2.26}$$

With the inclusion of multiple simplices, there arises a need for continuity conditions. The continuity conditions ensure a smooth transition from simplex to simplex. Continuity comes in different orders where the r$^{\text{th}}$ order continuity implies that the r$^{\text{th}}$ directional derivative of the simplex polynomials of adjacent simplices is continuous across the interface. The condition that guarantees this is Eq. (2.27), where v_* is the out-of-edge vertex. Note that this is just one of the possible permutations of the multi-index, the location of m and 0 are arbitrary and dependent on the out-of-edge vertex.

$$c^{t_2}_{\kappa_0,m,\kappa_1} = \sum_{|\gamma|=m} c^{t_1}_{(\kappa_0,0,\kappa_1)+\gamma} B^m_\gamma\left(v_*\right), \quad 0 \leq m \leq r \tag{2.27}$$

Using Eq. (2.27) the smoothness matrix H can be constructed. The continuity conditions can be summarized as a system of equations:

$$H \cdot c = 0 \tag{2.28}$$

For the parameters of a simplex spline, a constrained least-squares problem must be solved. This can be done by using Lagrange multipliers and a modified cost function called the Lagrangian:

$$L\left(c,\lambda\right) = \frac{1}{2}\left(Y - B\cdot c\right)^\top\left(Y - B\cdot c\right) + \lambda^\top \cdot H \cdot c. \tag{2.29}$$

The optimum of this cost function can be found at the point where the partial derivatives with respect to c and λ are zero. This can be reformulated in the following form,

$$\left[\begin{array}{cc} B^\top\cdot B & H^\top \\ H & 0 \end{array}\right] \cdot \left[\begin{array}{c} c \\ \lambda \end{array}\right] = \left[\begin{array}{c} B^\top \cdot Y \\ 0 \end{array}\right]. \tag{2.30}$$

The first matrix in this form is called the Karush-Kuhn-Tucker (KKT) matrix and by inverting it one can solve for the parameters c and λ. However, due to the general rank deficiency of the smoothness matrix, the KKT matrix cannot be inverted and the Moore-Penrose pseudo inverse should be used. As the KKT matrix can get large, it is more efficient to use iterative numerical solvers. One way to do this is by using the following scheme:

$$\hat{c}^{(1)} = \left(2B^\top\cdot B + \frac{1}{\varepsilon}H^\top\cdot H\right)^{-1}\cdot\left(2B^\top\cdot Y - H^\top\cdot\hat{\lambda}^{(0)}\right), \tag{2.31}$$

$$\hat{c}^{(k+1)} = \left(2B^\top\cdot B + \frac{1}{\varepsilon}H^\top\cdot H\right)^{-1}\cdot 2B^\top\cdot B\cdot\hat{c}^{(k)}, \tag{2.32}$$

where ε must be some small number such as $1\text{e}{-6}$ and the initial value for the Lagrange parameters should be $\hat{\lambda}^{(0)} = 1$. Another way to ensure the continuity conditions are met is by introducing Γ, the null space of the smoothness matrix H. The continuity conditions are automatically met by forcing the parameters c to be a linear combination of the vectors in the null space of H. The parameters look like this,

$$c = \Gamma\cdot\tilde{c}. \tag{2.33}$$

The modification should be introduced in the cost function, by substituting c in the least squares problem. The cost function looks like this,

$$L\left(\tilde{c}\right) = \left\|Y - B \cdot c\right\|^2 = \left\|Y - B \cdot \Gamma \cdot \tilde{c}\right\|^2, \tag{2.34}$$

where one now solves the modified unconstrained least squares problem. The least squares solution of the free parameters $\tilde{c}$ is,

$$\hat{\tilde{c}} = \left(B \cdot \Gamma\right)^+ \cdot Y. \tag{2.35}$$

The parameters can then be extracted by pre-multiplying the free parameters $\hat{\tilde{c}}$ with the null space Γ.

2.5. Separable Nonlinear Least squares

Separable Nonlinear Least Squares (SNLS) is a class of nonlinear least squares problems with a special structure. The structure discriminates parameters in a group of linear and nonlinear parameters. The premise of this method is that the linear parameters can be rewritten as a function of the nonlinear parameters, thereby reducing the dimension of the parameter space. Furthermore, Golub and Pereyra [41] found that leveraging this special structure reduces computation time. The technique has been widely used in research fields such as telecommunications, robotics, and medical imaging [41].

2.5.1. Cost Function

To further understand SNLS and its potential application to aerodynamic stall modeling, the mathematical structure of an SNLS problem will be explored. An SNLS model consists of a linear set of parameters $\boldsymbol{c}$, which multiply a set of regressors $\boldsymbol{\Phi}$. Opposed to standard linear least squares, the regressors $\boldsymbol{\Phi}$ can be a function of a nonlinear set of parameters $\boldsymbol{\theta}$. Note that this work deviates its notation from Golub and Pereyra [42] to avoid confusion with the angle of attack α. The model output can then be written as follows:

$$\hat{y}_i\left(\boldsymbol{c}, \boldsymbol{\theta}\right) = \boldsymbol{\Phi}\left(\boldsymbol{\theta}; t_i\right) \cdot \boldsymbol{c}, \tag{2.36}$$

where $\boldsymbol{c} \in \mathbb{R}^n$ and $\boldsymbol{\theta} \in \mathbb{R}^k$. The least squares cost function for this model structure is formulated as the vector norm of the difference between the observations $\boldsymbol{y}$ and the model output $\hat{\boldsymbol{y}}$ as

$$r\left(\boldsymbol{c}, \boldsymbol{\theta}\right) = \left\|\boldsymbol{y} - \hat{\boldsymbol{y}}\right\|^2 = \left\|\boldsymbol{y} - \boldsymbol{\Phi}\left(\boldsymbol{\theta}\right)\boldsymbol{c}\right\|^2. \tag{2.37}$$

Due to the special property of SNLS, for a given $\boldsymbol{\theta}$, a linear least squares solution can be found for the parameters $\boldsymbol{c}$:

$$\boldsymbol{c}\left(\boldsymbol{\theta}\right) = \boldsymbol{\Phi}\left(\boldsymbol{\theta}\right)^+ \boldsymbol{y}, \tag{2.38}$$

where $\boldsymbol{\Phi}\left(\boldsymbol{\theta}\right)^+$ indicates the Moore-Penrose pseudo inverse of $\boldsymbol{\Phi}\left(\boldsymbol{\theta}\right)$. Golub and Pereyra [42] proved that a global minimizer $\hat{\boldsymbol{\theta}}$ implies a global minimizer $\hat{\boldsymbol{c}}$. This enables the reduction of the parameter space:

$$r\left(\boldsymbol{\theta}\right) = \left\|\boldsymbol{y} - \boldsymbol{\Phi}\left(\boldsymbol{\theta}\right)\boldsymbol{\Phi}\left(\boldsymbol{\theta}\right)^+ \boldsymbol{y}\right\|^2 = \left\|P^{\perp}_{\boldsymbol{\Phi}(\boldsymbol{\theta})}\boldsymbol{y}\right\|^2 = \left\|\boldsymbol{r}_2\left(\boldsymbol{\theta}\right)\right\|^2, \tag{2.39}$$

where $\boldsymbol{c}$ is eliminated by substituting Eq. (2.38) into Eq. (2.37). Furthermore, $P^{\perp}_{\boldsymbol{\Phi}(\boldsymbol{\theta})}$ is the projector onto the orthogonal complement of the column space of $\boldsymbol{\Phi}\left(\boldsymbol{\theta}\right)$, defined as $\boldsymbol{I} - \boldsymbol{\Phi}\left(\boldsymbol{\theta}\right)\boldsymbol{\Phi}\left(\boldsymbol{\theta}\right)^+$.

2.5.2. Objective Gradient

Common methods for optimizing a nonlinear least squares problem require a residual Jacobian matrix. The Jacobian matrix provides the sensitivity of the residual vector $\boldsymbol{r}_2\left(\boldsymbol{\theta}\right)$ to changes in the parameters $\boldsymbol{\theta}$.

Golub and Pereyra [42] defined as:

$$\boldsymbol{D}\boldsymbol{r}_2\left(\boldsymbol{\theta}\right) = \boldsymbol{D}\boldsymbol{P}^{\perp}_{\boldsymbol{\Phi}(\alpha)}\boldsymbol{y} = -(\boldsymbol{P}^{\perp}_{\boldsymbol{\Phi}}\boldsymbol{D}\boldsymbol{\Phi})\boldsymbol{\Phi}^{+}\boldsymbol{y} - (\boldsymbol{\Phi}^{+})^{\top}(\boldsymbol{P}^{\perp}_{\boldsymbol{\Phi}}\boldsymbol{D}\boldsymbol{\Phi})^{\top}\boldsymbol{y}, \tag{2.40}$$

where $\boldsymbol{D}\boldsymbol{\Phi}$ is the Frechet derivative of the regression matrix $\boldsymbol{\Phi}$. This derivative is a three-dimensional tensor that stores, for each observation m, the derivatives of the n regressors with respect to the k parameters. This results in a $m \times n \times k$ sized tensor. This is visualized in Fig. 2.10. The multiplication involving the tensor is done page-wise, meaning that the multiplication is performed as a matrix multiplication for each entry in the parameter dimension of the tensor.

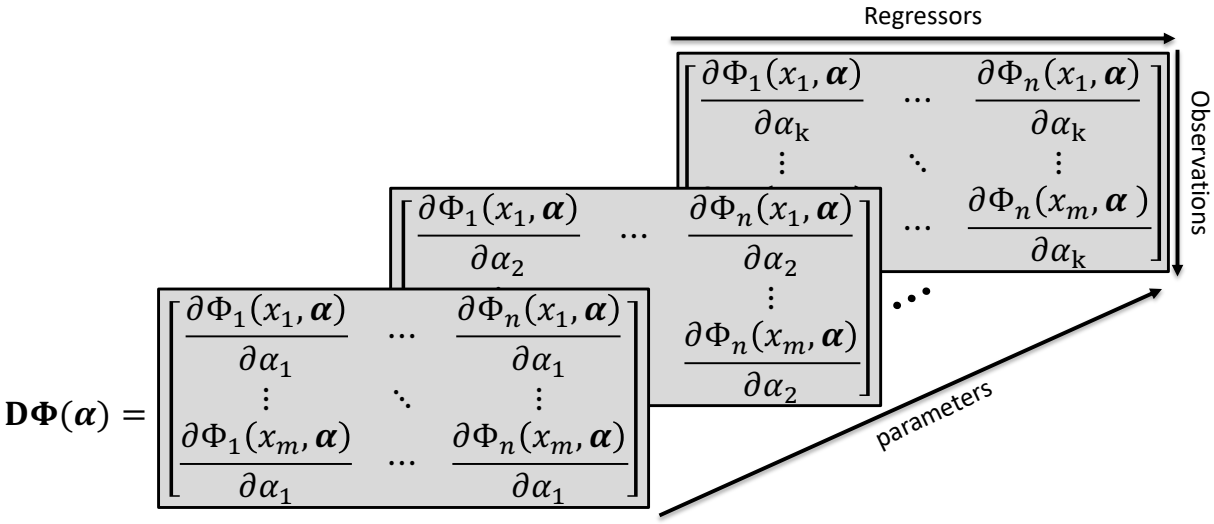

Figure 2.10: Visual representation of the Frechet derivative of ϕ. Own work.

Golub and Pereyra [42] identified that the tensor $\boldsymbol{D}\boldsymbol{\Phi}$ often has many zero columns. This is the case when not all regressors are a function of all nonlinear parameters. To improve storage, a lookup table that maps the regressors to the nonzero derivatives is suggested by O'Leary and Rust [43]. The three-dimensional tensor can be stored in a $m \times l$ array, where each column corresponds to a nonzero column of the tensor. The lookup table is a $2 \times l$ array that stores information about the l nonzero columns of the tensor. Each column I of the lookup table describes the partial derivative of regressor Φ_{I_1} to parameter α_{I_2} and corresponds to the same column in the $m \times l$ array. An example of this process is provided in O'Leary and Rust [43].

2.5.3. Statistical Properties

Once the parameter values have been found, one needs to judge the reliability of the results. One way to do this is to approximate the covariance matrix of the parameters. The covariance matrix contains the variance of the parameters on the diagonal. A reliable result will give a low variance meaning that it is not dependent on the specific realizations of the data. In other words, it is robust to noise. The covariance of the parameters can be found outside the diagonal. It describes the relation between the parameters, if the covariance is high the parameters are co-linear and characterize the same information in the data.

For the SNLS model structure Mahata and Söderström [44] derived an equation for the covariance matrix $C_{\hat{\theta}}$, which contains the covariance of the linear and nonlinear parameters. The formulation approaches the true covariance matrix for large sample sizes. The formula is as follows.

$$C_{\hat{\theta}} = \left[\nabla f_m^{\top}\nabla f_m\right]^{-1}\left[\nabla f_m^{\top}\Lambda_m\nabla f_m\right]\left[\nabla f_m^{\top}\nabla f_m\right]^{-1}, \tag{2.41}$$

where ∇f_m is the partial derivative of the model with respect to the linear and nonlinear parameters. The partial derivative of the linear parameters is simply the regression matrix $\boldsymbol{\Phi}$, for the nonlinear parameters the Jacobian of the residuals can be reused. It can be derived that the derivative of the model with respect to the nonlinear parameters is the inverse of the residual sensitivity derived in Subsection 2.5.2:

$$\begin{aligned} \boldsymbol{r}_2 &= \boldsymbol{y} - \hat{\boldsymbol{y}}, \\ \frac{\partial}{\partial \alpha_i}\left[\boldsymbol{r}_2 = \boldsymbol{y} - \hat{\boldsymbol{y}}\right], \\ \frac{\partial \boldsymbol{r}_2}{\partial \alpha_i} &= -\frac{\partial \hat{\boldsymbol{y}}}{\partial \alpha_i}. \end{aligned} \tag{2.42}$$

Using these two facts, ∇f_m can be derived as follows: $\nabla f_m = \begin{bmatrix} -\boldsymbol{D}\boldsymbol{r}_2 & \boldsymbol{\Phi} \end{bmatrix}$. The second parameter in the equation for the covariance matrix is Λ_m, which is the auto-correlation matrix of the residuals. This is a Toeplitz matrix of size $m \times m$. Its entries are created from the auto-correlation sequence λ as $[\Lambda_m]_{ij} = \lambda_{i-j}$.

3

Research Questions

Due to significant contributions made by master students at Delft University of Technology, a framework for system identification of stall models, using flight data, exists. This essential groundwork enables the research of this thesis to focus on one key aspect, the nonlinear system identification routine. This directly leads to the research objective, which is defined as:

Research Objective

To improve the Citation II aerodynamic stall model accuracy by developing an improved nonlinear system identification routine.

Looking deeper into the research objective, it consists of two components. Firstly, the development of an improved nonlinear system identification routine. This starts by reflecting on the existing methods. To this effect, RQ 1 is formulated:

Research Question 1

What are the limitations and potential improvements of the current nonlinear system identification routine used for aerodynamic stall modeling?

Next, an investigation should be performed, on how the proposed method, separable nonlinear least squares, solves the limitations of the previous methods. Furthermore, the practicalities of applying separable nonlinear least squares to the problem of stall model identification must be worked out. This has not been done previously and requires further analysis. With this goal in mind, RQ 2 has been formulated:

Research Question 2

How can separable nonlinear least squares eliminate the limitations imposed by the current nonlinear system identification routine?

Note that RQ 2 leads to a qualitative comparison of the old and the new method. Furthermore, it explores the implementation of the method in MATLAB. The research question can be closed with a quantitative comparison of the metrics determined as limitations.

Looking back at the research objective, the second aspect deals with enhancing the existing stall models. To achieve this, the improved nonlinear system identification routine will be used to re-evaluate the existing data. To verify if any improvements are made a quantitative comparison will be done. This task is covered by RQ 3:

Research Question 3

How does the output of the new nonlinear system identification routine compare to that of the current routine?

RQ 3 tries to objectively compare methods by using the same data and model structures. However, using the new method new information might be uncovered. Throughout the project research into new model terms will be done. This leads to RQ 4:

Research Question 4

What new model components can be identified using the new nonlinear system identification routine?

Integral to the research project is the evaluation of the existing flight data. At any stage, data gaps can be uncovered and, depending on the availability of the aircraft, flight tests can be performed to fill the gaps. This aspect of the research is covered in RQ 5:

Research Question 5

What additional flight test data is required to enhance the Citation II aerodynamic stall model?

Using a combination of new methods, model terms and flight data a final model will be made. This model looks to improve on the existing models and a comparison will be made of the model terms, parameter variances, model statistics and time traces. This leads to RQ 6:

Research Question 6

How does the identified stall model compare to the current stall models?

4

Project Plan

4.1. Methodology

Past literature has created methodologies for system identification of Cessna Citation II stall characteristics. First Van Ingen [23] came up with a methodology for longitudinal dynamics using Kirchhoff's theory of flow separation first introduced by Goman and Khrabrov [34]. The workflow developed is described in Fig. 4.1. It uses the dependency of the lift coefficient C_L on the internal state variable X to solve for the parameters of the governing differential equation of X. After the identification of the *X-parameters*, the model structure identification takes place. If it is found that a different model structure is identified for the lift coefficient the X-parameter identification is redone. When this converges, the parameters of the model are identified.

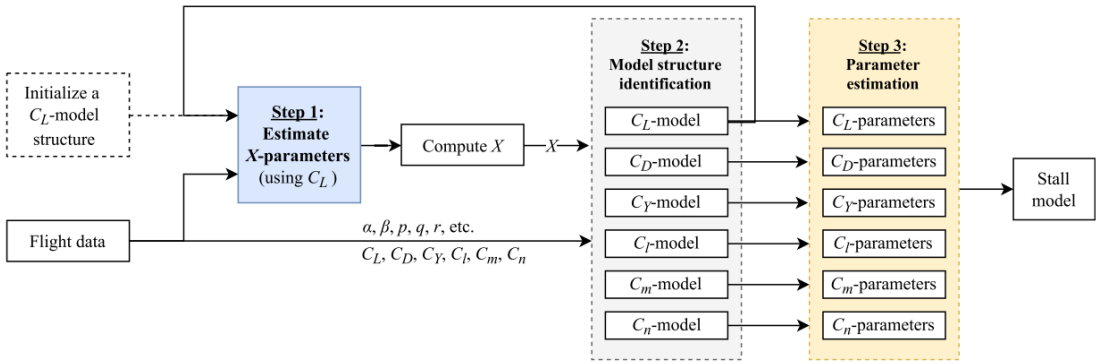

Figure 4.1: Stall model identification workflow developed by Van Ingen [23]

Building on previous work a deficiency in asymmetric stall modeling was recognized and tackled by De Fuijk [29]. It proposes a similar strategy as for the longitudinal model but uses a dependency of the roll moment coefficient on the local flow separation of the two wings. It converges on a model structure for C_l after wich all other model structures are selected and linear parameter estimation takes place. De Fuijk [29] found that the new methodology degrades the longitudinal dynamic model. He therefore proposes a hybrid methodology with separate separation models for longitudinal and asymmetric modes.

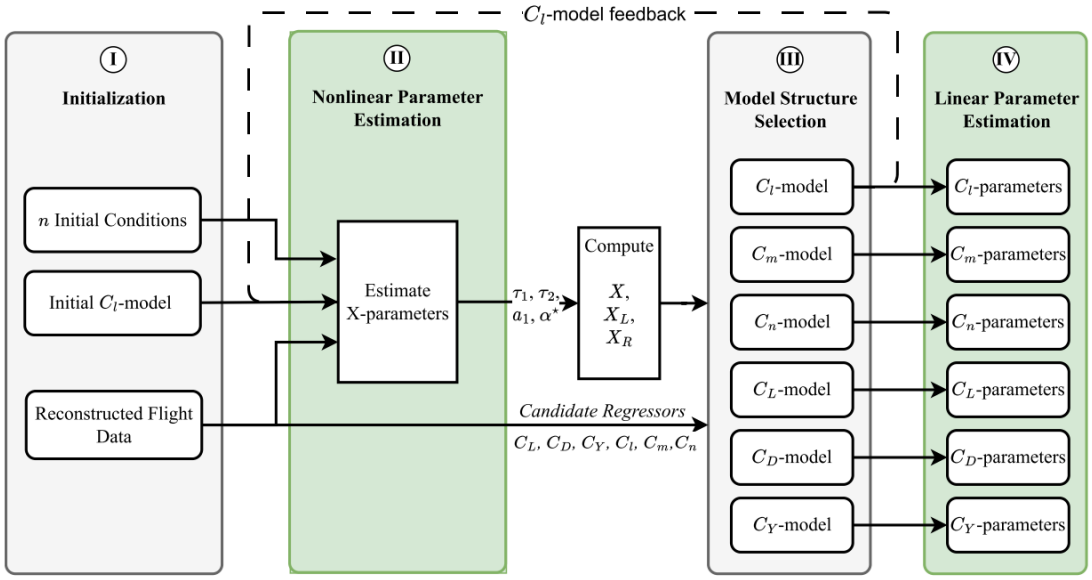

Figure 4.2: Stall model identification workflow developed by De Fuijk [29]

A major deficiency found in the previous workflows is in the optimization of the parameters. This was done through a nonlinear solver that solved for all parameters. For van Ingen and de Fuijk respectively:

$$\theta_{van,Ingen} = \begin{bmatrix} \tau_1 & \tau_2 & a_1 & \alpha^* & C_{L_0} & C_{L_\alpha} & C_{L_{\alpha^2}}, \end{bmatrix} \tag{4.1}$$

$$\theta_{de,Fuijk} = \begin{bmatrix} \tau_1 & \tau_2 & a_1 & \alpha^* & C_{l_0} & C_{l_\beta} & C_{l_r} & C_{l_{\delta_a}} & C_{l_{\Delta X}} \end{bmatrix}. \tag{4.2}$$

It can be seen that 7 or 9 parameters need to be resolved, depending on the model. Although previous work found a solution for the parameters, it did so suboptimally. This is evident from the post-optimization comparison with linear estimation methods. These show that, although well correlated, there are discrepancies between the nonlinear and the optimal OLS estimate. The discrepancies determined by De Fuijk [29] can be seen in Fig. 4.3. The previous methods solved this by doing an OLS on the linear parameters post-optimization. However, this does not guarantee global convergence.

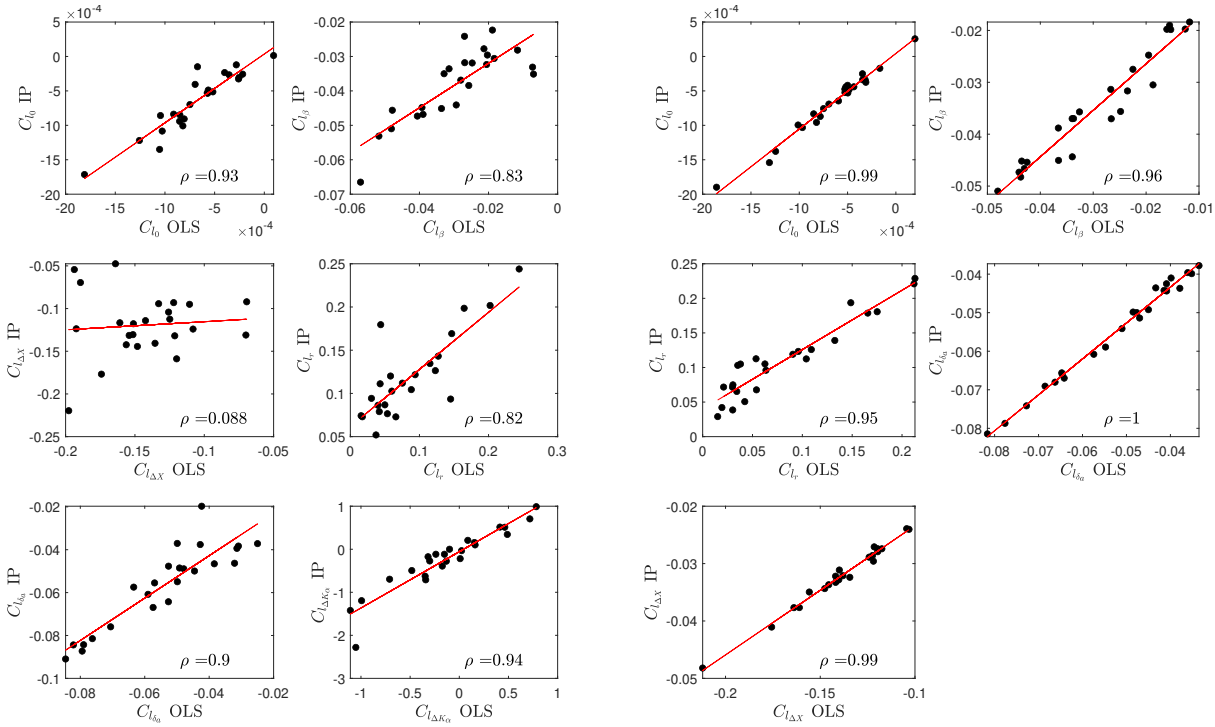

Figure 4.3: Correlation between linear and nonlinear parameter optimization (Adapted from [29])

An alternative approach can be taken by recognizing the linearity of all terms except τ_1, τ_2, a_1, and α^*. This methodology is based on separable nonlinear least squares and will be developed as part of this thesis.

After the successful implementation of the SNLS method, an exploration phase will start. In this phase, different ways of including multivariate splines are explored. The first option is to create a spline model for the aerodynamic coefficients (C_L, C_D, C_m, C_Y, C_l, C_n) directly, this is called the **Full Spline Model**. Alternatively, aerodynamic derivatives can be implemented as splines, Abramov et al. [14] found that C_{m_q}, for example, is a function of the angle of attack, this is called the **Hybrid Spline Model**. A third option is that improvements are found through the optimizer itself, this is called the **No Spline Model**.

4.2. Expected Results

The goal of this thesis is to implement an improved workflow for identifying stall models. The first major contribution is to reinvent the optimizer used to find the nonlinear parameters. Through improvements here, the identification of more complex model structures becomes possible. A promising direction is multivariate simplex splines, but not the only direction. Therefore, after successful implementation of SNLS an exploration phase will commence in which different opportunities of using the method are explored.

4.3. Planning

The global planning is visualized in Fig. 4.4. The development of SNLS is expected to be the major hurdle in the first phase of the thesis. After successful implementation, different applications are explored, referred to as **Full Spline Model**, **Hybrid Spline Model**, and **No Spline Model**.

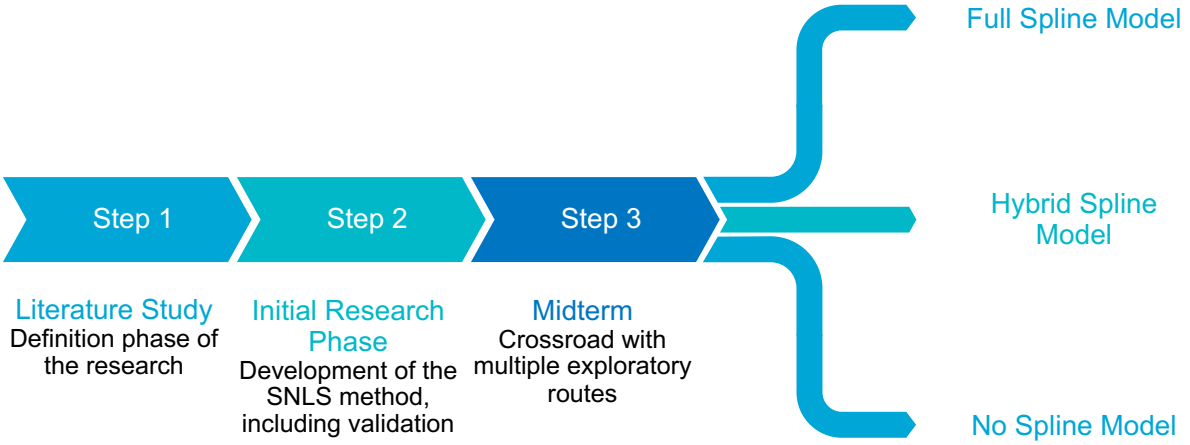

Figure 4.4: High level planning

Part II

Scientific Article

Improved Longitudinal Stall Modeling with Separable Nonlinear Least Squares and Dynamic Stall Maneuvers

Joey A. Herbold *
Delft University of Technology, Delft, Zuid-Holland, 2629HS, the Netherlands

Loss of control inflight is the most common cause of fatal accidents in aviation. Aerodynamic stall models are utilized in pilot training to enhance safety and prevent accidents. This research presents an advanced longitudinal stall model for the Cessna Citation II, achieved through innovations in modeling methodologies and experimental design. By introducing dynamic stall maneuvers with step inputs, the study mitigated τ_1 and τ_2 parameter correlation, enabling more reliable parameter identification. A separable nonlinear least squares method significantly reduced computational time for nonlinear stall model estimation, decreasing it from hours to seconds. This approach revealed two minimally correlated flow separation states, offering deeper insights into wing flow characteristics and improving model accuracy. The lift model was refined to incorporate pitch rate and elevator deflection effects, while the drag model was enhanced with a lift-induced drag component. Additionally, a center of pressure model was derived from pitching moment data, advancing the understanding of stability during stall. A novel structure for characterizing degraded elevator control effectiveness was also developed. These advancements resulted in substantial performance improvements, with mean squared errors for lift, drag, and pitch moment coefficients reduced by 32%, 29%, and 27%, respectively. The models also demonstrated greater consistency across diverse maneuvers, evidenced by reduced variability in R^2 values. This work contributes to more accurate stall modeling, enhancing both aerodynamic understanding and aviation safety.

Nomenclature

Abbreviations

FL	Flight level
LOC-I	Loss of control in-flight
MSE	Mean square error
OLS	Ordinary least squares
SNLS	Separable nonlinear least squares
UPRT	Upset prevention and recovery training

Roman Symbols

a_x,a_y,a_z	Accelerations in F_b [m/s^2]

a_1	Stall abruptness parameter [-]
b	Wing span [m]
$\bar{c}$	Mean aerodynamic chord [m]
$\boldsymbol{c}$	Linear parameters
C_D	Drag coefficient [-]
C_L	Drag coefficient [-]
C_m	Pitch moment coefficient [-]
C_N	Normal force coefficient for an airfoil [-]
C_X	Longitudinal force coefficient [-]
C_Z	Normal force coefficient for an aircraft [-]
$D*$	Fréchet derivative of $*$
F_*	Reference frame
I_*	Moment of inertia around $*$ axis [kgm^2]
$\boldsymbol{I}$	Inertia tensor [kgm^2]
K	Coefficient relating the pitch moment coefficient to the lift coefficient
$\boldsymbol{L}$	Loss function
m	Mass [kg]
p,q,r	Roll, pitch and yaw rate in F_b [rad/s]
$\boldsymbol{P}^{\perp}_{\boldsymbol{\Phi}(\boldsymbol{\theta})}$	Projector onto the orthogonal complement of the column space of $\boldsymbol{\Phi}(\boldsymbol{\theta})$
$\bar{q}$	Dynamic pressure [Pa]
$\boldsymbol{r}$	Residual vector
R^2	Coefficient of determination
$\mathbb{R}$	Set of real numbers
S	Wing surface area [m^2]
X	Separation state [-]
$\boldsymbol{X}$	Regression matrix for linear model
x,y,z	Coordinate in body reference frame [m]

Greek symbols

α	Angle of attack [rad]
α^*	Stall angle of attack [rad]
β	Angle of sideslip [rad]
$\delta_a,\delta_e,\delta_r$	Aileron, elevator and rudder deflection [rad]
$\boldsymbol{\theta}$	Nonlinear parameters
τ_1	Flow relaxation time constant [s]
τ_2	Delay of flow separation time constant [s]
$\boldsymbol{\Phi}$	Regression matrix for nonlinear model

Subscripts

$_0$	Static relation
$_0$	Bias term
$_a$	Aerodynamic reference frame
$_b$	Body reference frame
$_{c.g.}$	Center of gravity
$_{c.p.}$	Center of pressure
$_E$	Earth reference frame
$_{ss}$	Stall Strip
$_T$	Thrust
$_w$	Remainder of the wing

Superscripts

$\hat{}$	Model prediction
$\hat{}$	Optimal parameter estimate
$\dot{}$	Time derivative
$^+$	Moore-Penrose pseudo inverse

I. Introduction

Loss of control in-flight (LOC-I) remains a critical safety concern in aviation, responsible for a majority of fatal accidents over the past decades [1–4]. LOC-I occurs when a pilot is unable to maintain control and the aircraft deviates from its intended flight path. Stalls have been shown to be a common precursor to LOC-I incidents [5, 6]. In a study of 74 LOC-I accidents between 1993 and 2007, 36% were caused by aerodynamic stall [7]. If not correctly recognized, a stall can escalate into a more severe upset. Therefore, pilots' recognition of stalls is seen as a fundamental aspect of accident prevention [8]. The critical nature of stall recognition in LOC-I scenarios underscores the importance of effective upset prevention and recovery training (UPRT). Training goals have been put forward by the International Committee for Aviation Training in Extended Envelopes (ICATEE) [9] and are currently adopted by ICAO, FAA, and EASA [10–12]. Analysis of training goals showed that it is necessary to improve the aerodynamic models in stall regimes for flight simulator training devices [13].

There are two methods for the determination of stall models. The first is based on extensive wind tunnel testing and CFD analysis, for example, the simulation of upset recovery in aviation (SUPRA) project [14]. These projects are expensive due to the high complexity and extensive use of wind tunnels. Moreover, scaling effects complicate the interpretation of results. Alternatively, identification methods are used on flight test data. Stall model identification has been extensively researched at different research institutes and universities, such as the German Aerospace Center (DLR) [15–18], NASA [19], the Flight Test and Research Institute of the Brazilian Air Force [20, 21], and TU Delft [22–29].

Stall models generally combine differential equations to model flow separation with polynomial linear-in-the-parameters model structures to determine the aerodynamic forces resulting in a nonlinear optimization problem. This problem was previously solved in a multi-stage approach [30], which has been proven to be computationally expensive and often leads to local optima. The main contribution of this work is a novel model parameter estimation methodology that combines separable nonlinear least squares (SNLS) with Kirchhoff's theory of flow separation, allowing for more complex model structures that still converge to an optimal solution. Separable nonlinear least squares (SNLS) implicitly calculates the ordinary least squares (OLS) estimate for the linear parameters, which reduces the dimension of the nonlinear parameter space [31]. This is shown to improve the convergence rate [32].

The new parameter estimation technique is applied to the identification of a longitudinal dynamics model for the TU Delft's Cessna Citation II research aircraft. New flight tests have been performed for the new longitudinal model. The dynamic stall and deep dynamic stall aim to reduce the correlation between τ_1 and τ_2 which was found to be high with a new correlation calculation. Improvements are proposed to include local flow effects of the stall strips installed on the wing. Furthermore, elevator and pitch rate effects are incorporated into the model. A new approach involving the lift-induced drag is introduced for the drag model. The pitch model is upgraded by including a model for the shift in the center of pressure at high angles of attack. Lastly, a new model for elevator control effectiveness is identified.

This paper is organized as follows: Section II provides an overview of the prerequisites required for the rest of the

paper. Next, the developed methodology for this work is presented in Section III. This is followed by Section IV, which presents the results. A discussion is performed in Section V and finally, Section VI concludes the paper.

II. Background

A. Flight Test Vehicle

The Cessna Citation II callsign PH-LAB, is a research aircraft operated by Delft University of Technology. The aircraft is jointly owned by the University and the Netherlands Aerospace Center. The aircraft is used for educational and research purposes and offers a unique opportunity for stall model identification. Its general dimensions are presented in Table 1. Figure 1 shows a schematic view of the aircraft. The aircraft is outfitted with a custom flight test instrumentation system that logs aircraft states, a summary of the relevant sensed states is given in Table 2.

Table 1 General dimensions of the Cessna Citation II and mass and inertia properties at basic empty weight.

Dimensions	Value	Unit
b	15.75	m
$\bar{c}$	2.013	m
S	30.0	m^2
m	4161.3	kg
I_{xx}	12392	kgm^2
I_{yy}	31501	kgm^2
I_{zz}	41908	kgm^2
I_{xz}	2252.2	kgm^2

Note that values differ slightly from Van Ingen et al. [30] as they are derived directly from the manufacturer's manual

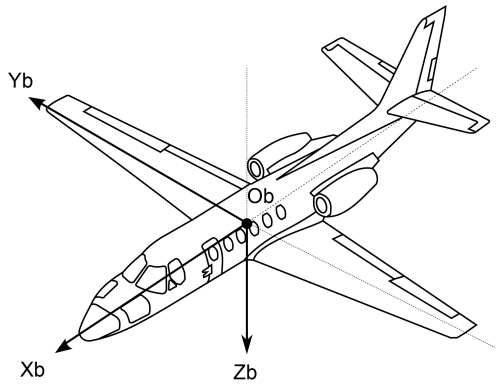

Fig. 1 Schematic view of the Cessna Citation II. Adapted from [30].

Table 2 Summary of the relevant sensing systems of the flight test instrumentation system.

System	Explanation	Measures	Variables	Unit	Sample rate
AHRS	Attitude & Heading Reference System	Aircraft Attitude	φ, θ, ψ	rad	52 Hz
		Body Rotation Rates	p, q, r	rad/s	
		Body Specific Forces	S_x, S_y, S_z	m/s^2	
Boom	Air Data Boom	Air Incidence Angles	α, β	rad	100 Hz
DADC	Digital Air Data Computer	True Airspeed	V_{TAS}	m/s	16 Hz
		Dynamic Pressure	$\bar{q}$	Pa	8 Hz
Engine	Engine Measurements	Rotational Rates	N_1, N_2	%	1000 Hz
		Fuel Mass Flow	$\dot{m}_f$	kg/s	
GPS	Global Positioning System	Position in F_E	x_E, y_E, z_E	m	1 Hz
		Velocity in F_E	$\dot{x}_E, \dot{y}_E, \dot{z}_E$	m/s	
Synchro	Angle Measurements	Control Surface Deflections	$\delta_a, \delta_e, \delta_r$	rad	100 Hz

B. Aerodynamic Coefficients

Aerodynamic coefficients express the aerodynamic forces and moments on the aircraft. These coefficients are dimensionless versions of the forces and moments themselves. In the body reference frame (see Appendix A), forces along X_b, Y_b and Z_b, can be defined as X^b, Y^b and Z^b respectively.

$$C_{X^b} = \frac{X^b}{\bar{q}S}, \quad C_{Y^b} = \frac{Y^b}{\bar{q}S}, \quad C_{Z^b} = \frac{Z^b}{\bar{q}S} \tag{1}$$

Equation (1) shows the non-dimensional forces in the body reference frame. In these equations, $\bar{q}$ refers to the dynamic pressure and S is the surface area of the wing.

$$C_l = \frac{L}{\bar{q}Sb}, \quad C_m = \frac{M}{\bar{q}S\bar{c}}, \quad C_n = \frac{N}{\bar{q}Sb} \tag{2}$$

Equation (2) shows the non-dimensional moments in the body reference frame. Here, b refers to the wingspan and $\bar{c}$ to the mean aerodynamic chord. Furthermore, the moments are defined as L, M, N around the axes X_b, Y_b and Z_b, respectively.

In the literature, it is also common to find the forces expressed in the aerodynamic reference frame (see Appendix A). The relationship between the reference frames is the rotation matrix $\mathbb{T}_{ab}$ (see Appendix A), which can convert the forces and moments in the body frame to those of the aerodynamic frame. The forces X^a and Z^a in the aerodynamic reference frame relate directly to the lift $L = -Z^a$ and the drag $D = -X^a$ of the aircraft.

Aerodynamic forces and moments cannot be measured directly in the aircraft. Instead, they are derived from the specific force and body rate data provided by the AHRS. The accelerations a_x, a_y, and a_z are derived from the specific force [23]. Acceleration is related to the sum of all forces on the vehicle. The gravitation and engine effects can be subtracted to isolate the aerodynamic force.

$$\begin{bmatrix} C_{X^b} \\ C_{Y^b} \\ C_{Z^b} \end{bmatrix} = \frac{1}{\bar{q}S} \left\{ m \begin{bmatrix} a_x^b \\ a_y^b \\ a_z^b \end{bmatrix} - m\mathbb{T}_{bE} \begin{bmatrix} 0 \\ 0 \\ g_0 \end{bmatrix} - \begin{bmatrix} X_T^b \\ Y_T^b \\ Z_T^b \end{bmatrix} \right\} \tag{3}$$

Equation (3) shows the force coefficients in the body frame. Here, m is the aircraft mass, which is time-varying and modeled by a mass model [33]. For the gravitational force, the assumption is made that the gravitational pull is constant regardless of altitude or geographical location. Furthermore, $\mathbb{T}_{bE}$ (see Appendix A) is a rotation matrix from the earth frame (see Appendix A) to the body frame. The thrust is defined in the body frame and calculated using an engine model provided by the manufacturer [33]. This model uses the Mach number M and the low-pressure turbine speed N_1 to calculate the thrust.

The aerodynamic moment coefficients can also be derived from the equations of motion. Here, the inertial and gyroscopic moments are taken into account. Furthermore, the moment caused by the thrust of the engines can be subtracted. Lastly, the equation can be non-dimensionalized.

$$\begin{bmatrix} C_l \\ C_m \\ C_n \end{bmatrix} = \frac{1}{\bar{q}S} \begin{bmatrix} 1/b & 0 & 0 \\ 0 & 1/\bar{c} & 0 \\ 0 & 0 & 1/b \end{bmatrix} \cdot \left\{ \boldsymbol{I} \cdot \begin{bmatrix} \dot{p} \\ \dot{q} \\ \dot{r} \end{bmatrix} + \begin{bmatrix} p \\ q \\ r \end{bmatrix} \times \boldsymbol{I} \cdot \begin{bmatrix} p \\ q \\ r \end{bmatrix} - \begin{bmatrix} x_{engine} - x_{cg} \\ y_{engine} - y_{cg} \\ z_{engine} - z_{cg} \end{bmatrix} \times \begin{bmatrix} X_T^b \\ Y_T^b \\ Z_T^b \end{bmatrix} \right\} \tag{4}$$

Equation (4) shows the aerodynamic moment coefficients in the body frame. Here, p, q, and r are the roll, pitch, and yaw rates respectively. Their time derivatives are $\dot{p}$, $\dot{q}$, $\dot{r}$. The moments of inertia of the aircraft are stored in matrix $\boldsymbol{I}$, which is time-varying and modeled by the mass model [33]. The moment caused by the engine thrust uses the engine model, engine positions, and time-varying center of gravity modeled by the mass model.

C. Theory of Flow Separation

To link the aircraft state to the aerodynamic forces and moments at high angles of attack an intermediary is required. Additional states, in the form of flow separation states, are included to model the changing behavior at high angles of attack. First, a connection between the angle of attack and state of flow separation is established in Section II.C.1. Then, the new flow separation state is connected to the forces and moments in Section II.C.2.

1. Flow Separation Models

The most prominent model in aircraft stall modeling is based on Kirchhoff's theory of flow separation. This model, introduced by Goman and Khrabrov [34], connects the degree of flow separation (X) and aerodynamic forces and moments. The degree of flow separation is measured as the normalized chord-wise distance at which the flow separates, $X = 1$ for attached flow and $X = 0$ for separated flow. Goman and Khrabrov noted that unsteady aerodynamic effects can cause relaxation and delay of flow separation. The following first-order differential equation can model these effects:

$$\tau_1 \frac{dX}{dt} + X = X_0(\alpha - \tau_2 \dot{\alpha}) \tag{5}$$

Here, τ_1 and τ_2 are time constants modeling relaxation and delay of flow separation, respectively. The static relationship between flow separation and angle of attack is modeled by X_0. This relation can be estimated from static wind tunnel data or identified from flight data if a model structure is assumed. Multiple model structures have been proposed [35, 36], however, in this work the model structure introduced by Fischenberg [15] is used:

$$X_0(\alpha) = \frac{1}{2} \left\{ 1 - \tanh\left(a_1 \left(\alpha - \alpha^* \right) \right) \right\} \tag{6}$$

where a_1 models the abruptness of the stall and α^* is the angle of attack at which flow separation reaches the mid chord. Using this information, three different flow separation models can be defined. Firstly, a steady flow separation model can be defined, where none of the previously mentioned unsteady effects are modeled, in other words, $\tau_1 = \tau_2 = 0$. Next, a quasi-steady model, for which τ_2 can be non-zero and delay of flow separation is modeled. Lastly, the full unsteady model for which τ_1 and τ_2 can be non-zero. These three model structures and corresponding model parameters are summarized in Table 3.

Table 3 Different flow separation models and their corresponding model parameters.

Separation model	Parameters
Steady	a_1, α^*
Quasi-steady	τ_2, a_1, α^*
Unsteady	τ_1, τ_2, a_1, α^*

2. Force and Moment Reconstructions

Reconstructions of the aerodynamic forces and moments can be made using the state of flow separation. Initial research efforts focused on the forces and moments on airfoils. Woods [37] mentions the lift coefficient for trailing edge flow separation as:

$$C_L = 2\pi \left(\frac{1 + \sqrt{X}}{2} \right)^2 \alpha \tag{7}$$

Here, 2π is the lift curve slope in thin airfoil theory [38, p. 352] and α the angle of attack. This relation is widely accepted in aircraft stall modeling [18, 30, 34]. Next to the lift coefficient, Woods [37] defines an expression for the drag coefficient:

$$C_D = 2\pi \left(\frac{1 - \sqrt{X}}{2} \right)^2 \alpha^2 \tag{8}$$

Moving on, Leishman and Beddoes [35] have created a relation between the pitch moment coefficient C_m and the normal force coefficient C_N. In the context of aircraft, K_0 models the distance between the center of gravity and the aerodynamic center of the wing, K_1 models the shift in the center of pressure due to flow separation, and K_2 is used to describe the typical moment break of the stall. Note that a zero-lift moment C_{m_0} may be added to the model.

$$C_m = \left[K_0 + K_1(1 - X) + K_2 \sin(\pi X^m) \right] C_N \ \ (+C_{m_0}) \tag{9}$$

Other formulations for the pitching moment also exist. Singh and Jategaonkar [16] propose a very similar term but uses the lift coefficient instead of the normal force coefficient. Additionally, the K_0 term is neglected.

$$C_m = C_L \left[K_1 (1 - X) + K_2 \sin(\pi X^m) \right] \tag{10}$$

It is not the only term for the pitching moment coefficient put forward by Singh and Jategaonkar [16]. An alternative formulation is derived from Goman and Khrabrov [34], who propose the following:

$$C_m = \frac{\pi}{2} \alpha \left(1 + \sqrt{X}\right)^2 \frac{5\left(1 - \sqrt{X}\right)^2 + 4\sqrt{X}}{16} \tag{11}$$

This formula was then adapted by Singh and Jategaonkar [16]. They add a constant term $\frac{1}{4}$ to multiply the lift coefficient by.

$$C_m = C_L \left(\frac{5\left(1 - \sqrt{X}\right)^2 + 4\sqrt{X}}{16} - \frac{1}{4} \right) \tag{12}$$

The models and model terms introduced in this section will be used later in the paper to explore different model structures.

III. Methodology

Over the past ten years, a stall model identification workflow has been developed at Delft University of Technology. A high-level overview is visualized in Fig. 2. As can be seen, the workflow can be broken down into five major steps. First, data must be collected through flight test experiments. This is done with the Citation PH-LAB. The design of flight test experiments will be discussed in Section III.A. Using the data collected in flight, a spectral analysis can be performed to analyze the buffet vibrations. The buffet model is created by fitting a curve to the power spectra of the normal and lateral accelerations [39]. Using the results of the buffet analysis, the buffet effects can be filtered out and flight path reconstruction can be performed, see Section III.B.

Phases 4 and 5 are the main subject of this paper. Stall model identification, phase 4 is further detailed in Fig. 3. As can be seen in the diagram, first a model structure is assumed. The selection of the best model structure is discussed in Section III.C. Using the assumed model structure of the lift coefficient and flow separation states, nonlinear parameter estimation is performed with SNLS. Details of the SNLS method are discussed in Section III.D. With the estimated flow separation models the flow separation states can be determined. This is used as an input for the linear parameter estimation for the other models C_D and C_m. Linear parameter estimation is performed using OLS and is discussed in Section III.E. Only longitudinal force and moment coefficients are mentioned, but the workflow can be extended to include lateral dynamics. After the identification, the model must be validated using additional flight data. This is discussed in Section IV.D.

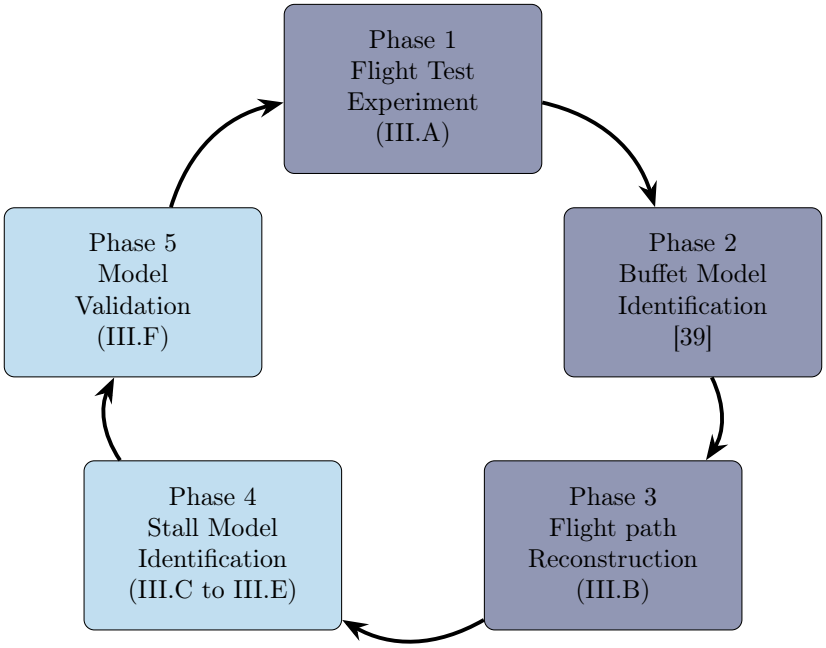

Fig. 2 System identification workflow for stall modeling. Phases four and five are the primary subjects of this research.

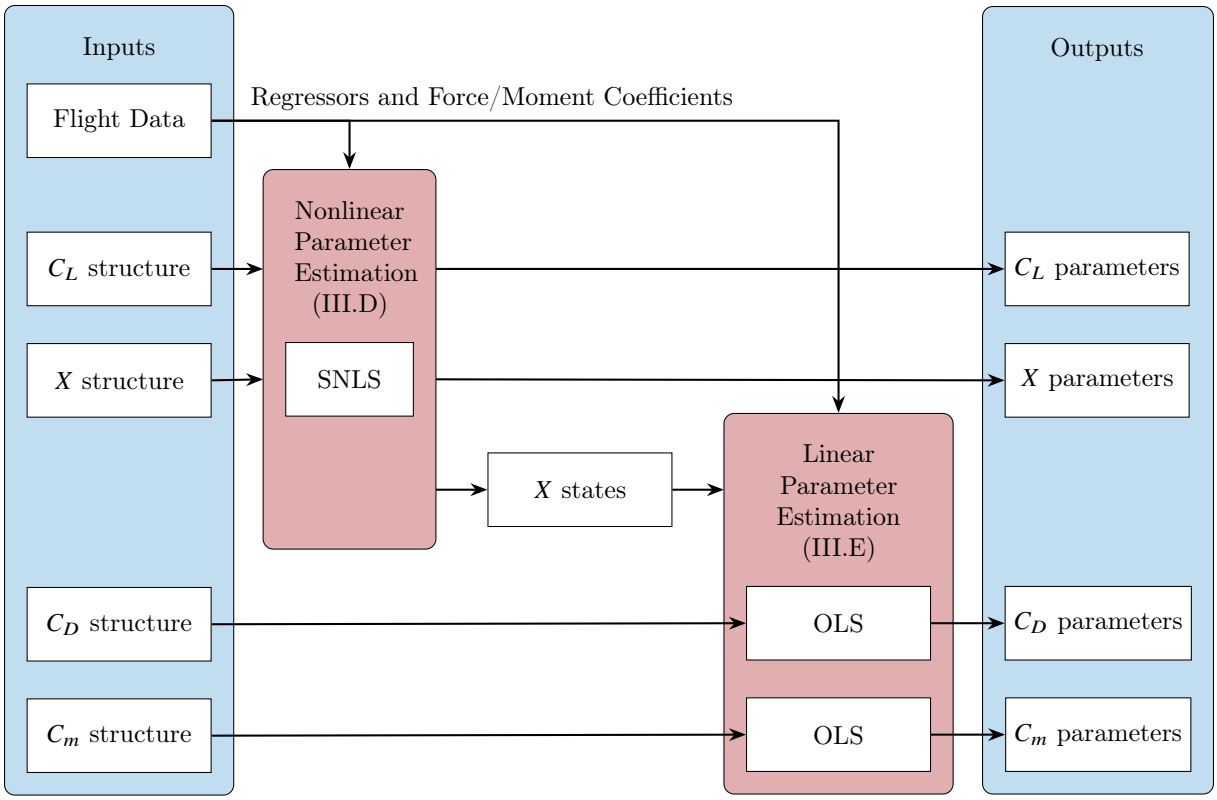

Fig. 3 Detailed description of the stall model identification workflow.

A. Flight Test Experiments

Using the covariance calculations from Section III.D, the correlation between τ_1 and τ_2 was re-evaluated. With this new formulation, the correlation is determined at 0.73. This was likely missed by Van Ingen et al. [30] because τ_2 ran into the lower bound of the optimization problem. This bound masked the true correlation between τ_1 and τ_2 when calculated on the resulting samples. To mitigate the correlation, new flight tests were necessary. Two new maneuvers were designed to eliminate this correlation: the dynamic and the deep dynamic stall. These maneuvers are derived from Singh and Jategaonkar [16] and adapted to fit the Citation.

The dynamic stall maneuver, depicted in Fig. 4a, starts with a smooth positive angle of attack rate. During the approach to stall, sequential step inputs are given to the elevator, ailerons, and rudder. These events are visible in Fig. 4a at annotations 1,2, and 3, respectively. The aircraft is stabilized before the aircraft enters the stall. Oscillating elevator inputs are applied to enter and exit the stall, starting at annotation 4. This gives the most information on the transition into and out of the stall.

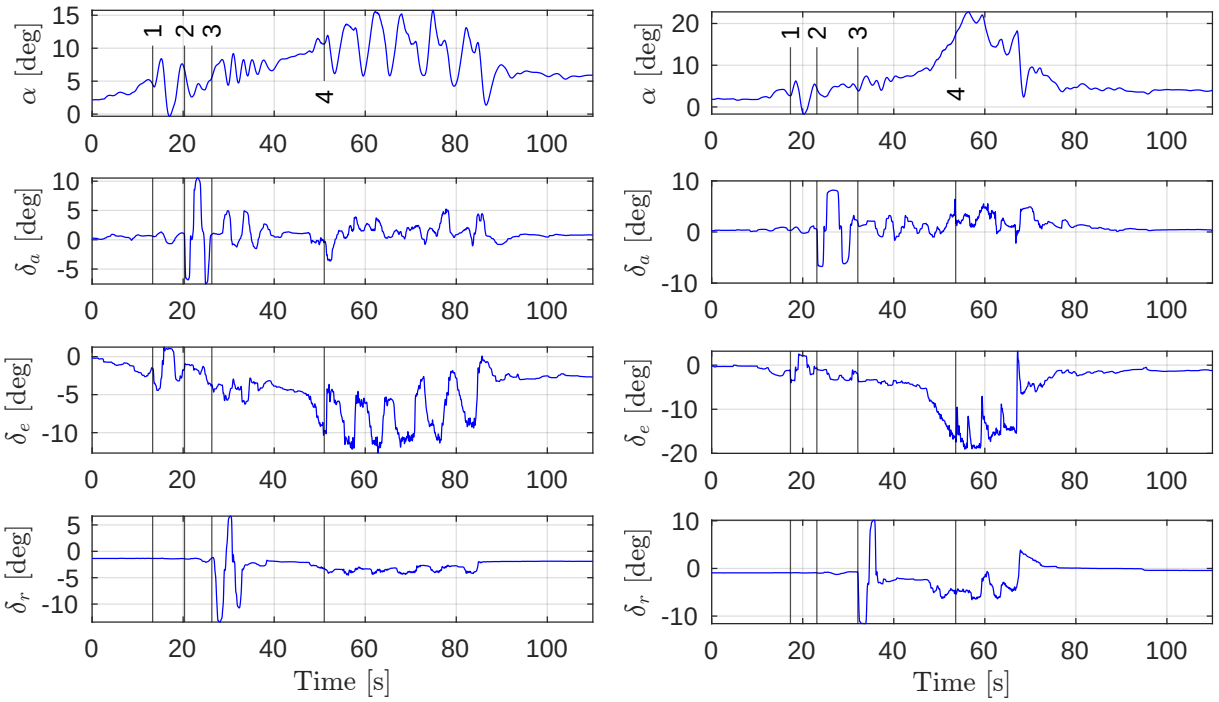

(a) Dynamic stall maneuver **(b) Deep dynamic stall maneuver**

Fig. 4 New stall maneuvers performed for this research.

The deep dynamic stall maneuver follows the same initial steps, as can be seen in Fig. 4b. Starting with a smooth positive angle of attack rate and sequential step inputs, again annotated with 1,2, and 3. The elevator is held to keep the aircraft in the stall. Once the angle of attack reaches 18° to 20°, oscillating elevator inputs are given. The oscillations are seen at annotation 4 as short spikes of lower deflection. Significant elevator deflection is needed to keep the aircraft

in the stall, which compromises the pilots' ability to oscillate the elevator.

Table 4 shows the data sets used in this research. First, a recap is given of the data set defined by Van Ingen et al. [30]. This prior data set is supplemented with five dynamic stalls and seven deep dynamic stalls. These were flown between flight levels 150 and 200. The data is split into a training and validation set using an 80%-20% ratio.

Table 4 Overview of the flight maneuvers used in this paper. The division into a training and validation set is also described.

Data set	FL	Maneuver Type	Reps	Training Set	Validation Set	Used In
Van Ingen [30]	80-110	Quasi-steady stall	2	1,2		
	110-150	Quasi-steady stall	4	3,4,6	5	IV.A
	150-200	Quasi-steady stall	28	8-11,13-15,17-21,24,26-34	7,12,16,22,23,25	
This Work	80-110	Quasi-steady stall	2	1,2		
	110-150	Quasi-steady stall	4	3,4,5,6		
	150-200	Quasi-steady stall	28	8-11,13-15,17-21,24,26-34	7,12,16,22,23,25	IV.B to IV.D
	150-200	Dynamic stall	5	35-37	38,39	
	150-200	Deep dynamic stall	7	40-45	46	

B. Flight Path Reconstruction

Reconstructing the flight path is essential for a good identification result of aircraft systems. Sensors will introduce noise, bias, and drift, which causes errors when using the measurements directly. Kalman filtering minimizes these errors, by using a prediction model in combination with the measurements. An unscented Kalman filter is used for the state reconstruction of the Citation. The workings of this filter have been worked out in detail by Van Horssen [22] and Van Ingen [23].

Table 5 A summary of the cut-off frequencies used for the low-pass filters.

Signals	f_c [Hz]
a_x, a_y, r, δ_r	4
p, q, δ_a	5
δ_e, α, β	6
a_z	8

Some signals are strongly affected by the aerodynamic buffet, signal pre-processing must be applied to eliminate these effects [40]. This can be done using a low-pass filter. In previous research, a fourth-order Butterworth filter was used [30]. This choice is retained, although the cut-off frequencies are adjusted based on a new analysis [41]. In this analysis, the idea is to filter only as much as needed and preserve as much of the signal as possible. This is important when considering unsteady effects of unknown frequency. A summary of the new cut-off frequencies is presented in Table 5.

C. Model Structure

In this section, candidate models are defined to achieve specific objectives. First, the studied flow separation models are defined in Section III.C.1. Then, the proposed lift, drag, and pitch moment models are discussed in Sections III.C.2 to III.C.4.

1. Separation Models

As expressed in Section II.C, stall models typically use the state of flow separation on the wing and connect it to the aerodynamic forces and moments. This simplification stems from two-dimensional aerodynamics, however, it has proven effective for aircraft too [30]. Early-stage stall models have used one flow separation parameter for the entire aircraft [15, 30]. Later, multiple flow separation parameters were explored, but only to model asymmetric effects [17, 29]. In this work, multiple flow separation parameters are proposed for the longitudinal stall model. It is believed that previous results found by Van Ingen et al. [30] do not model a full-wing stall, but the effects of the stall strips installed on the Citation. A diagram of the stall strip can be seen in Fig. 5. The stall strip provides control of when and where the stall happens on the wing. The hypothesis would explain the low stall angle of attack found in previous work ($\alpha^* \approx 12°$) [30], which does not align with prior knowledge of the airfoils of the wing. The Citation uses NACA23014 and NACA23012 airfoils. Wind tunnel data for the NACA23012 airfoil points out that for an infinite wing at Reynolds numbers of 3.4×10^6, the stall angle of attack is at 15°. Furthermore, for a finite wing with an aspect ratio of 6, they found a stall angle of attack of 20° [42]. The Citation with an aspect ratio of 8.3 must fall somewhere in between the two.

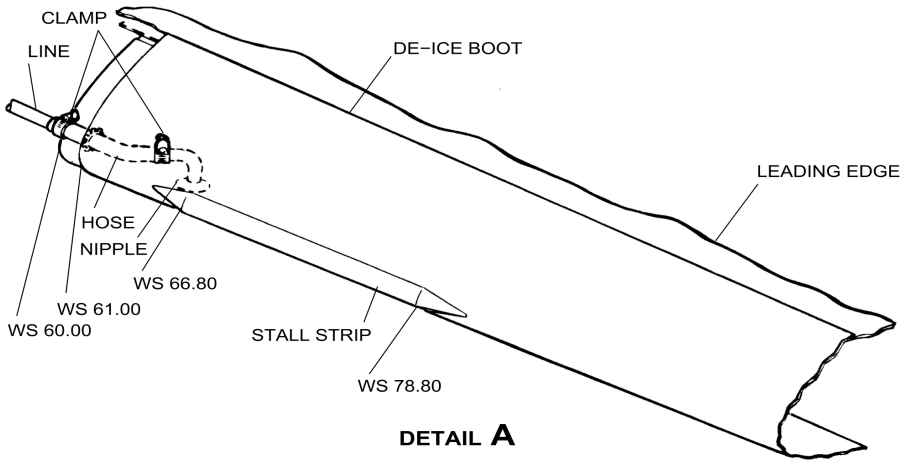

Fig. 5 Diagram of the stall strip installed on the de-ice boot on the leading edge of the wing. Adapted from the Cessna Citation II maintenance manual.

2. Lift Model

Four goals are defined for the estimation of a new lift model. To evaluate these goals, six new models will be estimated, for which the model structures are summarized in Table 18 in Appendix B. The first goal is to evaluate the effectiveness of the new SNLS method. To make this evaluation, the model structure of Van Ingen et al. [30] is re-estimated using SNLS. This re-estimated model will be referred to as **Model CL-I**. The second goal is to evaluate if the previously used second-order spline term is necessary or an artifact of the previous nonlinear parameter estimation technique. To achieve this, the term is removed in **Model CL-II**. The third goal is to evaluate the addition of the second flow separation state, this is done through **Model CL-III**. The last goal is to re-evaluate the contributions of pitch rate q and elevator deflection δ_e. Three models are created for this. **Model CL-IV** evaluates the contribution of q. **Model CL-V** does this for δ_e and **Model CL-VI** takes into account both simultaneously.

3. Drag Model

For the drag model, five objectives are set and fourteen models are defined. The model structures are summarized in Table 19 in Appendix B. As a first test, the model found by Van Ingen et al. [30] is re-estimated. This is referred to as **Model CD-I**. This re-estimation goes hand in hand with the re-estimation of **Model CL-I**. For the second objective, the same model is identified with the addition of a second flow separation term, this is **Model CD-II**. This gives an indication of the impact of the second flow separation state.

For analysis beyond the previous, it is chosen to include four terms by default: C_{D_0}, $C_{D_{q^*}}$, $C_{D_{\delta_e}}$ and $C_{D_{C_T}}$. A t-test is performed after the parameter estimation, if the hypothesis of the t-test is accepted for any parameter the model is re-estimated without the parameter. To set a baseline, the four terms are supplemented with the terms $(1 - X_{ss})$ and $(1 - X_w)$ to add stall effects. This model is referred to as **Model CD-III**.

Objective three is to analyze the relation of C_D with the angle of attack α. In previous work, a linear dependency on α was found [30]. However, it would make sense for a quadratic relation to exist, as otherwise, the drag becomes negative for negative angles of attack. For this reason, three models are suggested for comparison. The first adds a term α to the baseline and is called **Model CD-IV**. The second adds α^2 and is called **Model CD-V**. Lastly, **Model CD-VI** adds both α and α^2.

An alternative to including the angle of attack is to include the lift coefficient. Objective four is to understand the effect of including the lift coefficient as a regressor. For this, the best-performing lift coefficient model will be used as an input for the drag model. The lift coefficient model already includes stall effects. For this reason, the inclusion of C_L and C_L^2 will be tested with and without the $(1 - X_{ss})$ and $(1 - X_w)$ dependencies. This leads to six distinct models, **Model CD-VII** through **Model CD-XII**. Lastly, the drag term derived from Kirchhoff flow by Woods [37] is explored. This term also has a dependency on the state of flow separation and thus it is tested with and without the inclusion of $(1 - X_{ss})$ and $(1 - X_w)$, respectively **Model CD-XIII** and **Model CD-XIV**.

4. Pitch Moment Model

For the pitch moment model, multiple experiments are defined. First, the model by Van Ingen et al. [30] is re-estimated. This model is referred to as **Model Cm-I**. This model is identified in combination with **Model CL-I** and shows the effect of the new SNLS method.

Next, an exploration of the models proposed by Leishman and Beddoes [35] and Singh and Jategaonkar [16] is performed. Using components of their models, six base regressors are defined. First, K_0 models the moment arm between the center of gravity and the center of pressure. Then, K_1 models the shift of the center of pressure as a function of the state of flow separation. The term K_2^m is used to modify the moment to model pitch break at moment stall, here the value of m can be 1/2, 1, or 2. Lastly, K_S refers to a term proposed by Singh and Jategaonkar [16]. These six regressors are combined in fourteen ways and lead to **Model Cm-II** up to **Model Cm-XV**.

Table 6 Summary of the regressors studied in this work for the pitch moment coefficient. Note C_{m_0}, $C_{m_{C_T}}$, $C_{m_{q^*}}$ and $C_{m_{\delta_e}}$ are included by default.

Identifier	**Regressors**	
K_0	C_L	$x_{c.g.}/\bar{c}C_L$
K_1	$(1 - X_{ss})C_L$	$(1 - X_w)C_L$
$K_2^{1/2}$	$\sin(\pi X_{ss}^{1/2})C_L$	$\sin(\pi X_w^{1/2})C_L$
K_2^1	$\sin(\pi X_{ss}^1)C_L$	$\sin(\pi X_w^1)C_L$
K_2^2	$\sin(\pi X_{ss}^2)C_L$	$\sin(\pi X_w^2)C_L$
K_S	$\frac{5\left(1-\sqrt{X_{ss}}\right)^2+4\sqrt{X_{ss}}}{16}C_L$	$\frac{5\left(1-\sqrt{X_w}\right)^2+4\sqrt{X_w}}{16}C_L$
$(1 - X)$	$(1 - X_{ss})$	$(1 - X_w)$
$X\delta_e$	$X_{ss}\delta_e$	$X_w\delta_e$

Fischenberg and Jategaonkar [18] describe an empirical pitch moment model that includes $(1 - X)$ as a regressor. To study the inclusion of this term, **Model Cm-XVI** is defined. Furthermore, the combination of this term with previously defined regressors is studied, leading to fourteen additional model structures. These are **Model Cm-XVII** up to **Model Cm-XXX**.

The last objective is to define a new method for including stall-related elevator effectiveness reduction. To model this, a cross term of the elevator deflection δ_e and state of flow separation X_{ss} or X_w is defined. Collectively this is referred to as $X\delta_e$ but consists of two terms as can be seen in Table 6. These terms are added to the previously defined models to create 29 new models, **Model Cm-XXXI** up to **Model Cm-LXIX**. A summary of all model structures used can be found in Table 20 in Appendix B.

D. Nonlinear Parameter Estimation - Separable Nonlinear Least Squares

SNLS can be used to estimate the nonlinear parameters corresponding to the flow separation states. SNLS is a subset of nonlinear least squares problems, characterized by the ability to separate the model into linear and nonlinear components, which reduces computational load compared to full nonlinear optimization [32]. This separation is possible due to the following structure:

$$\hat{\boldsymbol{Y}} = f_m(\boldsymbol{x}, \boldsymbol{c}, \boldsymbol{\theta}) = \boldsymbol{\Phi}(\boldsymbol{x}, \boldsymbol{\theta}) \cdot \boldsymbol{c} \tag{13}$$

Here, $\boldsymbol{c} \in \mathbb{R}^n$ is a set of linear parameters and $\boldsymbol{\theta} \in \mathbb{R}^k$ is a set of nonlinear parameters. Furthermore, $\boldsymbol{\Phi}$ is a regression matrix, which is a function of the aircraft state $\boldsymbol{x}$ and nonlinear parameters $\boldsymbol{\theta}$. The dependency on the aircraft state $\boldsymbol{x}$ will be dropped in further equations to be concise. Lastly, $\hat{\boldsymbol{Y}}$ are the estimated outputs of the model at each data point. As with any least squares problem, the cost function is the sum of the squared residuals:

$$\boldsymbol{L}(\boldsymbol{c}, \boldsymbol{\theta}) = \|\boldsymbol{Y} - \boldsymbol{\Phi}(\boldsymbol{\theta}) \cdot \boldsymbol{c}\|^2 \tag{14}$$

Here, $\boldsymbol{Y}$ are the observed outputs at each data point. The structure allows for solving the linear parameters $\boldsymbol{c}$ as if it were an ordinary linear least squares problem. However, due to the dependency of $\boldsymbol{\Phi}$ on $\boldsymbol{\theta}$ the optimal estimate of $\boldsymbol{c}$ will also be dependent on $\boldsymbol{\theta}$. The least squares solution looks as follows:

$$\hat{\boldsymbol{c}}(\boldsymbol{\theta}) = \boldsymbol{\Phi}(\boldsymbol{\theta})^+ \cdot \boldsymbol{Y} \tag{15}$$

This optimal estimate can then be substituted in Eq. (14) which reduces the number of parameters to estimate from $n + k$ to k. Golub and Pereyra [31] proved that this reduction is valid and that when the reduced problem is solved for an optimal $\hat{\boldsymbol{\theta}}$ this also results in an optimal $\hat{\boldsymbol{c}}$, which minimizes the cost function globally. The reduced problem takes the following form:

$$\boldsymbol{L}(\boldsymbol{\theta}) = \|\boldsymbol{Y} - \boldsymbol{\Phi}(\boldsymbol{\theta}) \cdot \boldsymbol{\Phi}(\boldsymbol{\theta})^+ \cdot \boldsymbol{Y}\|^2 = \|\boldsymbol{P}^{\perp}_{\boldsymbol{\Phi}(\boldsymbol{\theta})} \cdot \boldsymbol{Y}\|^2 = \|\boldsymbol{r}(\boldsymbol{\theta})\|^2 \tag{16}$$

Here, $\boldsymbol{P}^{\perp}_{\boldsymbol{\Phi}(\boldsymbol{\theta})}$ signifies the projector onto the orthogonal complement of the column space of $\boldsymbol{\Phi}(\boldsymbol{\theta})$, defined as $\boldsymbol{I} - \boldsymbol{\Phi}(\boldsymbol{\theta})\boldsymbol{\Phi}(\boldsymbol{\theta})^+$. This effectively eliminates all contributions of the model proportional to the columns in $\boldsymbol{\Phi}(\boldsymbol{\theta})$, isolating the nonlinear contributions. Furthermore, $\boldsymbol{r}(\boldsymbol{\theta})$ is introduced as the residual vector, defined as $\boldsymbol{P}^{\perp}_{\boldsymbol{\Phi}(\boldsymbol{\theta})} \cdot \boldsymbol{Y}$.

The reduced problem can be solved with the nonlinear least squares tool in MATLAB*. This uses the trust-region-reflective method to find a minimum to the least squares problem. This method requires the formation of a Jacobian matrix, which provides the sensitivity of $\boldsymbol{r}(\boldsymbol{\theta})$ to the parameters $\boldsymbol{\theta}$. This is used to define the next step in the algorithm.

*https://nl.mathworks.com/help/optim/ug/lsqnonlin.html

The Jacobian of the residuals is defined in Eq. (17), where the dependency on $\boldsymbol{\theta}$ was dropped for convenience.

$$\mathbf{D}\boldsymbol{r} = -(\boldsymbol{P}_{\boldsymbol{\Phi}}^{\perp} \cdot \mathbf{D}\boldsymbol{\Phi}) \cdot \boldsymbol{\Phi}^{+} \cdot \boldsymbol{Y} - (\boldsymbol{\Phi}^{+})^{\top} \cdot (\boldsymbol{P}_{\boldsymbol{\Phi}}^{\perp} \cdot \mathbf{D}\boldsymbol{\Phi})^{\top} \cdot \boldsymbol{Y} \tag{17}$$

$\mathbf{D}$ defines the Fréchet derivative which is a generalization of derivatives in normed spaces [43]. This allows for the derivative of $\boldsymbol{\Phi}(\boldsymbol{\theta}) : \mathbb{R}^k \to \mathbb{R}^{(m \times n)}$ to be taken as $\mathbf{D}\boldsymbol{\Phi}(\boldsymbol{\theta}) : \mathbb{R}^k \to \mathbb{R}^{(m \times n \times k)}$ where $\mathbf{D}\boldsymbol{\Phi}(\boldsymbol{\theta})_{ijq} = \frac{\partial \Phi_{ij}(\boldsymbol{\theta})}{\partial \alpha_q}$. A novel expression for $\boldsymbol{Dr}$ equivalent to Eq. (17) that reduces memory storage is presented:

$$\mathbf{D}\boldsymbol{r} = -\mathbf{D}\boldsymbol{\Phi} \cdot \hat{\boldsymbol{c}} + \boldsymbol{\Phi} \cdot (\boldsymbol{\Phi}^{+} \cdot (\mathbf{D}\boldsymbol{\Phi} \cdot \hat{\boldsymbol{c}})) - (\boldsymbol{\Phi}^{+})^{\top} \cdot (\mathbf{D}\boldsymbol{\Phi})^{\top} \cdot \boldsymbol{r} \tag{18}$$

Proof. Equation (17) consists of two segments: $\boldsymbol{Dr} = -J_1 - J_2$. These segments can be refactored separately. Starting with J_1:

$$\begin{aligned}
J_1 &= (\boldsymbol{P}_{\boldsymbol{\Phi}}^{\perp} \cdot \mathbf{D}\boldsymbol{\Phi}) \cdot \boldsymbol{\Phi}^{+} \cdot \boldsymbol{Y} && \\
J_1 &= (\boldsymbol{P}_{\boldsymbol{\Phi}}^{\perp} \cdot \mathbf{D}\boldsymbol{\Phi}) \cdot \hat{\boldsymbol{c}} && (\hat{\boldsymbol{c}} = \boldsymbol{\Phi}^{+} \cdot \boldsymbol{Y}) \\
J_1 &= ((I - \boldsymbol{\Phi} \cdot \boldsymbol{\Phi}^{+}) \cdot \mathbf{D}\boldsymbol{\Phi}) \cdot \hat{\boldsymbol{c}} && (\boldsymbol{P}_{\boldsymbol{\Phi}}^{\perp} = I - \boldsymbol{\Phi} \cdot \boldsymbol{\Phi}^{+}) \\
J_1 &= \mathbf{D}\boldsymbol{\Phi} \cdot \hat{\boldsymbol{c}} - \boldsymbol{\Phi} \cdot (\boldsymbol{\Phi}^{+} \cdot (\mathbf{D}\boldsymbol{\Phi} \cdot \hat{\boldsymbol{c}})) && \text{(refactor)}
\end{aligned}$$

Next, J_2 can be refactored:

$$\begin{aligned}
J_2 &= (\boldsymbol{\Phi}^{+})^{\top} \cdot (\boldsymbol{P}_{\boldsymbol{\Phi}}^{\perp} \cdot \mathbf{D}\boldsymbol{\Phi})^{\top} \cdot \boldsymbol{Y} && \\
J_2 &= (\boldsymbol{Y}^{\top} \cdot \boldsymbol{P}_{\boldsymbol{\Phi}}^{\perp} \cdot \mathbf{D}\boldsymbol{\Phi} \cdot \boldsymbol{\Phi}^{+})^{\top} && \text{(double transpose)} \\
J_2 &= (\boldsymbol{Y}^{\top} \cdot (I - \boldsymbol{\Phi} \cdot \boldsymbol{\Phi}^{+}) \cdot \mathbf{D}\boldsymbol{\Phi} \cdot \boldsymbol{\Phi}^{+})^{\top} && (\boldsymbol{P}_{\boldsymbol{\Phi}}^{\perp} = I - \boldsymbol{\Phi} \cdot \boldsymbol{\Phi}^{+}) \\
J_2 &= ((\boldsymbol{Y}^{\top} - \boldsymbol{Y}^{\top} \cdot \boldsymbol{\Phi} \cdot \boldsymbol{\Phi}^{+}) \cdot \mathbf{D}\boldsymbol{\Phi} \cdot \boldsymbol{\Phi}^{+})^{\top} && \text{(refactor)} \\
J_2 &= ((\boldsymbol{Y} - (\boldsymbol{\Phi} \cdot \boldsymbol{\Phi}^{+})^{\top} \cdot \boldsymbol{Y})^{\top} \cdot \mathbf{D}\boldsymbol{\Phi} \cdot \boldsymbol{\Phi}^{+})^{\top} && \text{(double transpose)} \\
J_2 &= ((\boldsymbol{Y} - \boldsymbol{\Phi} \cdot \boldsymbol{\Phi}^{+} \cdot \boldsymbol{Y})^{\top} \cdot \mathbf{D}\boldsymbol{\Phi} \cdot \boldsymbol{\Phi}^{+})^{\top} && ((\boldsymbol{\Phi} \cdot \boldsymbol{\Phi}^{+})^{\top} = \boldsymbol{\Phi} \cdot \boldsymbol{\Phi}^{+}) \\
J_2 &= (\boldsymbol{r}^{\top} \cdot \mathbf{D}\boldsymbol{\Phi} \cdot \boldsymbol{\Phi}^{+})^{\top} && (\boldsymbol{r} = \boldsymbol{Y} - \boldsymbol{\Phi} \cdot \boldsymbol{\Phi}^{+} \cdot \boldsymbol{Y}) \\
J_2 &= (\boldsymbol{\Phi}^{+})^{\top} \cdot (\mathbf{D}\boldsymbol{\Phi})^{\top} \cdot \boldsymbol{r} && \text{(refactor transpose)}
\end{aligned}$$

Now by substituting J_1 and J_2:

$$\boldsymbol{D}\boldsymbol{r} = -J_1 - J_2$$
$$\boldsymbol{D}\boldsymbol{r} = -\mathbf{D}\boldsymbol{\Phi} \cdot \hat{\boldsymbol{c}} + \boldsymbol{\Phi} \cdot (\boldsymbol{\Phi}^{+} \cdot (\mathbf{D}\boldsymbol{\Phi} \cdot \hat{\boldsymbol{c}})) - (\boldsymbol{\Phi}^{+})^{\top} \cdot (\mathbf{D}\boldsymbol{\Phi})^{\top} \cdot \boldsymbol{r}$$

which proves that Eq. (18) is equivalent to Eq. (17).

□

Further inspiration is taken from Golub and Pereyra [31], and O'Leary and Rust [44], who suggest reducing the storage and computational constraints by bookkeeping the non-zero derivatives and skipping storing or calculating the zero derivatives.

The parameter variance can be determined to give a bound on the confidence one has in the estimated parameter values. Mahata and Söderström [45] present a method to estimate the parameter covariance matrix of the union of $\boldsymbol{c}$ and $\boldsymbol{\theta}$.

$$Cov[\boldsymbol{\theta}, \boldsymbol{c}] = \left[\nabla f_m^{\top} \cdot \nabla f_m\right]^{-1} \left[\nabla f_m^{\top} \cdot \Lambda_m \cdot \nabla f_m\right] \left[\nabla f_m^{\top} \cdot \nabla f_m\right]^{-1} \tag{19}$$

In Eq. (19), ∇f_m is the Jacobian matrix of f_m with respect to the parameters $\boldsymbol{\theta}$ and $\boldsymbol{c}$. Furthermore, Λ_m is a Toeplitz matrix built from the autocorrelation sequence $\{\lambda_t\}$ of the residuals r_t. Each diagonal D_i of Λ_m for $-m+1 \leq i \leq m-1$ is constant with value λ_i, where $D_i \neq D_0$ refers to the off-diagonals. The diagonal of the covariance matrix contains the parameter variances.

E. Linear Parameter Estimation

For the identification of aerodynamic coefficient models, linear parameter estimation is used. Linear parameter estimation deals with the identification of parameter values in equations that are linear in the parameters. Note that this does not require the regressors to be linear.

$$\hat{\boldsymbol{Y}} = \boldsymbol{X}\boldsymbol{c} \tag{20}$$

Equation (20) is the general form for this type of model, where $\boldsymbol{X}$ is the regression matrix and $\boldsymbol{c}$ is a vector containing the linear parameters. An estimate for the parameter values can be found using ordinary least squares.

$$\hat{\boldsymbol{c}} = \boldsymbol{X}^{+} \cdot \boldsymbol{Y} \tag{21}$$

The covariance matrix is defined in Eq. (22) and comes from the system identification book by Klein and Morelli [46]. Here Λ_m has the same definition as in Section III.D.

$$Cov[\boldsymbol{c}] = \left[\boldsymbol{X}^\top \cdot \boldsymbol{X}\right]^{-1} \left[\boldsymbol{X}^\top \cdot \Lambda_m \cdot \boldsymbol{X}\right] \left[\boldsymbol{X}^\top \cdot \boldsymbol{X}\right]^{-1} \tag{22}$$

F. Model Validation

As mentioned in Section III.A, 20% of the flight data is reserved for validation. Two main statistics are calculated for the training and validation data sets to judge the performance of the models. First, the mean square error (MSE) is calculated. This value is calculated as follows:

$$MSE = \frac{\sum_{i=1}^{N}(y_i - \hat{y}_i)^2}{N} \tag{23}$$

Secondly, the coefficient of determination or R^2 value can be calculated. This value is an indication of the accuracy of the fit, where 1 indicates a perfect fit. Typically the value varies between 0 and 1, but it is possible to go below one when the measured signal has little variation. The value is calculated as follows:

$$R^2 = 1 - \frac{\sum_{i=1}^{N}(y_i - \hat{y}_i)^2}{\sum_{i=1}^{N}(y_i - \mu_y)^2} \tag{24}$$

IV. Results

A. Evaluation of Separable Nonlinear Least Squares

To judge the effectiveness of SNLS, the model structure defined in Van Ingen et al. [30] is reidentified. In addition, the same data set and training-validation split are used, see Section III.A for details. Note that the cut-off frequencies are still different from the work of Van Ingen et al. [30]. Estimation of flow separation and lift coefficient parameters is performed using the SNLS method. The remaining coefficients are estimated using OLS.

The MSE values on the training and validation data are summarized in Table 7. The MSE values of the lift coefficient are reduced by 36% and 25% on the training and validation data respectively. This consistent reduction shows that the SNLS method finds better solutions within the same optimization problem. Moreover, the computation time is reduced from hours to seconds, which opens the door to more extensive iteration and analysis. All other MSE values of force and moment coefficients are reduced for the training data. However, this consistency is not found in the validation data. This indicates that the model structures might not be optimal, further exploration of different model structures is covered in Section IV.B.

Table 7 Comparison of mean square error values for the model defined by Van Ingen et al. [30] and unidentified using SNLS in this work.

	Training Data			Validation Data		
	Van Ingen	*This work*		*Van Ingen*	*This work*	
Model	**MSE**	**MSE**	**Difference** [%]	**MSE**	**MSE**	**Difference** [%]
C_L	2.74×10^{-3}	1.76×10^{-3}	−36	2.48×10^{-3}	1.86×10^{-3}	−25
C_D	1.33×10^{-4}	1.12×10^{-4}	−15	1.01×10^{-4}	1.00×10^{-4}	−1
C_X	1.65×10^{-4}	1.30×10^{-4}	−21	9.09×10^{-5}	9.28×10^{-5}	2
C_Z	2.70×10^{-3}	1.74×10^{-3}	−36	1.87×10^{-3}	1.87×10^{-3}	−25
C_m	1.17×10^{-4}	1.08×10^{-4}	−8	1.25×10^{-4}	1.25×10^{-4}	0

B. Model Structure Selection

1. Flow Separation Model

As mentioned in Section III.C, a second flow separation state is introduced to model the effects of the stall strips. For each flow separation state, the choice remains between a steady, a quasi-steady, and an unsteady flow separation model. In this section, an analysis is done to explore the different options. For this analysis, SNLS is performed on the lift coefficient. The presumed model incorporates a bias, two Kirchhoff terms, a pitch rate term, and an elevator deflection term. The model looks as follows:

$$C_L = C_{L_0} + C_{L_{\alpha,ss}} \left(\frac{1 + \sqrt{X_{ss}}}{2} \right)^2 \alpha + C_{L_{\alpha,w}} \left(\frac{1 + \sqrt{X_w}}{2} \right)^2 \alpha + C_{L_{q^*}} \frac{q\bar{c}}{V} + C_{L_{\delta_e}} \delta_e \tag{25}$$

Here, X_{ss} is the flow separation state at the stall strip and X_w models the rest of the wing. For both X_{ss} and X_w the steady, quasi-steady and unsteady flow separation models are explored. This leads to nine potential model structures as seen in Table 8. The choice for lift model structure will be explained in Section IV.C.2.

Table 8 Mean square error fit of the lift model using different flow separation dynamics models for the stall strip and wing. The most accurate result is highlighted in green.

		Stall Strip X_{ss}		
		Steady	**Quasi-steady**	**Unsteady**
Wing X_w	**Steady**	3.73×10^{-3}	3.65×10^{-3}	3.55×10^{-3}
	Quasi-steady	3.73×10^{-3}	3.65×10^{-3}	3.56×10^{-3}
	Unsteady	3.70×10^{-3}	3.64×10^{-3}	3.69×10^{-3}

Examining the MSE values of the models in Table 8 reveals several key insights. First, the values are nearly identical when using either a steady or quasi-steady model for X_w. This is because the parameter $\tau_{2,w}$ approaches zero in the quasi-steady models, effectively reducing them to steady models. Furthermore, incorporating unsteady terms enhances the performance of the stall strip flow separation model, where the combination of two unsteady models is an exception. The exception is due to poor convergence, which may be caused by poor observability of the two τ_1

parameters. Consequently, an unsteady model is selected for X_{ss}, while a steady model is chosen for X_w. For the remainder of this paper, the unsteady model for X_{ss} and the steady model for X_w will be utilized as presented in Eqs. (26) and (27). The parameter estimation and associated statistics are presented in Section IV.C.1.

$$\tau_{1,ss}\frac{dX_{ss}}{dt} + X_{ss} = \frac{1}{2} - \frac{1}{2}\tanh\left(a_{1,ss}\left[\alpha - \tau_{2,ss}\dot{\alpha} - \alpha^*_{ss}\right]\right) \tag{26}$$

$$X_w = \frac{1}{2} - \frac{1}{2}\tanh\left(a_{1,w}\left[\alpha - \alpha^*_w\right]\right) \tag{27}$$

2. Lift Model

The lift model created by Van Ingen et al. [30], referred to as **Van Ingen CL**, serves as a baseline for comparison with the new model structures defined in this paper. As mentioned in Section III.C.2, six lift coefficient models are proposed for comparison. **Model CL-I** and **Model CL-II** use one flow separation state, reconstructed using an unsteady flow separation model. **Model CL-III** through **Model CL-VI** use two flow separation states, where X_{ss} uses an unsteady flow separation model and X_w uses a flow steady separation model. The results of the parameter estimation can be summarized using the MSE on the training set. These results are presented in Table 9.

Table 9 Summary of the model exploration for the lift coefficient model. The underlying separation model types are defined as steady (S), quasi-steady (Q) or unsteady (U). Furthermore, the linear parameters are defined. Lastly, the MSE of the lift and normal force coefficient on the training data are also presented. The most accurate result is highlighted in green.

Model			MSE	
Name	**Separation Models (S/Q/U)**	**Linear Parameters**	C_L	C_Z
Van Ingen CL	U	$C_{L_0}, C_{L_\alpha}, C_{L_{\alpha^2}}$	5.2256×10^{-3}	5.0438×10^{-3}
Model CL-I	U	$C_{L_0}, C_{L_\alpha}, C_{L_{\alpha^2}}$	3.8823×10^{-3}	3.7420×10^{-3}
Model CL-II	U	C_{L_0}, C_{L_α}	3.9255×10^{-3}	3.7874×10^{-3}
Model CL-III	U | S	$C_{L_0}, C_{L_{\alpha,ss}}, C_{L_{\alpha,w}}$	3.7919×10^{-3}	3.6565×10^{-3}
Model CL-IV	U | S	$C_{L_0}, C_{L_{\alpha,ss}}, C_{L_{\alpha,w}}, C_{L_{q^*}}$	3.6244×10^{-3}	3.4975×10^{-3}
Model CL-V	U | S	$C_{L_0}, C_{L_{\alpha,ss}}, C_{L_{\alpha,w}}, C_{L_{\delta_e}}$	3.6448×10^{-3}	3.5150×10^{-3}
Model CL-VI	U | S	$C_{L_0}, C_{L_{\alpha,ss}}, C_{L_{\alpha,w}}, C_{L_{q^*}}, C_{L_{\delta_e}}$	3.5534×10^{-3}	3.4278×10^{-3}

As a first step, **Van Ingen CL** and **Model CL-I** are compared. This comparison is made to see the relative performance of the newly developed SNLS method compared to the old nonlinear parameter estimation method. The SNLS method shows a 25.7% reduction in training MSE. Next, **Model CL-II** shows the quadratic spline term is not of significant contribution compared to **Model CL-I** as removing it does not degrade model performance. Therefore, the spline term will be excluded from further analysis. Moving to the two flow separation states, **Model CL-III** shows a 3.4% reduction in training MSE compared to **Model CL-II**.

Another objective of the proposed model structures is the evaluation of pitch rate q and elevator deflection δ_e effects. This is done through model structures **Model CL-IV** through **Model CL-VI**, where **Model CL-IV** and **Model CL-V**

evaluate the separate effects of the pitch rate and elevator deflection respectively, and **Model CL-VI** evaluates the combined effect. The results show that compared to **Model CL-III**, the pitch rate term reduces the training MSE by 4.4% and the elevator deflection term reduces the MSE by 3.9%. Combined the two terms reduce the MSE by 6.3%. The combination of SNLS, two flow separation states, and the inclusion of pitch rate and elevator deflection terms reduce the MSE with a total of 32%. The final model structure looks as follows:

$$C_L = C_{L_0} + C_{L_{\alpha,ss}} \left(\frac{1 + \sqrt{X_{ss}}}{2} \right)^2 \alpha + C_{L_{\alpha,w}} \left(\frac{1 + \sqrt{X_w}}{2} \right)^2 \alpha + C_{L_{q^*}} \frac{q\bar{c}}{V} + C_{L_{\delta_e}} \delta_e \tag{28}$$

3. Drag Model

A total of fourteen models have been tested for the drag model. This is done with five main objectives objectives defined in Section III.C.3. The results of the comparisons are summarized in Table 10. Looking deeper into the results, interesting insights can be found. Starting with the direct comparison of the two nonlinear parameter estimation methods. Using SNLS to estimate **Model CL-I** and then using OLS to estimate **Model CD-I** results in a 12.0% decrease in MSE for the drag coefficient. However, more importantly, the longitudinal force coefficient MSE is reduced by 54.7%. This larger improvement is due to the combined effects of the lift and drag coefficient model improvements.

Moving on to objective number two, the addition of a second flow separation state. Compared to **Model CD-I**, **Model CD-II** further decreases the drag coefficient MSE by 15.6%. This in combination with the improved lift model **Model CL-VI** causes a 34.0% reduction of the longitudinal force coefficient MSE.

The next goal is to review the contribution of the angle of attack as a direct regressor in the model. Before analyzing this, a baseline is set with **Model CD-III**. Then, **Model CD-IV** and **Model CD-V** are estimated to see the improvements of including α and α^2, respectively. Furthermore, **Model CD-VI** shows the effect of including both. It is seen that α^2 has a more significant effect than α, but the best effect is seen when combining the terms. **Model CD-VI** makes a 9.7% reduction in drag coefficient MSE and 8.5% reduction in longitudinal force coefficient MSE, all compared to baseline **Model CD-III**.

A very similar analysis is done for the dependency of drag on lift. **Model CD-III** is used as a baseline. A first observation can be made by looking at **Model CD-X** through **Model CD-XII**. Due to their poor performance, these models are discarded. Looking at **Model CD-VII** through **Model CD-IX** the inclusion of only C_L, only C_L^2, and both are tested. The term C_L^2 outperforms C_L and including both works best. Furthermore, they show that the addition of $(1 - X_{ss})$ and $(1 - X_w)$ have significant impact. **Model CD-IX** reduces the drag coefficient MSE by 10.3% and longitudinal force coefficient by 10.0%, compared to **Model CD-III**. It can thus be said that the lift coefficient addition performs better than the angle of attack addition.

Lastly, the effect of the Kirchhoff flow term is tested and compared to **Model CD-III**. The results again show that

Table 10 Summary of the model exploration for the drag coefficient model. The underlying lift coefficient model is referenced. Furthermore, the linear parameters are defined. Lastly, the MSE of the lift and normal force coefficient on the training data are also presented. The most accurate result is highlighted in green.

Model			MSE	
Name	**Lift Model**	**Linear Parameters**	C_D	C_X
Van Ingen CD	**Van Ingen CL**	$C_{D_0}, C_{D_\alpha}, C_{D_{\delta_e}}, C_{D_{C_T}}, C_{D_X}$	2.3514×10^{-4}	4.1277×10^{-4}
Model CD-I	**Model CL-I**	$C_{D_0}, C_{D_\alpha}, C_{D_{\delta_e}}, C_{D_{C_T}}, C_{D_X}$	2.1027×10^{-4}	1.9151×10^{-4}
Model CD-II	**Model CL-VI**	$C_{D_0}, C_{D_\alpha}, C_{D_{\delta_e}}, C_{D_{C_T}}, C_{D_{X,ss}}, C_{D_{X,w}}$	1.7545×10^{-4}	1.2495×10^{-4}
Model CD-III	**Model CL-VI**	$C_{D_0}, C_{D_{C_T}}, C_{D_{q^*}}, C_{D_{\delta_e}}, C_{D_{X,ss}}, C_{D_{X,w}}$	1.7890×10^{-4}	1.2814×10^{-4}
Model CD-IV	**Model CL-VI**	C_{D_0}, $C_{D_{C_T}}$, $C_{D_{q^*}}$, $C_{D_{\delta_e}}$, $C_{D_{X,ss}}$, $C_{D_{X,w}}$, C_{D_α}	1.7225×10^{-4}	1.2372×10^{-4}
Model CD-V	**Model CL-VI**	C_{D_0}, $C_{D_{C_T}}$, $C_{D_{q^*}}$, $C_{D_{\delta_e}}$, $C_{D_{X,ss}}$, $C_{D_{X,w}}$, $C_{D_{\alpha^2}}$	1.6585×10^{-4}	1.1980×10^{-4}
Model CD-VI	**Model CL-VI**	C_{D_0}, $C_{D_{C_T}}$, $C_{D_{q^*}}$, $C_{D_{\delta_e}}$, $C_{D_{X,ss}}$, $C_{D_{X,w}}$, $C_{D_\alpha}, C_{D_{\alpha^2}}$	1.6162×10^{-4}	1.1749×10^{-4}
Model CD-VII	**Model CL-VI**	C_{D_0}, $C_{D_{C_T}}$, $C_{D_{q^*}}$, $C_{D_{\delta_e}}$, $C_{D_{X,ss}}$, $C_{D_{X,w}}$, $C_{D_{C_L}}$	1.7186×10^{-4}	1.2327×10^{-4}
Model CD-VIII	**Model CL-VI**	C_{D_0}, $C_{D_{C_T}}$, $C_{D_{q^*}}$, $C_{D_{\delta_e}}$, $C_{D_{X,ss}}$, $C_{D_{X,w}}$, $C_{D_{C_L^2}}$	1.6683×10^{-4}	1.1981×10^{-4}
Model CD-IX	**Model CL-VI**	C_{D_0}, $C_{D_{C_T}}$, $C_{D_{q^*}}$, $C_{D_{\delta_e}}$, $C_{D_{X,ss}}$, $C_{D_{X,w}}$, $C_{D_{C_L}}, C_{D_{C_L^2}}$	1.6077×10^{-4}	1.1572×10^{-4}
Model CD-X	**Model CL-VI**	$C_{D_0}, C_{D_{C_T}}, C_{D_{q^*}}, C_{D_{\delta_e}}, C_{D_{C_L}}$	4.7955×10^{-4}	4.0464×10^{-4}
Model CD-XI	**Model CL-VI**	$C_{D_0}, C_{D_{C_T}}, C_{D_{q^*}}, C_{D_{\delta_e}}, C_{D_{C_L^2}}$	4.5693×10^{-4}	3.8668×10^{-4}
Model CD-XII	**Model CL-VI**	$C_{D_0}, C_{D_{C_T}}, C_{D_{q^*}}, C_{D_{\delta_e}}, C_{D_{C_L}}, C_{D_{C_L^2}}$	4.0461×10^{-4}	3.4206×10^{-4}
Model CD-XIII	**Model CL-VI**	$C_{D_0}, C_{D_{C_T}}, C_{D_{q^*}}, C_{D_{\delta_e}}, C_{D_{K_D,ss}}, C_{D_{K_D,w}}$	2.6119×10^{-4}	2.0720×10^{-4}
Model CD-XIV	**Model CL-VI**	C_{D_0}, $C_{D_{C_T}}$, $C_{D_{q^*}}$, $C_{D_{\delta_e}}$, $C_{D_{X,ss}}$, $C_{D_{X,w}}$, $C_{D_{K_D,ss}}, C_{D_{K_D,w}}$	1.7722×10^{-4}	1.2555×10^{-4}

the inclusion of $(1 - X_{ss})$ and $(1 - X_w)$ is necessary. The best performing version, **Model CD-XIV**, shows a 1.1% reduction in drag coefficient MSE and 2.1% reduction in longitudinal force coefficient MSE. This term performs worse than previous terms and is hence discarded.

From the previous analysis, **Model CD-IX** is selected for further refinement. Firstly, the pitch rate term is removed as its t-test null hypothesis was accepted. Looking further, the correlations between $C_{D_{C_L}}$ and $C_{D_{C_L^2}}$ as well as $C_{D_{C_L}}$ and C_{D_0} are between 0.8 and 0.9. Considering the small difference in performance between **Model CD-IX** and **Model CD-VIII**, the $C_{D_{C_L}}$ term is removed. This leads to the following model:

$$C_D = C_{D_0} + C_{D_{C_T}} C_T + C_{D_{\delta_e}} \delta_e + C_{D_{C_L^2}} C_L^2 + C_{D_{X,ss}} (1 - X_{ss}) + C_{D_{X,w}} (1 - X_w) \tag{29}$$

4. Pitch Moment Model

As mentioned in Section III.C.4, 59 new model structures are selected to be evaluated for the pitch moment model. Due to their large quantity, individual mentions are omitted. However, global observations are discussed, and a

comprehensive overview of all model fitting results is provided in Table 20 in Appendix B. The first objective was to estimate **Model Cm-I**, building on the results of **Model CL-I**. It decreases the MSE on the pitch moment coefficient by 2.3%.

Moving on to the models proposed by Leishman and Beddoes [35], and Singh and Jategaonkar [16]. First, it is observed that the inclusion of K_2^m does not provide significant improvements. Although marginal improvements are found, it is chosen to neglect these terms because of their diminishing returns and risk of overfitting. Furthermore, the inclusion of K_0 must be paired with K_1 or $(1 - X)$ to provide good results.

The model term proposed by Goman and Khrabrov [34], and Singh and Jategaonkar [16], shows poor performance individually. Paired with K_0 and $(1 - X)$ it provides a decent improvement. However, there is no clear physical underlying meaning for this. To improve the interpretability of the results, this term is omitted. Lastly, the inclusion of $X\delta_e$ to model a reduction in the elevator effectiveness at high angles of attack shows consistent improvements in the model. For this reason, it is chosen to keep it in the model.

Based on the previous sections, **Model Cm-XXXIII** is chosen. This model includes K_0 and K_1 as well as $X\delta_e$. Although the addition of $(1 - X)$ could improve the model slightly, it is excluded to limit the complexity of the model. **Model Cm-XXXIII** serves as a start for refinement. As a first observation, the correlation between $C_{m_{\delta_e}}$ and $C_{m_{X_w \delta_e}}$ is found to be above 0.9. Therefore, it is decided to remove the latter. This does not have significant repercussions in terms of model performance. This results in the following model:

$$\begin{aligned} C_m = {} & C_{m_0} + C_{m_{C_T}} C_T + C_{m_{q^*}} \frac{q\bar{c}}{V} + C_{m_{\delta_e}} \delta_e + C_{m_{c.g.}} \frac{x_{c.g.}}{\bar{c}} C_L \\ & + C_{m_{K_0}} C_L + C_{m_{K_{1,ss}}} (1 - X_{ss}) C_L + C_{m_{K_{1,w}}} (1 - X_w) C_L + C_{m_{X_{ss}\delta_e}} X_{ss} \delta_e \end{aligned} \tag{30}$$

Finally, by grouping the terms relating to C_L, a model for the distance between the center of gravity and the center of pressure can be obtained, this is referred to as $l_{c.p.}$. Furthermore, terms relating to the elevator deflection δ_e can be grouped to create a model of the effectivity of the elevator $C^*_{m_{\delta_e}}$. This results in the following model:

$$C_m = C_{m_0} + C_{m_{C_T}} C_T + C_{m_{q^*}} \frac{q\bar{c}}{V} - l_{c.p.} C_L + C^*_{m_{\delta_e}} \delta_e \tag{31}$$

$$l_{c.p.} = \frac{x_{c.p.} - x_{c.g.}}{\bar{c}} = -C_{m_{K_0}} - C_{m_{K_{1,ss}}} (1 - X_{ss}) - C_{m_{K_{1,w}}} (1 - X_w) - C_{m_{c.g.}} \frac{x_{c.g}}{\bar{c}} \tag{32}$$

$$C^*_{m_{\delta_e}} = C_{m_{\delta_e}} + C_{m_{X_{ss}\delta_e}} X_{ss} \tag{33}$$

C. Stall Model

The final model structure, as derived from the analyses described in Section IV.B, can be obtained as:

$$C_L = C_{L_0} + C_{L_{\alpha,ss}} \left(\frac{1 + \sqrt{X_{ss}}}{2} \right)^2 \alpha + C_{L_{\alpha,w}} \left(\frac{1 + \sqrt{X_w}}{2} \right)^2 \alpha + C_{L_{q^*}} \frac{q\bar{c}}{V} + C_{L_{\delta_e}} \delta_e \tag{34}$$

$$C_D = C_{D_0} + C_{D_{C_T}} C_T + C_{D_{\delta_e}} \delta_e + C_{D_{C_L^2}} C_L^2 + C_{D_{X,ss}} (1 - X_{ss}) + C_{D_{X,w}} (1 - X_w) \tag{35}$$

$$C_m = C_{m_0} + C_{m_{C_T}} C_T + C_{m_{q^*}} \frac{q\bar{c}}{V} - l_{c.p.} C_L + C^*_{m_{\delta_e}} \delta_e \tag{36}$$

The models for the aerodynamic force and moment coefficients are supplemented with a model for the position of the center of pressure and control effectiveness of the elevator:

$$l_{c.p.} = -C_{m_{K_0}} - C_{m_{K_{1,ss}}} (1 - X_{ss}) - C_{m_{K_{1,w}}} (1 - X_w) - C_{m_{c.g.}} \frac{x_{c.g}}{\bar{c}} \tag{37}$$

$$C^*_{m_{\delta_e}} = C_{m_{\delta_e}} + C_{m_{X_{ss}\,\delta_e}} X_{ss} \tag{38}$$

Lastly, the stall is modeled using two flow separation states. One state will model the effect of stall strips installed on the wing, and another will model the rest of the wing. The governing equations are obtained as:

$$\tau_{1,ss} \frac{dX_{ss}}{dt} + X_{ss} = \frac{1}{2} - \frac{1}{2} \tanh \left(a_{1,ss} \left[\alpha - \tau_{2,ss} \dot{\alpha} - \alpha^*_{ss} \right] \right) \tag{39}$$

$$X_w = \frac{1}{2} - \frac{1}{2} \tanh \left(a_{1,w} \left[\alpha - \alpha^*_w \right] \right) \tag{40}$$

1. Flow Separation Models

Using the SNLS method, the models for the lift coefficient and flow separation states defined in Eqs. (34), (39) and (40) can be estimated simultaneously. The results of this system identification task can be found in Tables 11 and 12. The results in Table 11 show an acceptable parameter standard deviation. It also shows that all null hypotheses for the t-test are rejected. Furthermore, all parameter correlations in Table 12 are below 0.9. The correlation between $\tau_{1,ss}$ and $\tau_{2,ss}$ is very low, indicating that the new flight maneuvers mentioned in Section III.A are effective. The highest correlation is found for C_{L_0} and $C_{L_{\alpha,ss}}$. This correlation was already highlighted by Van Ingen et al. [30] and is likely caused by parts of the data having insufficient variation in the angle of attack. However, removing either term significantly reduces the accuracy of the model, thus both are retained.

Looking at the static flow separation parameters of the stall strip and wing, a few observations can be made. Starting with the stall strip angle of attack α^*_{ss}. This is found to be at 11.2° and is in line with the start of buffet vibrations. Furthermore, the abruptness of the stall modeled by $a_{1,ss}$ is high. This corresponds well with the behavior of a stall strip, which causes flow separation at the leading edge. A high abruptness is seen here as a crude method for modeling a

Table 11 Parameter estimates and statistics for the final lift coefficient model. For the t-test $\circ$ indicates that the null hypothesis is accepted and $*$ that the null hypothesis is rejected.

		Results		t-test	
Parameter	**Unit**	$\hat{\theta}$	σ_θ	p	h
$\tau_{1,ss}$	s	**0.4191**	0.0722	0.0000	*
$\tau_{2,ss}$	s	**0.3391**	0.0346	0.0000	*
$a_{1,ss}$	-	**70.2846**	11.2205	0.0000	*
α^*_{ss}	rad	**0.1956**	0.0017	0.0000	*
$a_{1,w}$	-	**13.9276**	1.4462	0.0000	*
α^*_w	rad	**0.3267**	0.0056	0.0000	*
C_{L_0}	-	**0.2318**	0.0116	0.0000	*
$C_{L_{K_{\alpha,ss}}}$	-	**1.3851**	0.1061	0.0000	*
$C_{L_{K_{\alpha,w}}}$	-	**2.5961**	0.0536	0.0000	*
$C_{L_{q^*}}$	-	**8.0747**	1.3881	0.0000	*
$C_{L_{\delta_e}}$	-	**−0.3403**	0.0681	0.0000	*

Table 12 Parameter correlation matrix for the final lift coefficient model. High correlations are highlighted red.

	$\tau_{1,ss}$	$\tau_{2,ss}$	$a_{1,ss}$	α^*_{ss}	$a_{1,w}$	α^*_w	C_{L_0}	$C_{L_{K_{\alpha,ss}}}$	$C_{L_{K_{\alpha,w}}}$	$C_{L_{q^*}}$	$C_{L_{\delta_e}}$
$\tau_{1,ss}$	1.00	0.06	0.21	0.10	0.15	0.03	0.16	-0.35	0.33	0.06	-0.08
$\tau_{2,ss}$	0.06	1.00	-0.07	-0.35	0.09	0.36	0.09	-0.27	0.40	0.51	0.16
$a_{1,ss}$	0.21	-0.07	1.00	0.36	-0.08	0.03	0.07	0.04	-0.07	0.05	0.13
α^*_{ss}	0.10	-0.35	0.36	1.00	-0.04	0.04	0.17	-0.10	-0.26	-0.03	-0.21
$a_{1,w}$	0.15	0.09	-0.08	-0.04	1.00	0.30	0.00	-0.05	0.14	0.29	0.10
α^*_w	0.03	0.36	0.03	0.04	0.30	1.00	0.07	-0.16	0.28	0.46	0.21
C_{L_0}	0.16	0.09	0.07	0.17	0.00	0.07	1.00	-0.87	-0.27	0.58	-0.12
$C_{L_{K_{\alpha,ss}}}$	-0.35	-0.27	0.04	-0.10	-0.05	-0.16	-0.87	1.00	-0.11	-0.61	0.23
$C_{L_{K_{\alpha,w}}}$	0.33	0.40	-0.07	-0.26	0.14	0.28	-0.27	-0.11	1.00	0.25	0.49
$C_{L_{q^*}}$	0.06	0.51	0.05	-0.03	0.29	0.46	0.58	-0.61	0.25	1.00	0.30
$C_{L_{\delta_e}}$	-0.08	0.16	0.13	-0.21	0.10	0.21	-0.12	0.23	0.49	0.30	1.00

leading-edge stall. Moving on to $a_{1,w}$, a much more subtle stall is estimated for the rest of the wing. This is in line with the expected trailing-edge stall. Furthermore, α^*_w is estimated to be 18.7°. This corresponds well with the wind tunnel results for NACA23012, which indicated that the stall angle of attack must be between 15° and 20°.

Using the four static flow separation parameters discussed before, the static flow separation curves can be plotted. These are presented in the left plots of Fig. 6. Three main stages in the flow separation behavior can be defined: no flow separation, stall strip flow separation, and full flow separation. No flow separation is the expected stage during normal flight, this is defined in Fig. 6 as stage 1. As can be seen in the top right plot, the flow separation line is located at the trailing edge of the wing. Moving on to stage 2, stall strip separation, corresponds to the middle right plot. It can be seen that the green flow separation line has moved to the leading edge which means full flow separation at the stall strips. Lastly, stage 3 refers to full flow separation and is shown in the bottom right plot. At this stage, the rest of the wing follows the stall strips and the flow separates.

The unsteady flow separation parameters of the stall strip were determined at $\tau_{1,ss}$=0.4191 s and $\tau_{2,ss}$=0.3391 s.

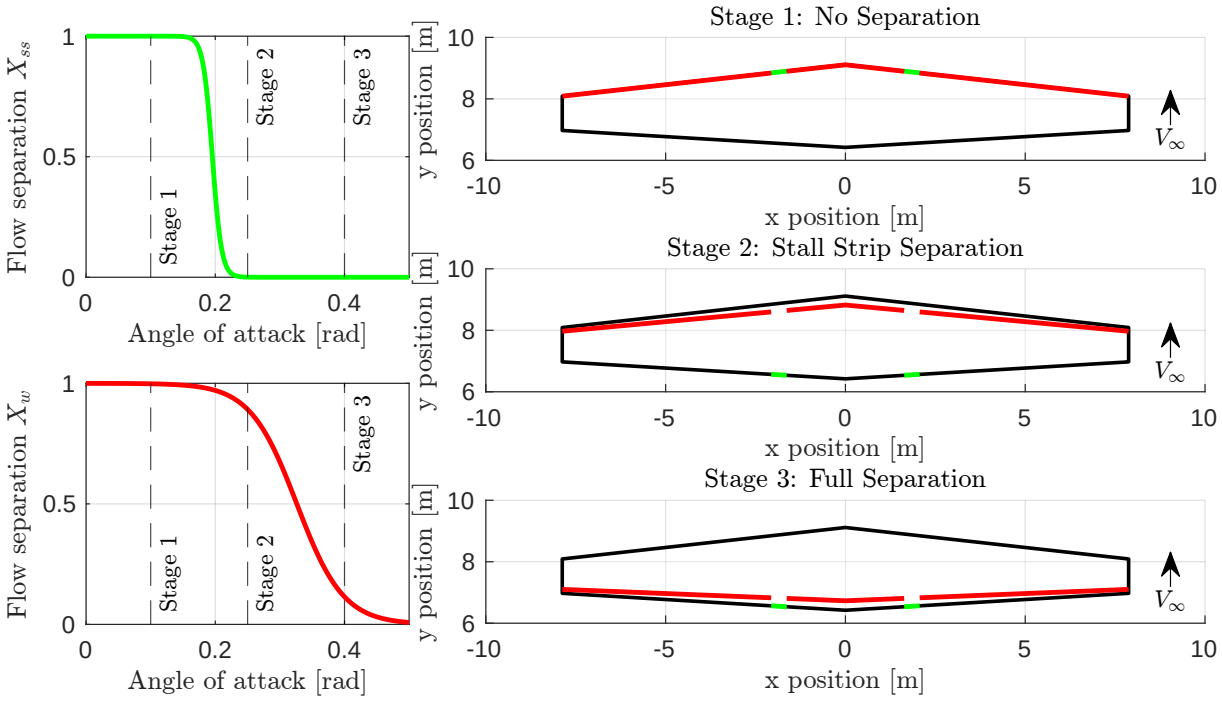

Fig. 6 Visualization of the stages of flow separation on the wing. Flow separation state of the stall strip in the top left plot. Flow separation state of the rest of the wing in the bottom left plot. The three right plots show the three stages of flow separation on a top view of the wing and reference the vertical lines in the left plots.

Using the average airspeed of the training set V=87 m/s and chord length, the non-dimensional time constants can be determined. These are $\tau^*_{1,ss}$=18.14 and $\tau^*_{2,ss}$=14.67. The value for $\tau_{1,ss}$ corresponds well with literature. However, $\tau_{2,ss}$ is observed to be relatively high [15].

2. Lift Model

The lift coefficient model parameters have been identified with SNLS in Section IV.C.1. A review of the parameter values in Table 11 is performed here. The zero angle of attack lift coefficient C_{L_0} is estimated at 0.2318. It is expected for this value to be above zero due to an angle of incidence of the wing and a camber in the airfoil profile. The lift curve slope in the linear part of the angle of attack range is 3.98 and found by combining $C_{L_{\alpha,ss}}$ and $C_{L_{\alpha,w}}$. The response of the lift to a pitch, captured by $C_{L_{q^*}}$, is positive, as expected. Lastly, the response of the lift to an elevator deflection is estimated to be negative. The low lift curve slope and negative response of lift to elevator deflection could be explained by a high correlation between the angle of attack and elevator deflection, which is estimated at -0.8 for the training set.

Using C_{L_0}, $C_{L_{\alpha,ss}}$, $C_{L_{\alpha,w}}$ and the steady flow separation parameters, the static lift curve can be constructed. Figure 7 shows the measured values as data points and the static lift curves of Van Ingen [23] and this work. It can be seen that the measured values show significant spread, which can be attributed to neglected elevator deflection effects through $C_{L_{\delta_e}}$ and unsteady effects modeled by $\tau_{1,ss}$, $\tau_{2,ss}$ and $C_{L_{q^*}}$. Beyond that, it can be seen that both models are in the

middle of the measurements in the low angle of attack regions. However, the previous model starts to diverge at high angles of attack due to the quadratic spline term in the work of Van Ingen [23]. This divergence already starts around 0.3 radians. On the other hand, the old model closer approximates the data at low angles of attack.

3. Drag Model

For the refined C_D model defined in Eq. (35), referred to as **Model CD-IXr**, the results of the parameter estimation are presented in Tables 13 and 14. It can be seen in Table 13 that all t-test null hypotheses are rejected, indicating that each parameter is significantly different from zero. Furthermore, it can be seen in Table 14 that all correlations are below 0.8.

Looking at the values of the coefficients, C_{D_0} is estimated at 0.0165, indicating there is some drag, even when all other contributions are zero. The coefficient $C_{D_{C_T}}$ is estimated at 0.3917, which corresponds well with previous results found by Van Ingen et al. [30]. The coefficient for the elevator deflection $C_{D_{\delta_e}}$ is found to be negative. This is likely because the deflection is on average negative, which makes the contribution of the elevator to the drag positive. As expected, the lift causes added lift-induced drag, thus the coefficient $C_{D_{C_L^2}}$ is positive. The coefficients $C_{D_{X_{ss}}}$ and $C_{D_{X_w}}$ indicate that as the flow separates a further increase in drag is observed.

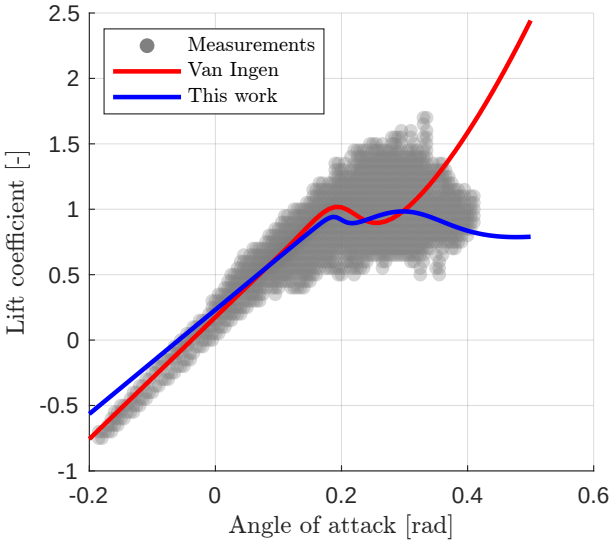

Fig. 7 Static lift curve for Van Ingen CL and Model CL-VI plotted over the measured lift coefficient values

Table 13 Estimated coefficients for the Drag coefficient model. For the t-test $\circ$ indicates that the null hypothesis is accepted and $*$ that the null hypothesis is rejected.

		Results		t-test	
Parameter	**Unit**	$\hat{\theta}$	$\sigma_{\hat{\theta}}$	p	h
C_{D_0}	-	**0.0165**	0.0020	0.0000	*
$C_{D_{C_T}}$	-	**0.3917**	0.0135	0.0000	*
$C_{D_{\delta_e}}$	-	**−0.1894**	0.0131	0.0000	*
$C_{D_{C_L^2}}$	-	**0.0258**	0.0035	0.0000	*
$C_{D_{X_{ss}}}$	-	**0.0555**	0.0017	0.0000	*
$C_{D_{X_w}}$	-	**0.2062**	0.0064	0.0000	*

Table 14 Parameter correlation matrix for the Drag coefficient model.

	C_{D_0}	$C_{D_{C_T}}$	$C_{D_{\delta_e}}$	$C_{D_{C_L^2}}$	$C_{D_{X_{ss}}}$	$C_{D_{X_w}}$
C_{D_0}	1.00	-0.74	-0.23	-0.76	0.20	0.40
$C_{D_{C_T}}$	-0.74	1.00	-0.05	0.23	0.14	-0.38
$C_{D_{\delta_e}}$	-0.23	-0.05	1.00	0.73	-0.25	-0.04
$C_{D_{C_L^2}}$	-0.76	0.23	0.73	1.00	-0.40	-0.25
$C_{D_{X_{ss}}}$	0.20	0.14	-0.25	-0.40	1.00	-0.52
$C_{D_{X_w}}$	0.40	-0.38	-0.04	-0.25	-0.52	1.00

Using the estimated model, the static drag polar may be constructed. The static drag polar is presented in Fig. 8. The polar is complemented by the measurements corrected for the effects of the thrust coefficient and elevator deflection. Furthermore, the model **Van Ingen CD** from Van Ingen et al. [30] is added for comparison. It can be seen that the new model better matches the high and low angle of attack regions. Furthermore, the C_L^2 term ensures that drag remains positive for negative angles of attack.

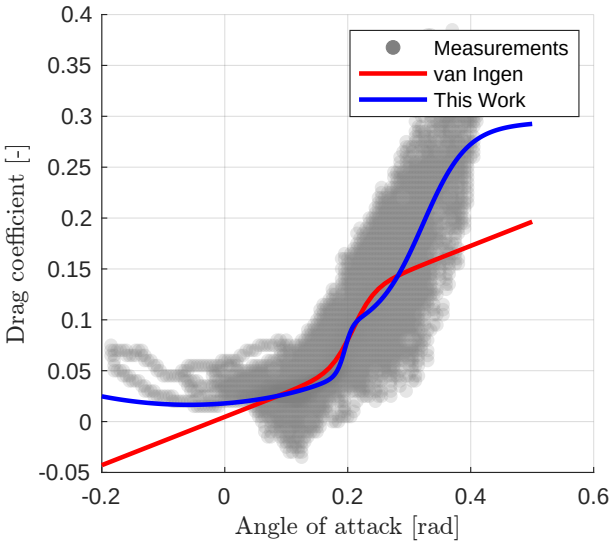

Fig. 8 Static drag polar for Van Ingen CL and Model CD-IXr plotted over the adjusted drag coefficient measurements

4. Pitch Moment Model

The results of the model identification for the pitch moment model in Eq. (36), referred to as **Model Cm-XXXIIIr**, are presented in Tables 15 and 16. Immediately, the high correlation between $C_{m_{cg}}$ and $C_{m_{K_0}}$ in Table 16 stands out. This makes sense as the center of gravity is relatively constant. However, due to the difference it makes for the accuracy of the model the term is retained. Beyond that, all terms were found to be significant by the t-test, and parameter correlations are below 0.8.

Table 15 Estimated coefficients for the Pitch moment coefficient model. For the t-test $\circ$ indicates that the null hypothesis is accepted and $*$ that the null hypothesis is rejected.

		Results		t-test	
Parameter	**Unit**	$\hat{\theta}$	$\sigma_{\hat{\theta}}$	p	h
C_{m_0}	-	0.0659	0.0026	0.0000	*
$C_{m_{C_T}}$	-	0.0794	0.0089	0.0000	*
$C_{m_{q^*}}$	-	−1.7502	0.2675	0.0000	*
$C_{m_{\delta e}}$	-	−0.7431	0.0134	0.0000	*
$C_{m_{c.g.}}$	-	−0.9616	0.1305	0.0000	*
$C_{m_{K_0}}$	-	3.2316	0.4594	0.0000	*
$C_{m_{K_{1,ss}}}$	-	−0.0517	0.0033	0.0000	*
$C_{m_{K_{1,w}}}$	-	−0.0681	0.0053	0.0000	*
$C_{m_{X_1\delta e}}$	-	−0.2576	0.0224	0.0000	*

The model for the center of pressure is presented in Fig. 9. The center of pressure is measured from a datum defined 15 inches in front of the aircraft [33]. It can be seen that for low angles of attack, the center of pressure is constant and it shifts backward as the aircraft stalls. The stall angles of attack for the stall strip and the rest of the wing are highlighted in the figure. The shift back is expected and relates to the relative contribution of the horizontal tail becoming larger.

Table 16 Parameter correlation matrix for the Pitch moment coefficient model. High correlations are highlighted red.

	C_{m_0}	$C_{m_{C_T}}$	$C_{m_{q^*}}$	$C_{m_{\delta_e}}$	$C_{m_{c.g.}}$	$C_{m_{K_0}}$	$C_{m_{K_{1,ss}}}$	$C_{m_{K_{1,w}}}$	$C_{m_{X_1\delta_e}}$
C_{m_0}	1.00	-0.41	0.54	0.07	-0.07	0.06	0.51	0.20	-0.38
$C_{m_{C_T}}$	-0.41	1.00	0.08	-0.07	-0.45	0.45	0.03	-0.30	0.08
$C_{m_{q^*}}$	0.54	0.08	1.00	0.28	-0.40	0.39	0.57	-0.23	-0.21
$C_{m_{\delta_e}}$	0.07	-0.07	0.28	1.00	-0.08	0.08	0.67	0.04	-0.68
$C_{m_{c.g.}}$	-0.07	-0.45	-0.40	-0.08	1.00	-1.00	-0.27	0.13	0.11
$C_{m_{K_0}}$	0.06	0.45	0.39	0.08	-1.00	1.00	0.26	-0.13	-0.11
$C_{m_{K_{1,ss}}}$	0.51	0.03	0.57	0.67	-0.27	0.26	1.00	-0.15	-0.78
$C_{m_{K_{1,w}}}$	0.20	-0.30	-0.23	0.04	0.13	-0.13	-0.15	1.00	-0.27
$C_{m_{X_1\delta_e}}$	-0.38	0.08	-0.21	-0.68	0.11	-0.11	-0.78	-0.27	1.00

The center of gravity envelope lies between 276 and 286 inches[†], which is ahead of the center of pressure at all times. This means that the configuration is stable; that this comes back from the identification results is an important marker for the reliability of the results.

Moving to the effective elevator control effectiveness $C^*_{m_{\delta_e}}$. It has long been known that the stall would adversely affect this [30]. The results in this work, as seen in Fig. 10, show the same. The initial control effectiveness is close to that estimated by Van Ingen et al. [30], however, the degradation is less. In previous work, the degradation was forced to be 50%, due to the model structure. In this work, the identification has more freedom and therefore is seen as a more reliable estimate.

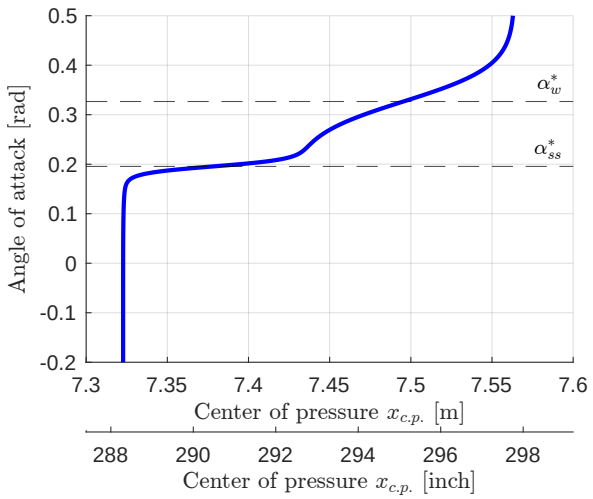

Fig. 9 Variation of the center of pressure $x_{c.p}$ with respect to a datum in front of the aircraft for increasing angle of attack.

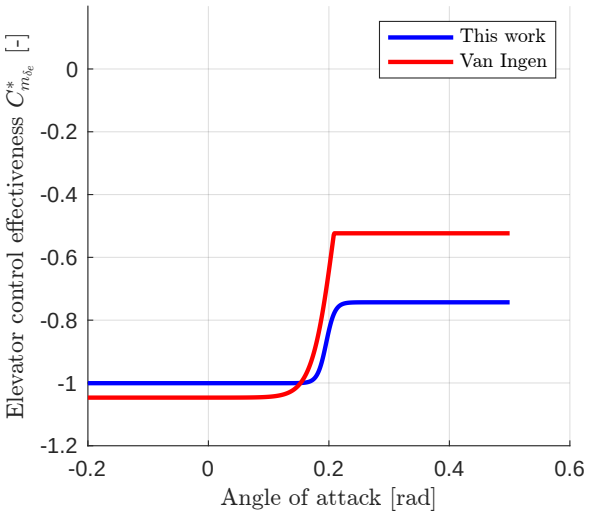

Fig. 10 Variation of the elevator control effectiveness for increasing angle of attack. Compared against Van Ingen et al. [30]

[†]Information received from the TU Delft's research aircraft technicians

Lastly, the static pitch moment behavior can be plotted in Fig. 11. To do this, unsteady effects from the flow separation states are neglected. Furthermore, the measurements are corrected for elevator and thrust coefficient effects. The static pitch moment is compared to that obtained by Van Ingen et al. [30]. Interestingly, the two models behave very similarly in the low angle of attack region. However, for high angles of attack the new model levels off, as opposed to the previous model. This is expected as the lift, causing the moment, levels off as well. At first, this is offset by the shift of the center of pressure, but as that stabilizes the pitch moment settles too.

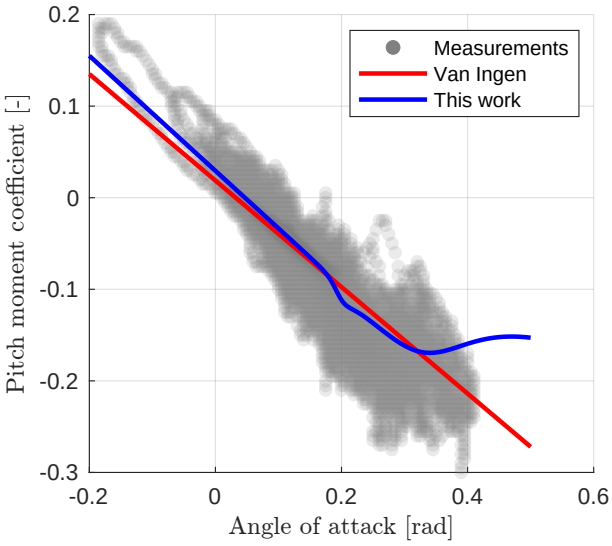

Fig. 11 Static pitch moment for Van Ingen Cm and Model Cm-XXXIIIr plotted over the adjusted pitch moment measurements.

D. Model Validation

As mentioned in Section III.A, 20% of the data is saved to be used for validation. This data is used to show that the identified model can generalize. A comparison of the MSE values on the training and validation data sets is summarized in Table 17. This table recaps the reductions mentioned in previous sections. Furthermore, the reductions for the validation set are presented. Improvements for the validation set are smaller, but significant nonetheless. The consistency of the improvements builds confidence in the validity of the model.

Table 17 Comparison of mean square error values for the model defined in this work and that by Van Ingen et al. [30]

	Training Data			**Validation Data**		
	Van Ingen	*This work*		*Van Ingen*	*This work*	
Model	**MSE**	**MSE**	**Difference** [%]	**MSE**	**MSE**	**Difference** [%]
C_L	5.23×10^{-3}	3.55×10^{-3}	−32	4.09×10^{-3}	3.38×10^{-3}	−17
C_D	2.35×10^{-4}	1.68×10^{-4}	−29	1.90×10^{-4}	1.75×10^{-4}	−8
C_X	4.13×10^{-4}	1.20×10^{-4}	−71	1.98×10^{-4}	1.53×10^{-4}	−23
C_Z	5.04×10^{-3}	3.60×10^{-3}	−29	4.07×10^{-3}	3.38×10^{-3}	−17
C_m	1.96×10^{-4}	1.43×10^{-4}	−27	2.52×10^{-4}	1.86×10^{-4}	−26

The R^2 value can be calculated for each maneuver in the training and validation data sets. Moreover, the R^2 values can be obtained for all models. The resulting values are summarized in Fig. 12, where Fig. 12a shows the training data and Fig. 12b shows the validation data. The plots show an improvement in the consistency of the model obtained in this work. This is evident from the increases in mean values, first quartile values, lower whisker values, and outlier values.

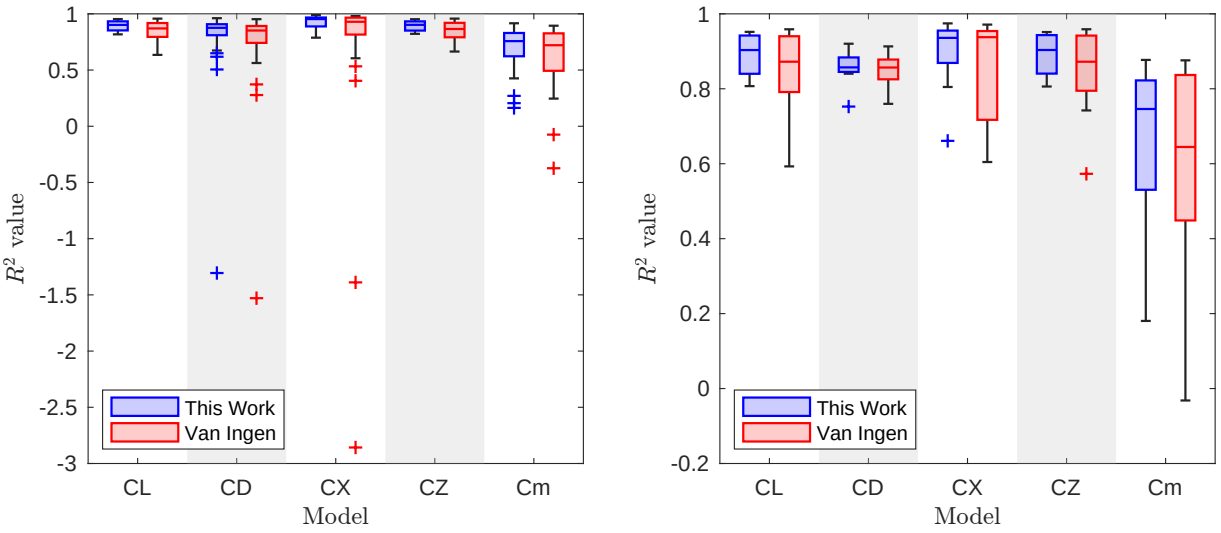

(a) Training data **(b) Validation data**

Fig. 12 Boxplots of the R^2 values of each model. R^2 values are calculated for each maneuver.

Figure 13 shows a comparison of the previous and new models for three selected flight maneuvers of the validation set. These were chosen based on the average R^2 value for the different submodels. The model performed worst for maneuver 46, average performance was found for maneuver 16, and the best performance on maneuver 7. The plots show that, in general, the prediction made by the new model is closer to the measured value.

V. Discussion

A. Implications of Separable Nonlinear Least Squares

SNLS is introduced in this paper as an alternative nonlinear parameter estimation technique. Its goal is to overcome three main limitations in prior methods: long runtime, lack of a parameter correlation metric, and suboptimal linear parameter results. The first limitation has been largely eliminated, with runtime reduced from hours to seconds. The second limitation was removed with the introduction of the covariance matrix in Eq. (19). The correlation metric can be derived from the covariance matrix. The third limitation was previously solved by running OLS after the nonlinear parameter estimation. However, this gave inconsistent results between nonlinear and linear parameter estimation methods. SNLS embeds OLS into it for the linear parameters, implying that the parameter estimates are the best linear unbiased estimators of the true parameter values.

The use of SNLS has enabled rapid iteration of model structures, which can be expanded even more in the future. For the separation states and lift coefficient, 15 different nonlinear parameter estimations have been performed. In the past, this was infeasible. The low runtime enables more comprehensive studies to be performed in the future. On top of the runtime improvement, the SNLS method also converges to better parameter values. In Section IV.A, the model of

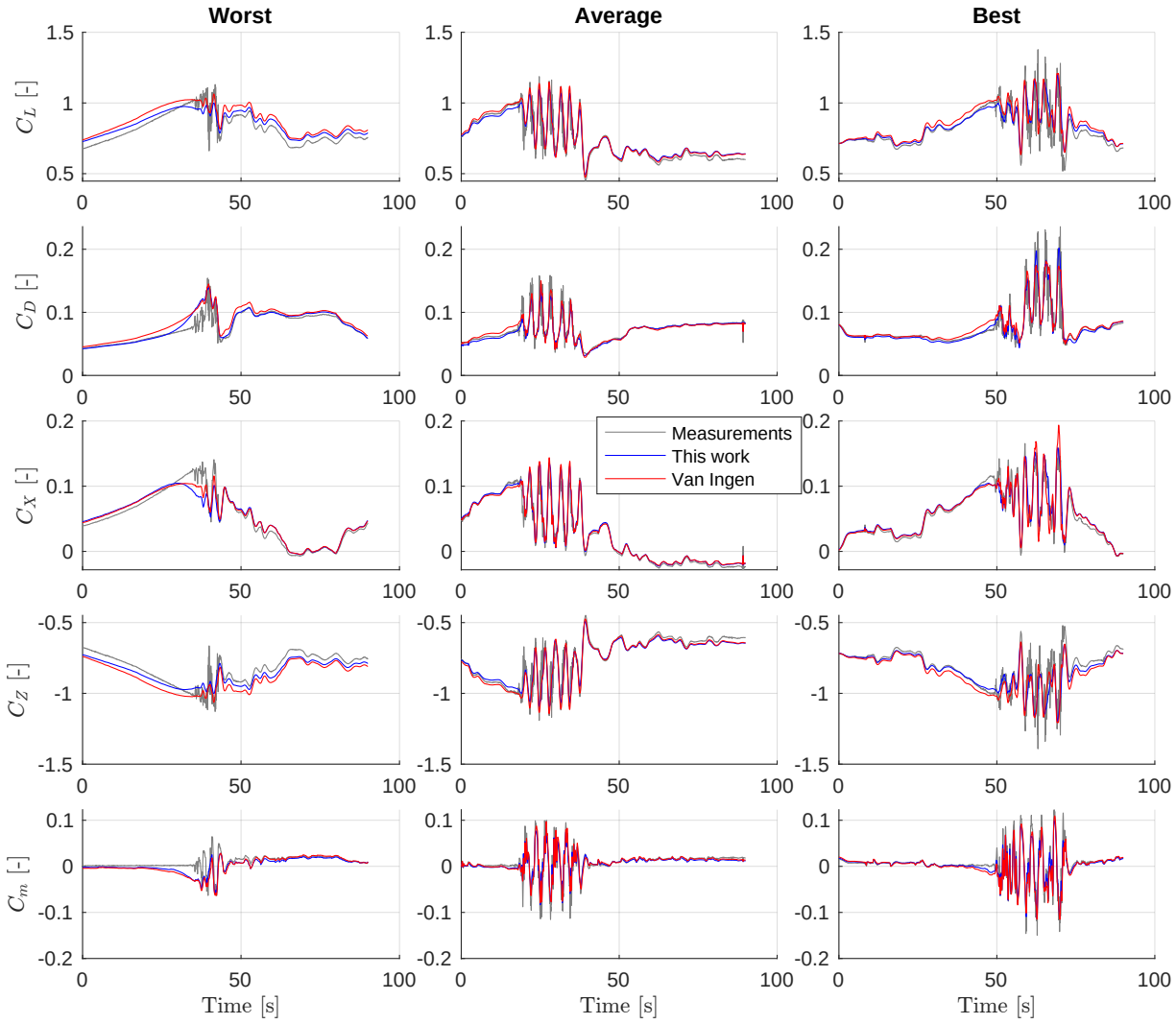

Fig. 13 Performance of the new longitudinal stall model compared with Van Ingen et al. [30] for selected maneuvers. Left shows maneuver 46, the middle shows maneuver 16, and the right shows maneuver 7.

Van Ingen et al. [30] was re-identified and lower MSE values were found on the same maneuvers. The same was found when retaining the same model structure on the new data set created for this paper. Moreover, the results prove more consistent, showing higher averages and smaller spreads in R^2 values.

The potential of the SNLS method is clear, however, work remains in extending the method to lateral flight dynamics. Additionally, the method should be integrated with better model structure selection methods, such as genetic algorithms or exhaustive methods. The use of SNLS has also opened up the option to work with larger data sets. Future work should use this to create composite data sets with stall and non-stall data. Integrating stall models with nominal models has been a longstanding challenge and this is seen as a potential avenue for closing that gap.

B. Stall Model

A new longitudinal stall model for the Cessna Citation II has been presented in this paper. The new model reduces the training MSE by around 30% for the lift, drag, and pitch moment coefficients. Furthermore, the validation MSE is decreased by around 20%.

The model has been extended with a second flow separation state. The second state is hypothesized to correspond to the stall strip. However, this cannot be confirmed without specific tests to visualize the flow around the wing. To this effect, it is suggested for subsequent research to perform flight tests with tufts installed on the wing. Assuming the second state models the local effects of the stall strip. Further research should investigate the use of the model for leading edge stalls specifically. The flow separation model used is typically associated with trailing edge stalls.

No unsteady contributions were found for the wing separation state. It is important to note that these results do not imply that unsteady aerodynamic effects are absent on the rest of the wing. Instead, the available data does not provide significant information for the stall regime in these regions. Furthermore, the deep dynamic stall maneuver proved difficult to execute and further research should work on reliable maneuvers in the high angle of attack regime.

The lift model has been extended and now includes two separation states, as well as a pitch rate and elevator deflection term. There remains a large correlation between the bias and Kirchhoff's term. Although reduced, future work should try to reduce it even further. Furthermore, the effect of the elevator deflection is found to be negative. This is counter-intuitive and likely caused by a high correlation between the elevator deflection and the angle of attack. This can be eliminated by including excitations of the elevator at low angles of attack.

The drag model was changed and now includes a quadratic relation to the lift coefficient. It matches the low and high angle of attack extremes more closely compared to the previous model. Most importantly, it avoids negative drag for negative angles of attack. Still, it would be useful to include more data at negative angles of attack to improve knowledge of that regime.

The pitch moment model saw the most major iteration. It now includes a model for the center of pressure and its shift during a stall. The determination of its location is of great interest for aerodynamic modeling, and future research should investigate it in more detail. Next, a new formulation for the elevator control effectiveness is obtained. The model shows a stagnation of the static pitch moment. Further work should specifically look at that high angle of attack regime where this is observed.

For the drag and pitch moment models, a new dependency on the lift coefficient is introduced. The lift model itself contains errors, which means those are propagated to the drag and pitch moment models. Future work should investigate this propagation. More broadly speaking, an estimate of the confidence in the output of the model is desirable. This can be achieved using uncertainty propagation, which is an area that should be investigated in the future.

C. Stall Simulation

The ultimate goal of this research is to teach pilots how to safely operate an aircraft during a stall. This paper contributes by improving the accuracy of the aerodynamic force and moment models during the stall. However, future work should determine its effectiveness for pilot training.

First, a study should be performed to judge the propagation of the aerodynamic model towards the aircraft states. By simulating the aircraft dynamics with the aerodynamic model the aircraft states can be compared against the measured states. This might reveal deficiencies present in the model. Additionally, it may also be used to determine if the added complexity is worthwhile.

Similarly, pilot-in-the-loop simulations can determine if it is necessary to include model terms. Through the use of just-noticeable-differences experiments, it can also be determined if the parameter variances found in this work are low enough. Otherwise, more data must be gathered.

VI. Conclusion

Stall model identification aims to improve upset prevention and recovery training by enabling accurate flight simulation in stall. This paper contributes to this goal by introducing new flight maneuvers for the Cessna Citation II: the dynamic stall and the deep dynamic stall. These maneuvers reduced τ_1 and τ_2 parameter correlation from 0.73 to 0.06, improving model reliability. Furthermore, a new nonlinear parameter estimation technique was developed, called separable nonlinear least squares. This method significantly reduces the computational time for nonlinear parameter estimation. In addition, larger data sets can be processed, ensuring greater consistency and reducing the risk of overfitting to certain maneuvers. In the future, data sets using stall and non-stall data may be considered to bridge the existing gap of transitioning from nominal to stall models. Further methodological improvements can be made by integrating the separable nonlinear least squares method with model structure selection methods. An improved longitudinal stall model is introduced in this paper, where MSE values for the lift, drag and pitch moment coefficients were reduced by 32%, 29%, and 27%, respectively. The new model should be tested in a simulation where aircraft states can be analyzed. Additionally, pilot-in-the-loop tests should be performed to review the pilots' perception of the new model. Further research should extend the developed longitudinal model to the lateral dynamics of the aircraft using the new methodology. In conclusion, multiple advances have been made that contribute to the overarching goal of improving upset prevention and recovery training, paving the way to safer flight.

Acknowledgments

The author wishes to thank the test pilots, aircraft technicians, academic staff, and other members of the stall task force for their help during the research project.

References

[1] Bromfield, M. A., and Landry, S. J., "Loss of Control In Flight – time to re-define?" *AIAA Aviation 2019 Forum*, AIAA, Dallas, Texas, 2019. https://doi.org/10.2514/6.2019-3612.

[2] "A Statistical Analysis of Commercial Aviation Accidents 1958-2023," Airbus, SAS, X00D17008863, 2024.

[3] "Statistical Summary of Commercial Jet Airplane Accidents," Boeing, Co, 326909, 2023.

[4] "Loss of Control In-Flight Accident Analysis Report," International Air Transport Association, 2019.

[5] Belcastro, C. M., Foster, J., Newman, R. L., Groff, L., Crider, D. A., and Klyde, D. H., "Preliminary Analysis of Aircraft Loss of Control Accidents: Worst Case Precursor Combinations and Temporal Sequencing," *AIAA Guidance, Navigation, and Control Conference*, AIAA, National Harbor, Maryland, 2014. https://doi.org/10.2514/6.2014-0612.

[6] Jacobson, S. R., "Aircraft Loss of Control Causal Factors and Mitigation Challenges," *AIAA Guidance, Navigation, and Control Conference*, AIAA, Toronto, Ontario, Canada, 2010. https://doi.org/10.2514/6.2010-8007.

[7] Lambregts, A. A., Nesemeier, G., Wilborn, J. E., and Newman, R. L., "Airplane Upsets: Old Problem, New Issues," *AIAA Modeling and Simulation Technologies Conference and Exhibit*, AIAA, Honolulu, Hawaii, 2008. https://doi.org/10.2514/6.2008-6867.

[8] Crider, D., "Accident Lessons for Stall Upset Recovery Training," *AIAA Guidance, Navigation, and Control Conference*, AIAA, Toronto, Ontario, Canada, 2010. https://doi.org/10.2514/6.2010-8003.

[9] Advani, S., and Field, J., "Upset Prevention and Recovery Training in Flight Simulators," *AIAA Modeling and Simulation Technologies Conference*, AIAA, Portland, Oregon, 2011. https://doi.org/10.2514/6.2011-6698.

[10] "Manual on Aeroplane Upset Prevention and Recovery Training," International Civil Aviation Organization, Doc 10011 AN/506, 2014.

[11] "Stall Prevention and Recovery Training," Federal Aviation Administration, AC 120-109A, 2017.

[12] "Annex I to ED Decision 2019/005/R," European Union Aviation Safety Agency, 2019.

[13] Advani, S. K., Schroeder, J. A., and Burks, B., "Global Implementation of Upset Prevention & Recovery Training," *AIAA Modeling and Simulation Technologies Conference*, AIAA, San Diego, California, USA, 2016. https://doi.org/10.2514/6.2016-1430.

[14] Abramov, N. B., Goman, M. G., Khrabrov, A. N., and Soemarwoto, B. I., "Aerodynamic Modeling for Poststall Flight Simulation of a Transport Airplane," *Journal of Aircraft*, Vol. 56, No. 4, 2019, pp. 1427–1440. https://doi.org/10.2514/1.C034790.

[15] Fischenberg, D., "Identification of an unsteady aerodynamic stall model from flight test data," *20th Atmospheric Flight Mechanics Conference*, AIAA, Baltimore, MD, 1995, pp. 138–146. https://doi.org/10.2514/6.1995-3438.

[16] Singh, J., and Jategaonkar, R., "Flight determination of configurational effects on aircraft stall behavior," *21st Atmospheric Flight Mechanics Conference*, AIAA, San Diego, CA, 1996, pp. 657–665. https://doi.org/10.2514/6.1996-3441.

[17] Singh, J., and Jategaonkar, R. V., "Identification of lateral-directional behavior in stall from flight data," *Journal of Aircraft*, Vol. 33, No. 3, 1996, pp. 627–630. https://doi.org/10.2514/3.46993.

[18] Fischenberg, D., and Jategaonkar, R. V., "Identification of Aircraft Stall Behavior from Flight Test Data," *RTO Meeting Proceedings 11, System Identification for Integrated Aircraft Development and Flight Testing*, NATO, Research and Technology Organization, Madrid, Spain, 1998, pp. 17(1)–17(8). https://doi.org/10.14339/RTO-MP-011.

[19] Morelli, E. A., Cunningham, K., and Hill, M. A., "Global Aerodynamic Modeling for Stall/Upset Recovery Training Using Efficient Piloted Flight Test Techniques," *AIAA Modeling and Simulation Technologies (MST) Conference*, AIAA, Boston, MA, 2013. https://doi.org/10.2514/6.2013-4976.

[20] Dias, J. N., "Nonlinear Lifting-Line Algorithm for Unsteady and Post-stall Conditions," *34th AIAA Applied Aerodynamics Conference*, AIAA, Washington, D.C., 2016. https://doi.org/10.2514/6.2016-4164.

[21] Dias, J. N., "Stall Model Identification Using Flight Path Reconstruction of Multiple Maneuvers," *AIAA Aviation 2023 Forum*, AIAA, San Diego, CA, 2023. https://doi.org/10.2514/6.2023-3781.

[22] Van Horssen, L. J., "Aerodynamic Stall Modeling for the Cessna Citation II," M.Sc. Thesis, Control & Operations Department, Faculty of Aerospace Engineering, Delft University of Technology, Delft, the Netherlands, 2016. URL http://repository.tudelft.nl/.

[23] Van Ingen, J., "Dynamic Stall Modeling for the Cessna Citation II," M.Sc. Thesis, Control & Operations Department, Faculty of Aerospace Engineering, Delft University of Technology, Delft, the Netherlands, 2017. URL http://repository.tudelft.nl/.

[24] Marschalk, S., "Stall Buffet Modeling using Swept Wing Flight Test Data," M.Sc. Thesis, Control & Operations Department, Faculty of Aerospace Engineering, Delft University of Technology, Delft, the Netherlands, 2019. URL http://repository.tudelft.nl/.

[25] Luteijn, P. C., "Towards a Stall Model for the Fokker 100," M.Sc. Thesis, Control & Operations Department, Faculty of Aerospace Engineering, Delft University of Technology, Delft, the Netherlands, 2020. URL http://repository.tudelft.nl/.

[26] De Meester, E. H. P., "Towards an Asymmetric Stall Model for the Fokker 100," M.Sc. Thesis, Control & Operations Department, Faculty of Aerospace Engineering, Delft University of Technology, Delft, the Netherlands, 2021. URL http://repository.tudelft.nl/.

[27] Delfosse, A., "Asymmetric Stall and Control Effectiveness Reduction Modeling for the Cessna Citation II," M.Sc. Thesis, Control & Operations Department, Faculty of Aerospace Engineering, Delft University of Technology, Delft, the Netherlands, 2021. URL http://repository.tudelft.nl/.

[28] Brill, P. A. R., "Improving Stall Model Accuracy through Optimal Data Slicing by Analyzing Kirch-hoff Stall Parameter Estimate Behaviour," M.Sc. Thesis, Control & Operations Department, Faculty of Aerospace Engineering, Delft University of Technology, Delft, the Netherlands, 2023. URL http://repository.tudelft.nl/.

[29] De Fuijk, D., "Asymmetric Cessna Citation II Stall Model Identification using a Roll Moment-based Kirchhoff Method," M.Sc. Thesis, Control & Operations Department, Faculty of Aerospace Engineering, Delft University of Technology, Delft, the Netherlands, 2023. URL http://repository.tudelft.nl/.

[30] Van Ingen, J. B., de Visser, C. C., and Pool, D. M., "Stall Model Identification of a Cessna Citation II from Flight Test Data Using Orthogonal Model Structure Selection," *AIAA Scitech 2021 Forum*, AIAA, 2021. https://doi.org/10.2514/6.2021-1725.

[31] Golub, G. H., and Pereyra, V., "The Differentiation of Pseudo-Inverses and Nonlinear Least Squares Problems Whose Variables Separate," *SIAM Journal on Numerical Analysis*, Vol. 10, No. 2, 1973, pp. 413–432. https://doi.org/10.1137/0710036.

[32] Golub, G., and Pereyra, V., "Separable nonlinear least squares: the variable projection method and its applications," *Inverse Problems*, Vol. 19, No. 2, 2003, pp. R1–R26. https://doi.org/10.1088/0266-5611/19/2/201.

[33] De Visser, C. C., "Global Nonlinear Model Identification with Multivariate Splines," Ph.D. thesis, Delft University of Technology, Delft, the Netherlands, July, 2011.

[34] Goman, M., and Khrabrov, A., "State-space representation of aerodynamic characteristics of an aircraft at high angles of attack," *Astrodynamics Conference*, AIAA, 1992. https://doi.org/10.2514/6.1992-4651.

[35] Leishman, J. G., and Beddoes, T. S., "A Semi-Empirical Model for Dynamic Stall," *Journal of the American Helicopter Society*, Vol. 34, No. 3, 1989, pp. 3–17. https://doi.org/10.4050/JAHS.34.3.3.

[36] Truong, K. V., "Modeling Longitudinal Unsteady Aerodynamics of a Wing-Tail Transport Aircraft based on a Dynamic Stall Model," , 2 2018. https://doi.org/10.13140/RG.2.2.14420.71043.

[37] Woods, L. C., *The theory of subsonic plane flow*, Cambridge University Press, Cambridge, England, 2011.

[38] Anderson, J. D., *Fundamentals of Aerodynamics*, 6th ed., McGraw-Hill Education, New York, NY, 2017.

[39] Marschalk, S., Luteijn, P. C., van Os, D., Pool, D. M., and de Visser, C. C., "Stall buffet modeling using swept wing flight test data," *AIAA Scitech 2021 Forum*, AIAA, VIRTUAL EVENT, 2021. https://doi.org/10.2514/6.2021-0286.

[40] de Visser, C. C., and Pool, D. M., "Stalls and Splines: Current Trends in Flight Testing and Aerodynamic Model Identification," *Journal of Aircraft*, Vol. 60, No. 5, 2023, pp. 1480–1502. https://doi.org/10.2514/1.c037283.

[41] Herbold, J. A., "Aircraft Stall Dynamics: Improved Longitudinal Stall Modeling with Seperable Nonlinear Least Squares and Dynamic Stall Maneuvers," M.Sc. Thesis, Control & Operations Department, Faculty of Aerospace Engineering, Delft University of Technology, Delft, the Netherlands, 2025. URL http://repository.tudelft.nl/.

[42] Jacobs, E. N., and Clay, W. C., "Characteristics of The NACA 23012 Airfoil from Full-Scale and Variable-Density Tunnels," NASA, 1936.

[43] Endou, N., and Shidama, Y., "Differentiation in normed spaces," *Formalized Mathematics*, Vol. 21, No. 2, 2013, pp. 95–102. https://doi.org/10.2478/forma-2013-0011.

[44] O'Leary, D. P., and Rust, B. W., "Variable projection for nonlinear least squares problems," *Computational Optimization and Applications*, Vol. 54, No. 3, 2013, pp. 579–593. https://doi.org/10.1007/s10589-012-9492-9.

[45] Mahata, K., and Söderström, T., "Large sample properties of separable nonlinear least squares estimators," *IEEE Transactions on Signal Processing*, Vol. 52, No. 6, 2004, pp. 1650–1658. https://doi.org/10.1109/TSP.2004.827227.

[46] Klein, V., and Morelli, E., "Aircraft System Identification Theory and Practice," AIAA, 2006.

[47] Mulder, J. A., Van Staveren, W. H. J. J., Van Der Vaart, J. C., De Weerdt, E., De Visser, C. C., In 't Veld, A. C., and Mooij, E., "Lecture Notes AE3202 Flight Dynamics," Delft University of Technology, 2013.

A. Aircraft Reference Frames

In the paper, three reference frames are used. These reference frames define in which direction forces and moments act. The first reference frame is the earth reference frame, as seen in Figure 14. The origin of this frame is in the center of gravity of the aircraft. The XY-plane is tangential to the surface of the earth, with the X-axis pointing north and the Y-axis pointing east. The Z-axis is perpendicular to the XY-plane and points towards the center of the earth.

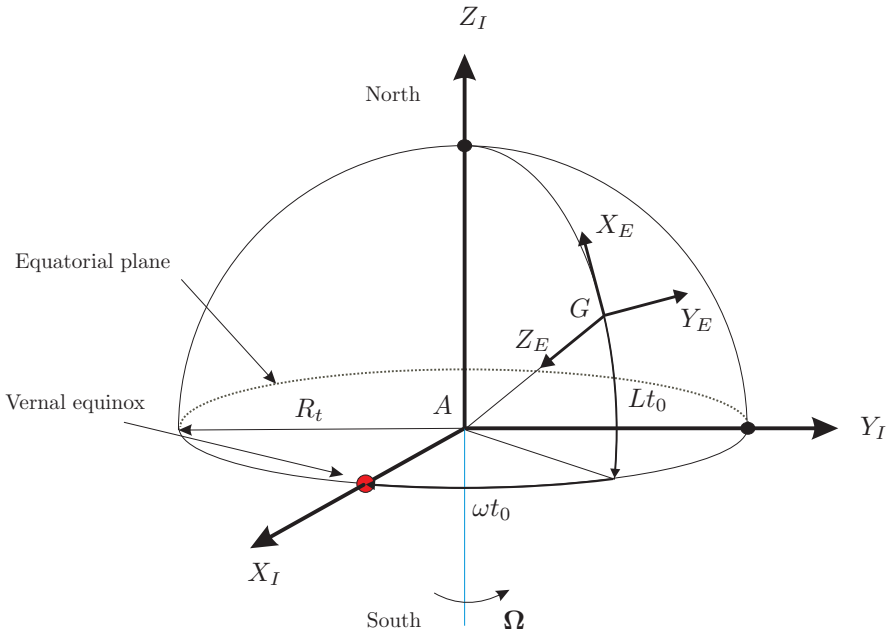

Fig. 14 Earth reference frame, adapted from [47]

The second reference frame, most relevant for flight dynamics modeling, is the body reference frame. This is the frame in which aerodynamic forces and moments are typically expressed. The X-axis is defined through the nose of the aircraft. The Y-axis lies in the horizontal plane and points towards the right wing. Lastly, the Z-axis points downwards and is perpendicular to the X and Y-axis. This reference frame is depicted in Figure 15. The Euler angles can be used to rotate from the earth frame to the body frame. These angles are defined as yaw ψ, pitch θ and roll φ. Using these three angles the rotation matrix $\mathbb{T}_{bE}$ can be constructed:

$$\mathbb{T}_{bE} = \begin{bmatrix} \cos\theta\cos\psi & \cos\theta\sin\psi & -\sin\theta \\ \sin\varphi\sin\theta\cos\psi - \cos\varphi\sin\psi & \sin\varphi\sin\theta\sin\psi + \cos\varphi\cos\psi & \sin\varphi\cos\theta \\ \cos\varphi\sin\theta\cos\psi + \sin\varphi\sin\psi & \cos\varphi\sin\theta\sin\psi - \sin\varphi\cos\psi & \cos\varphi\cos\theta \end{bmatrix} \tag{41}$$

Lastly, the aerodynamic reference frame can be constructed. This frame is aligned with the velocity vector of the incoming undisturbed air. The lift and drag of an aircraft are defined in this reference frame. Its relation to the body frame can be seen in Figure 16. The two angles are the angle of attack α and sideslip β. To rotate from the body frame

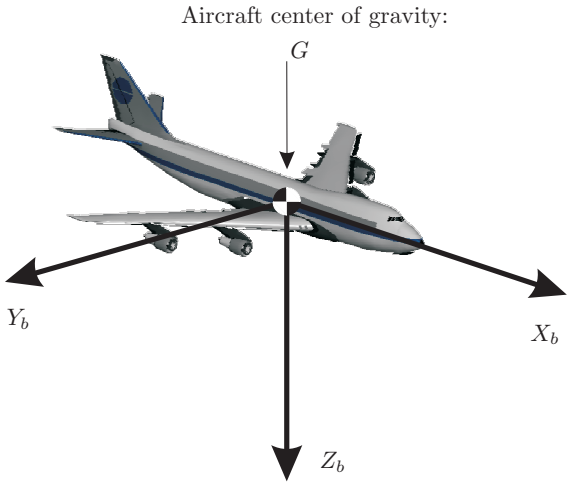

Fig. 15 Body reference frame, adapted from [47]

to the aerodynamic frame rotation matrix $\mathbb{T}_{ab}$ can be used. This rotation matrix is defined as follows:

$$\mathbb{T}_{ab} = \begin{bmatrix} \cos\beta\cos\alpha & \sin\beta & \cos\beta\sin\alpha \\ -\sin\beta\cos\alpha & \cos\beta & -\sin\beta\sin\alpha \\ -\sin\alpha & 0 & \cos\alpha \end{bmatrix} \tag{42}$$

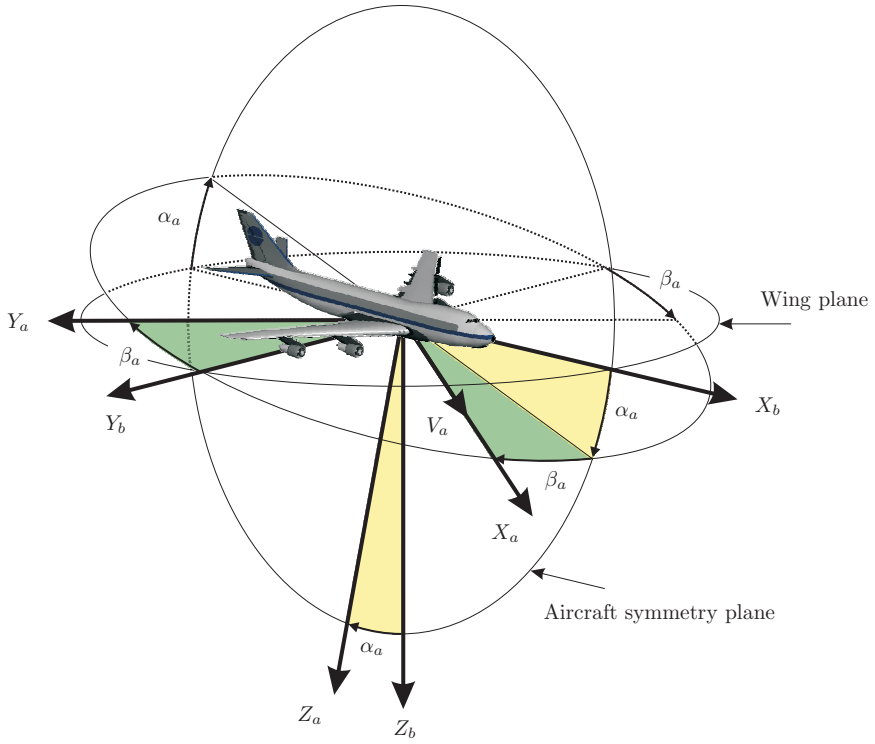

Fig. 16 Aerodynamic reference frame, adapted from [47]

B. Model Structures

A. Lift Model

The lift models used during exploration are summarized in Table 18.

Table 18 Overview of all experimental lift model structures derived from the base regressors. All models include C_{L_0}.

	$(\alpha - 6°)_+^2$	$K_{L,ss}$	$K_{L,w}$	$\frac{q\bar{c}}{V}$	δ_e
Model CL-I	*	*			
Model CL-II		*			
Model CL-III		*	*		
Model CL-IV		*	*	*	
Model CL-V		*	*		*
Model CL-VI		*	*	*	*

B. Drag Model

The drag models used during exploration are summarized in Table 19.

Table 19 Overview of all experimental drag model structures derived from the base regressors. All models include C_{D_0}.

	C_T	$\frac{q\bar{c}}{V}$	δ_e	α	α^2	C_L	C_L^2	$(1 - X_{ss})$	$(1 - X_{ss})$	$K_{D,ss}$	$K_{D,w}$
Model CD-I	*		*	*				*			
Model CD-II	*		*	*				*	*		
Model CD-III	*	*	*					*	*		
Model CD-IV	*	*	*	*				*	*		
Model CD-V	*	*	*		*			*	*		
Model CD-VI	*	*	*	*	*			*	*		
Model CD-VII	*	*	*			*		*	*		
Model CD-VIII	*	*	*				*	*	*		
Model CD-IX	*	*	*			*	*	*	*		
Model CD-X	*	*	*			*					
Model CD-XI	*	*	*				*				
Model CD-XII	*	*	*			*	*				
Model CD-XIII	*	*	*							*	*
Model CD-XIV	*	*	*					*	*	*	*

C. Pitch Model

The first model structure for the pitch model is derived from Van Ingen et al. [30].

$$\textbf{Model Cm-I}: \quad C_m = C_{m_0} + C_{m_\alpha}\alpha + C_{m_{X\delta_e}} \max(1/2, X)\delta_e + C_{m_{C_T}} C_T \tag{43}$$

The other model structures are summarized in Table 20. They are supplemented with training MSE on the pitch moment coefficient as not each model is mentioned separately in the main body. Furthermore, the percentage difference from the model by Van Ingen et al. [30] is presented.

Table 20 Overview of all pitch model structures derived from the base regressors. Differences are measured against the pitch model of Van Ingen et al. [30].

	K_0	K_1	$K_2^{1/2}$	K_2^1	K_2^2	K_S	$(1-X)$	$X\delta_e$	C_m MSE	**Difference** [%]
Model Cm-II	*								3.86×10^{-4}	96.7
Model Cm-III		*							3.39×10^{-4}	72.6
Model Cm-IV	*	*							1.53×10^{-4}	−22.2
Model Cm-V	*		*						2.17×10^{-4}	10.8
Model Cm-VI		*	*						3.33×10^{-4}	69.9
Model Cm-VII	*	*	*						1.51×10^{-4}	−22.8
Model Cm-VIII	*			*					2.50×10^{-4}	27.6
Model Cm-IX		*		*					3.32×10^{-4}	69.4
Model Cm-X	*	*		*					1.51×10^{-4}	−23.0
Model Cm-XI	*				*				2.486×10^{-4}	26.3
Model Cm-XII		*			*				3.30×10^{-4}	68.2
Model Cm-XIII	*	*			*				1.49×10^{-4}	−24.1
Model Cm-XIV						*			4.62×10^{-4}	135.3
Model Cm-XV	*					*			2.52×10^{-4}	28.4
Model Cm-XVI							*		3.45×10^{-4}	75.8
Model Cm-XVII	*						*		1.62×10^{-4}	−17.4
Model Cm-XVIII		*					*		3.30×10^{-4}	68.4
Model Cm-XIX	*	*					*		1.47×10^{-4}	−24.9
Model Cm-XX	*		*				*		1.62×10^{-4}	−17.6
Model Cm-XXI		*	*				*		3.18×10^{-4}	62.0
Model Cm-XXII	*	*	*				*		1.41×10^{-4}	−27.9
Model Cm-XXIII	*			*			*		1.61×10^{-4}	−17.9
Model Cm-XXIV		*		*			*		3.17×10^{-4}	61.7
Model Cm-XXV	*	*		*			*		1.39×10^{-4}	−29.1
Model Cm-XXVI	*				*		*		1.57×10^{-4}	−20.2
Model Cm-XXVII		*			*		*		3.18×10^{-4}	61.9
Model Cm-XXVIII	*	*			*		*		1.40×10^{-4}	−28.5
Model Cm-XXIX						*	*		1.80×10^{-4}	−8.3
Model Cm-XXX	*					*	*		1.62×10^{-4}	−17.6
Model Cm-XXXI	*							*	1.68×10^{-4}	−14.5
Model Cm-XXXII		*						*	3.06×10^{-4}	56.0
Model Cm-XXXIII	*	*						*	1.42×10^{-4}	−27.8
Model Cm-XXXIV	*		*					*	1.46×10^{-4}	−25.8
Model Cm-XXXV		*	*					*	3.06×10^{-4}	55.8
Model Cm-XXXVI	*	*	*					*	1.40×10^{-4}	−28.7
Model Cm-XXXVII	*			*				*	1.57×10^{-4}	−20.2

Continues on the next page

Table 20 Overview of all pitch model structures derived from the base regressors. Differences are measured against the pitch model of Van Ingen et al. [30]. (continued)

	K_0	K_1	$K_2^{1/2}$	K_2^1	K_2^2	*Singh*	$(1-X)$	$X\delta_e$	C_m MSE	**Difference** [%]
Model Cm-XXXVIII		*		*				*	3.04×10^{-4}	55.1
Model Cm-XXXIX	*	*		*				*	1.41×10^{-4}	−27.9
Model Cm-XL	*				*			*	1.63×10^{-4}	−16.9
Model Cm-XLI		*			*			*	2.98×10^{-4}	51.9
Model Cm-XLII	*	*			*			*	1.41×10^{-4}	−28.3
Model Cm-XLIII						*		*	2.08×10^{-4}	5.8
Model Cm-XLIV	*					*		*	1.52×10^{-4}	−22.7
Model Cm-XLV							*	*	3.27×10^{-4}	66.5
Model Cm-XLVI	*						*	*	1.45×10^{-4}	−26.1
Model Cm-XLVII		*					*	*	2.85×10^{-4}	45.1
Model Cm-XLVIII	*	*					*	*	1.39×10^{-4}	−29.1
Model Cm-XLIX	*		*				*	*	1.42×10^{-4}	−27.7
Model Cm-L		*	*				*	*	2.84×10^{-4}	45.0
Model Cm-LI	*	*	*				*	*	1.37×10^{-4}	−30.1
Model Cm-LII	*			*			*	*	1.44×10^{-4}	−26.4
Model Cm-LIII		*		*			*	*	2.83×10^{-4}	44.5
Model Cm-LIV	*	*		*			*	*	1.37×10^{-4}	−30.2
Model Cm-LV	*				*		*	*	1.44×10^{-4}	−26.6
Model Cm-LVI		*			*		*	*	2.81×10^{-4}	43.4
Model Cm-LVII	*	*			*		*	*	1.37×10^{-4}	−30.4
Model Cm-LVIII						*	*	*	1.64×10^{-4}	−16.2
Model Cm-LIX	*					*	*	*	1.43×10^{-4}	−27.3

Part III

Additional Results

6

Pre-filter Analysis

The function of the pre-filter is two-fold. Firstly, it removes contributions from the buffet in the stall. The Kalman filter does not model the buffet dynamics. The buffet therefore would increase the state variance of the filter. Secondly, the states $\dot{p}$, $\dot{q}$, $\dot{r}$, $\dot{\alpha}$ and $\dot{\beta}$ are obtained by numerical differentiation. Numerical differentiation tends to amplify high-frequency noise. Using a low-pass filter, the high-frequency content can be reduced.

Table 6.1 shows the parameters that have been filtered. The third column shows the cut-off frequencies selected by Van Ingen [23]. However, these were found to be very restrictive. Higher-frequency signals are required especially for the identification of unsteady effects. For the identified value of $\tau_1 = 0.2547$ frequency signals up to 4 Hz are required. The control inputs, performed during test flights, are another reason to increase the cut-off frequencies. These quasi-random inputs have a higher maximum frequency than 1.5 Hz. Any effects from those inputs would not be present in the aerodynamic coefficients derived from the accelerations and body rates.

A new analysis of the cut-off frequency was performed. Data from the four most recent stall test flights were used. Furthermore, for comparison two recent flights for flight test practicals were analyzed. These were included to provide a comparison between data including and excluding stalls. A power spectral density is made of the data. These power spectra are presented in the left plots of Figs. 6.1 to 6.11. The power spectra were calculated with the periodogram MATLAB function[1]. Afterwards, a moving average filter with 100 mean points was applied using the movmean MATLAB function[2].

Analyzing the plots, similar conclusions can be drawn as Marschalk [24] made. For the accelerations, it is clear that the longitudinal acceleration a_x in Fig. 6.1 has a range of frequencies in which buffeting happens. Furthermore, it is orders of magnitude lower than a_y and a_z. The lateral acceleration a_y in Fig. 6.2 does have two clear buffet peaks around 6 and 10 Hz. To a lesser extent, there is also a peak at 15 Hz, this has not been modeled previously but could be related to the new dynamic stall maneuvers. The normal acceleration a_z in Fig. 6.3 has a buffet peak at 12 Hz. These results are in line with previous results [22]. From the power spectra, it is determined that the previous cut-off frequencies for a_x, a_y and a_z eliminate the buffet contributions, but are very close to the maneuvering contributions. It is chosen to increase the cut-off frequencies to 4, 4 and 8 Hz for a_x, a_y and a_z respectively.

For the body rates, no specific analysis has been done prior. The results presented in Figs. 6.4 to 6.6 are new. Observe that the peaks for the lateral acceleration a_y are also present in the lateral body rates p and r. The same can be said for the normal acceleration a_z, which transfers to the pitch rate q. Furthermore, a wider range of low-frequency content is visible. This likely has to do with the direct response of the aircraft to control inputs. The previously selected cut-off frequencies are inappropriate to capture this behavior. Therefore, the cut-off is moved to 5, 5 and 4 Hz for p, q and r respectively.

Moving to the control surface deflections, these already had a relatively high cut-off at 4 Hz. Looking at Figs. 6.7 to 6.9, it can be seen that the signal content goes up to about 5 Hz. For the ailerons, there is no visible high-frequency content and the cut-off is set to 5 Hz. For the elevator, the signal strength at 4 Hz is higher than for the elevator. To be on the safe side, the cut-off frequency here is set to 6 Hz, without

[1] https://nl.mathworks.com/help/signal/ref/periodogram.html

[2] https://nl.mathworks.com/help/matlab/ref/movmean.html

introducing much high-frequency content. For the rudder, there are clear effects from the lateral buffet. The data shows a big peak at 6 Hz. To attenuate this peak the cut-off frequency is set to 4 Hz.

Lastly, the angle of attack and sideslip signals of the air data boom are analyzed. The power spectra Figs. 6.10 and 6.11 show signal strength in the frequency range of 8 to 12 Hz. These cannot be fully attributed to any prior frequency mode. The most probable cause is vibrations in the boom itself. To attenuate these effects the cut-off frequency is set to 6 Hz.

Besides the analyzed signals, a small note on the time derivatives. The filters used in this and prior work are of the type Butterworth. This is a linear filter. This means that filtering before taking the derivative should be equivalent to filtering after the derivative. This is further derived in Eq. (6.1). In this equation, $B(\omega)$ is the Butterworth filter. This means that the time derivatives by definition are filtered at the same frequency.

$$B(\omega) \cdot \dot{\alpha} = B(\omega) \cdot \frac{\alpha}{s} = \frac{1}{s}(B(\omega) \cdot \alpha) \tag{6.1}$$

To summarize, new cut-off frequencies have been defined. In most cases, the frequency range is widened. The final filter is a fourth-order Butterworth filter with cut-off frequencies as defined in the fourth column of Table 6.1. The result of this filter is visualized for a time segment during stall on the right side of Figs. 6.1 to 6.11

Table 6.1: Cut-off frequencies for the pre-filter of different signals

Parameter	**Symbol**	**Previous work** [23]	**This work**
Longitudinal acceleration	a_x	1.5 Hz	4.0 Hz
Lateral acceleration	a_y	1.5 Hz	4.0 Hz
Normal acceleration	a_z	1.5 Hz	8.0 Hz
Roll rate	p	1.5 Hz	5.0 Hz
Pitch rate	q	1.5 Hz	5.0 Hz
Yaw rate	r	1.5 Hz	4.0 Hz
Aileron deflection	δ_a	4.0 Hz	5.0 Hz
Elevator deflection	δ_e	4.0 Hz	6.0 Hz
Rudder deflection	δ_r	4.0 Hz	4.0 Hz
Angle of attack	α	4.0 Hz	6.0 Hz
Angle of sideslip	β	4.0 Hz	6.0 Hz
Roll acceleration	$\dot{p}$	1.5 Hz[1]	5.0 Hz
Pitch acceleration	$\dot{q}$	1.5 Hz[1]	5.0 Hz
Yaw acceleration	$\dot{r}$	1.5 Hz[1]	4.0 Hz
Angle of attack	$\dot{\alpha}$	4.0 Hz	6.0 Hz
Angle of sideslip	$\dot{\beta}$	4.0 Hz	6.0 Hz

[1] The source mentions 4 Hz, however, due to the lower cut-off frequency filter on p, q and r the effective cut-off frequency is 1.5 Hz

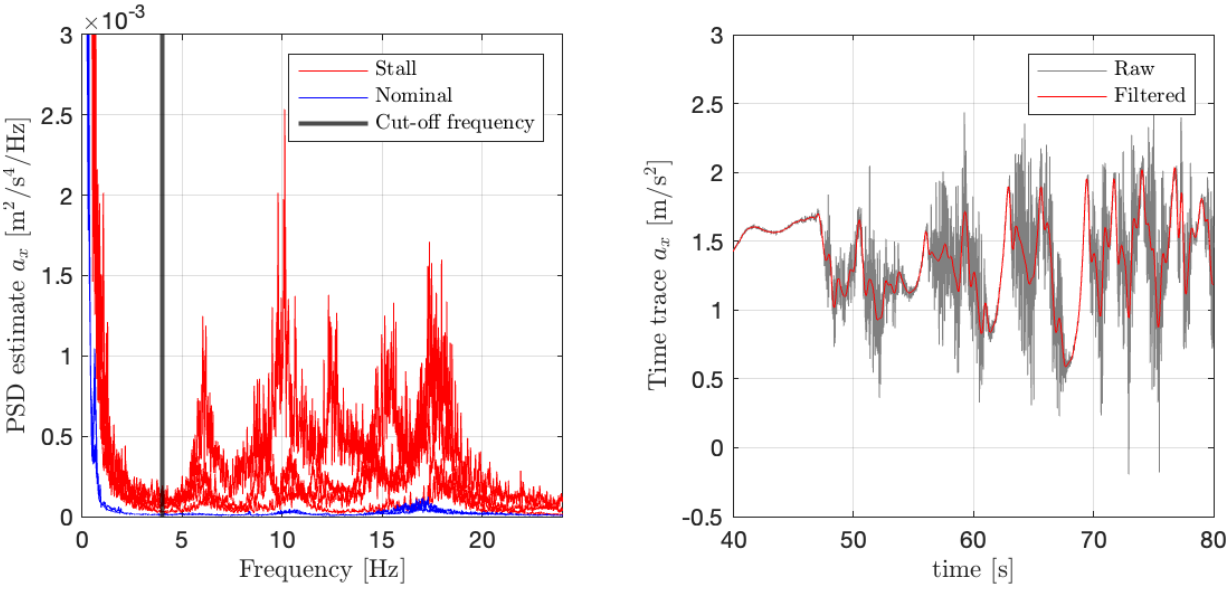

Figure 6.1: Analysis of the cut-off frequency for a_x. Left: Power spectral density estimates for stall and nominal flights. Right: Raw and filtered time trace

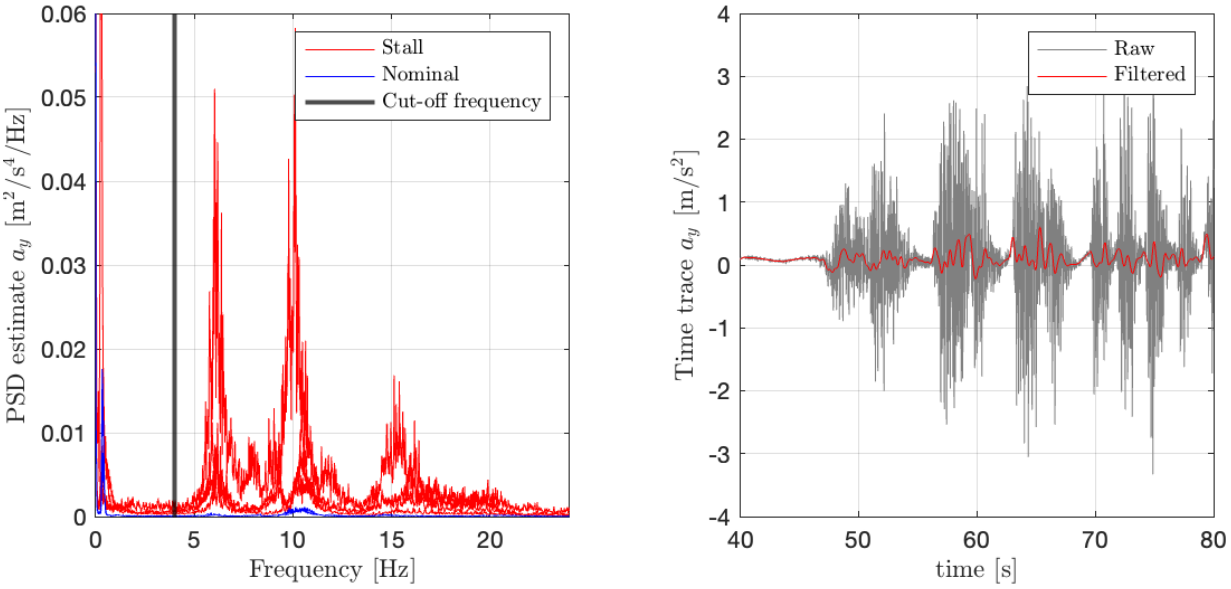

Figure 6.2: Analysis of the cut-off frequency for a_y. Left: Power spectral density estimates for stall and nominal flights. Right: Raw and filtered time trace

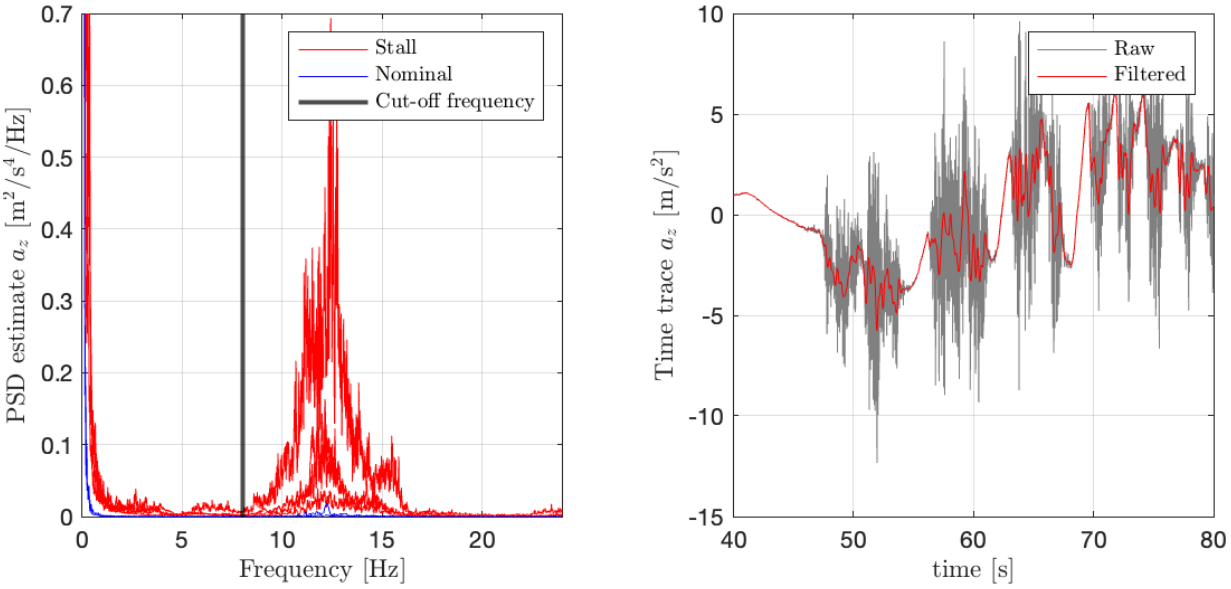

Figure 6.3: Analysis of the cut-off frequency for a_z. Left: Power spectral density estimates for stall and nominal flights. Right: Raw and filtered time trace

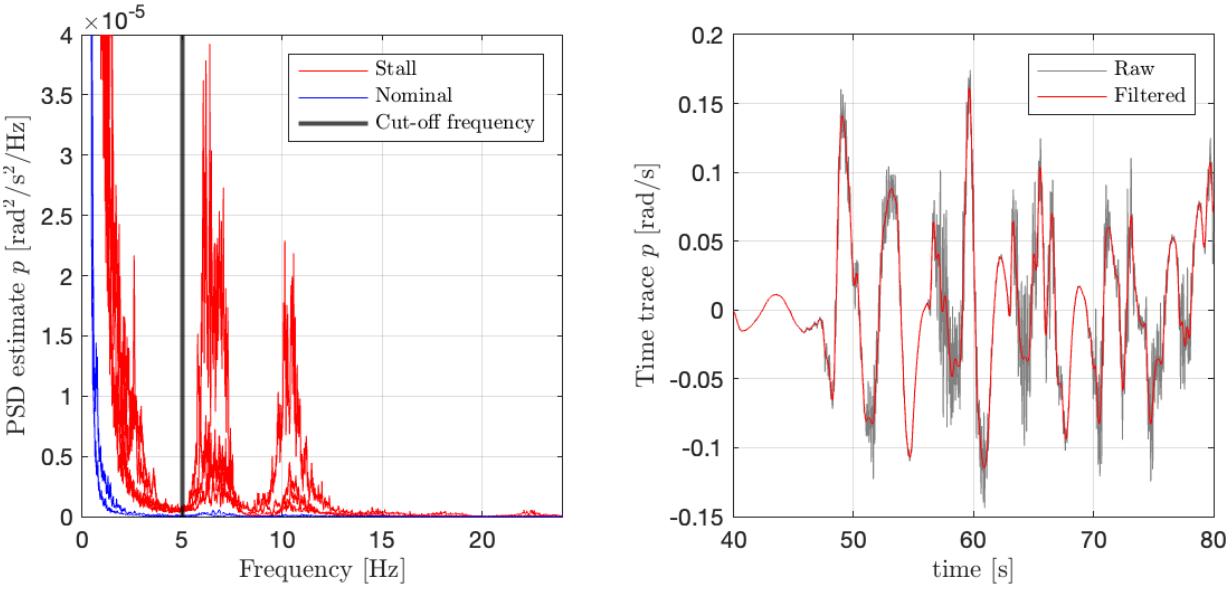

Figure 6.4: Analysis of the cut-off frequency for p. Left: Power spectral density estimates for stall and nominal flights. Right: Raw and filtered time trace

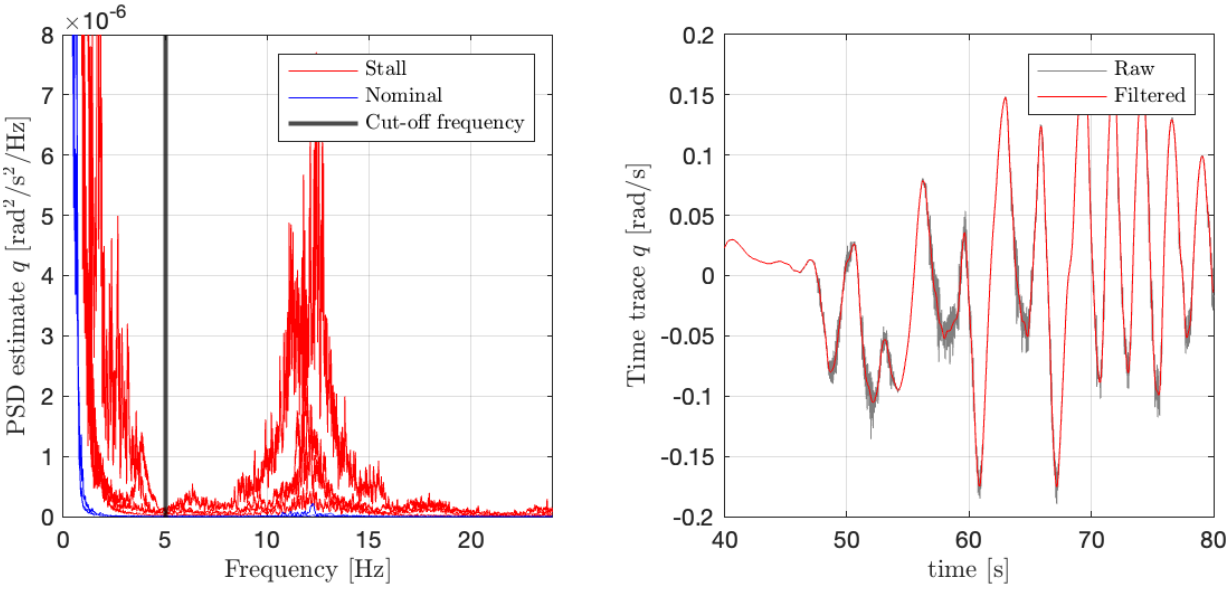

Figure 6.5: Analysis of the cut-off frequency for q. Left: Power spectral density estimates for stall and nominal flights. Right: Raw and filtered time trace

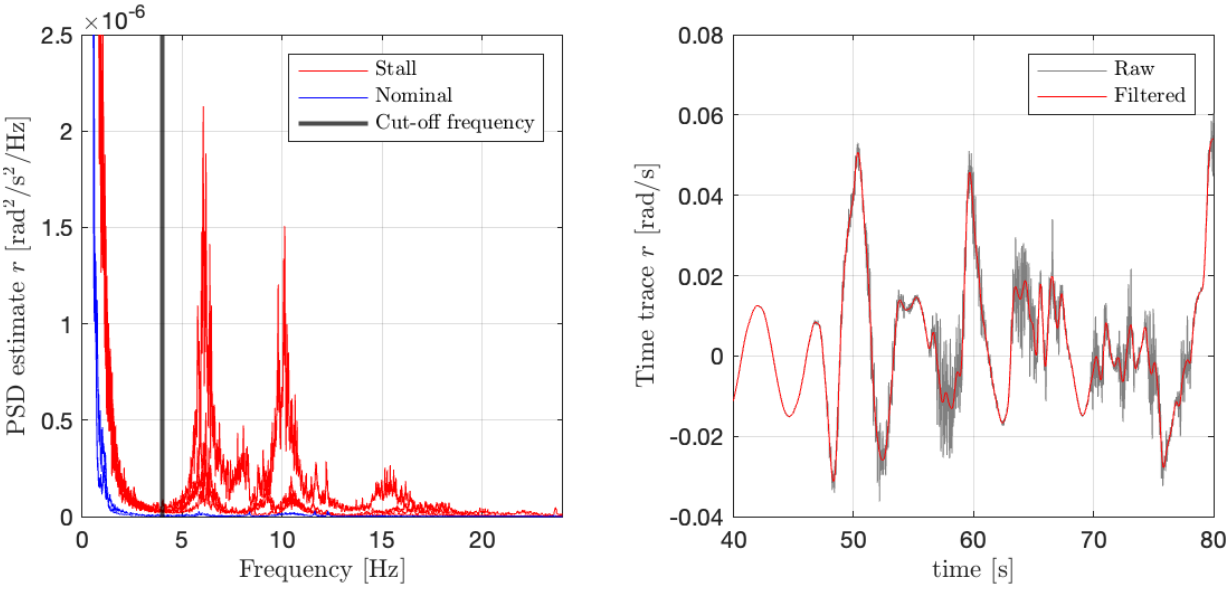

Figure 6.6: Analysis of the cut-off frequency for r. Left: Power spectral density estimates for stall and nominal flights. Right: Raw and filtered time trace

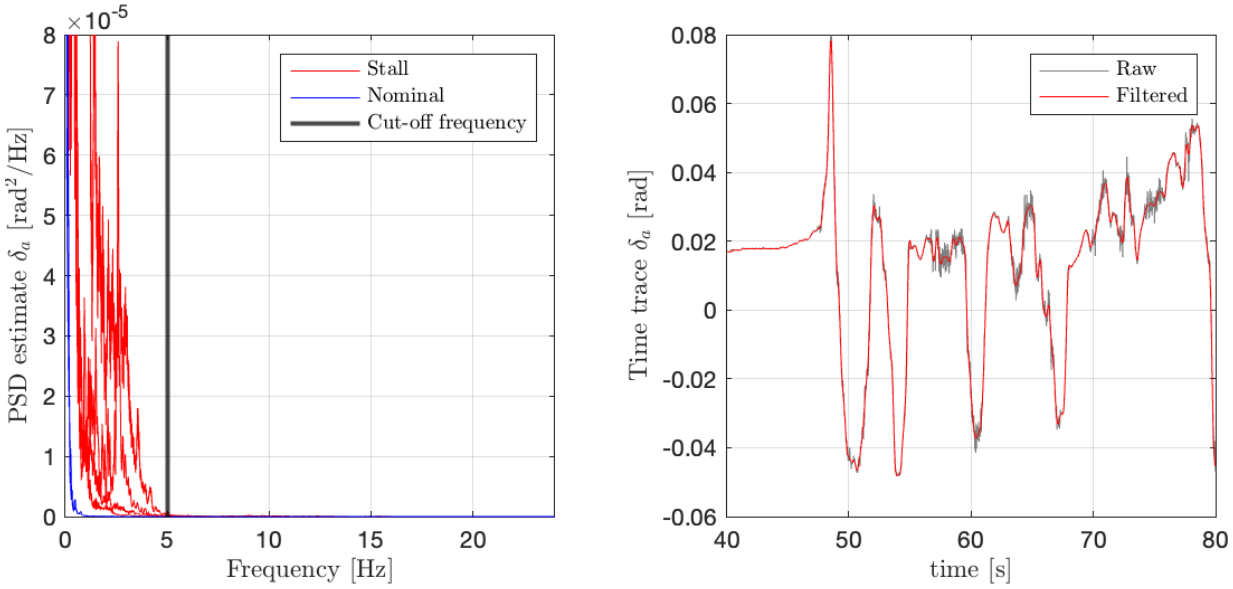

Figure 6.7: Analysis of the cut-off frequency for δ_a. Left: Power spectral density estimates for stall and nominal flights. Right: Raw and filtered time trace

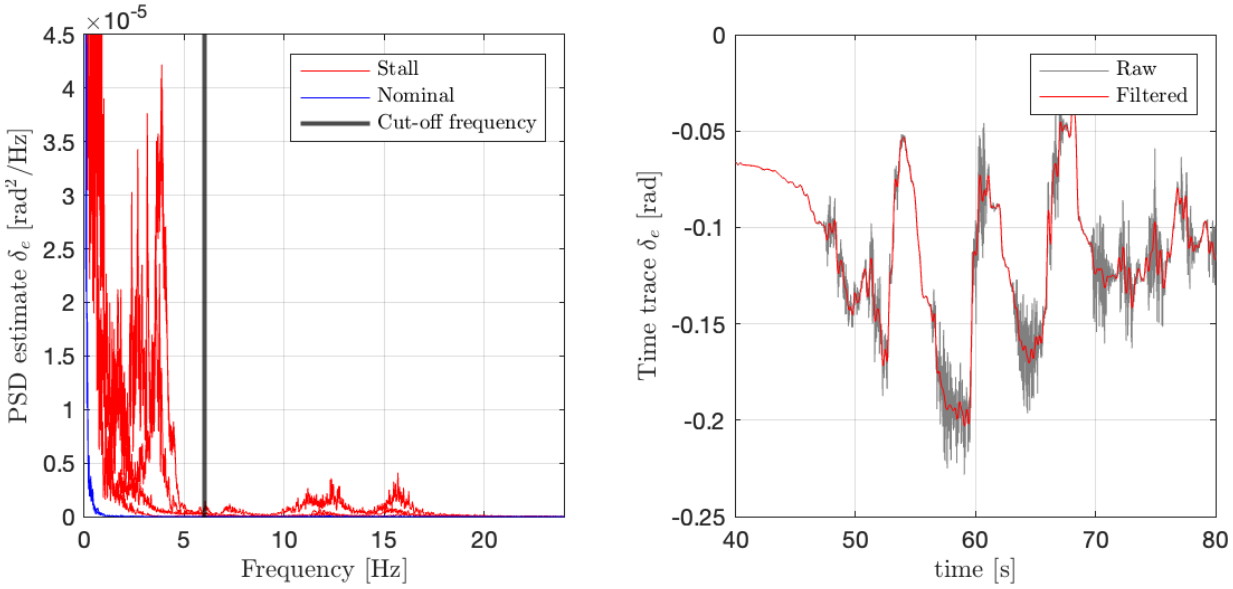

Figure 6.8: Analysis of the cut-off frequency for δ_e. Left: Power spectral density estimates for stall and nominal flights. Right: Raw and filtered time trace

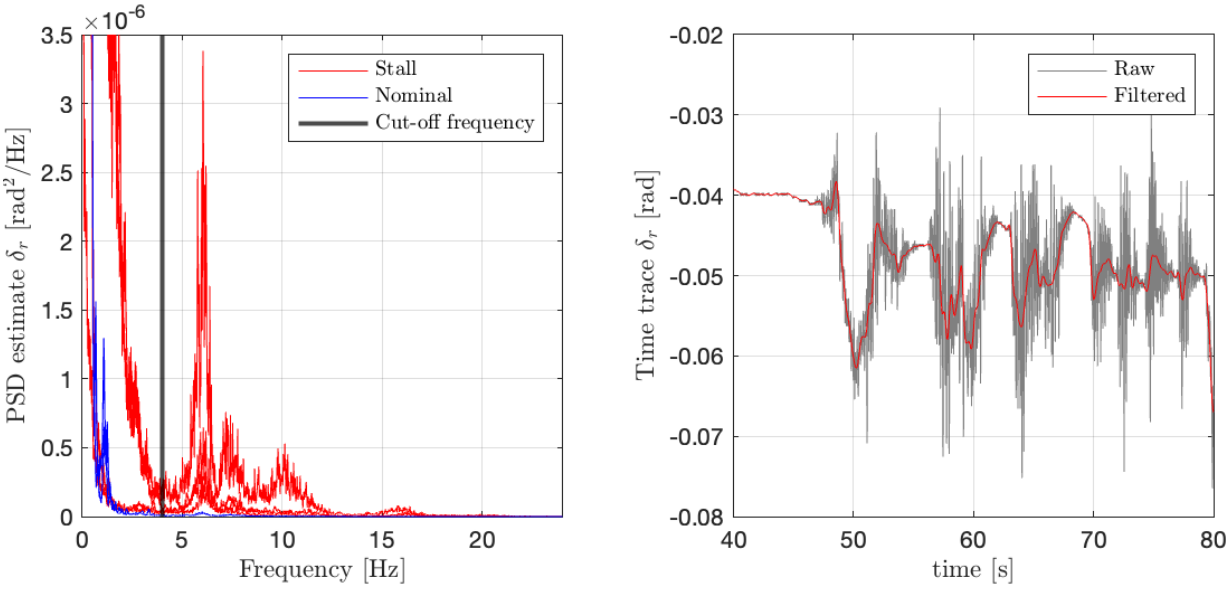

Figure 6.9: Analysis of the cut-off frequency for δ_r. Left: Power spectral density estimates for stall and nominal flights. Right: Raw and filtered time trace

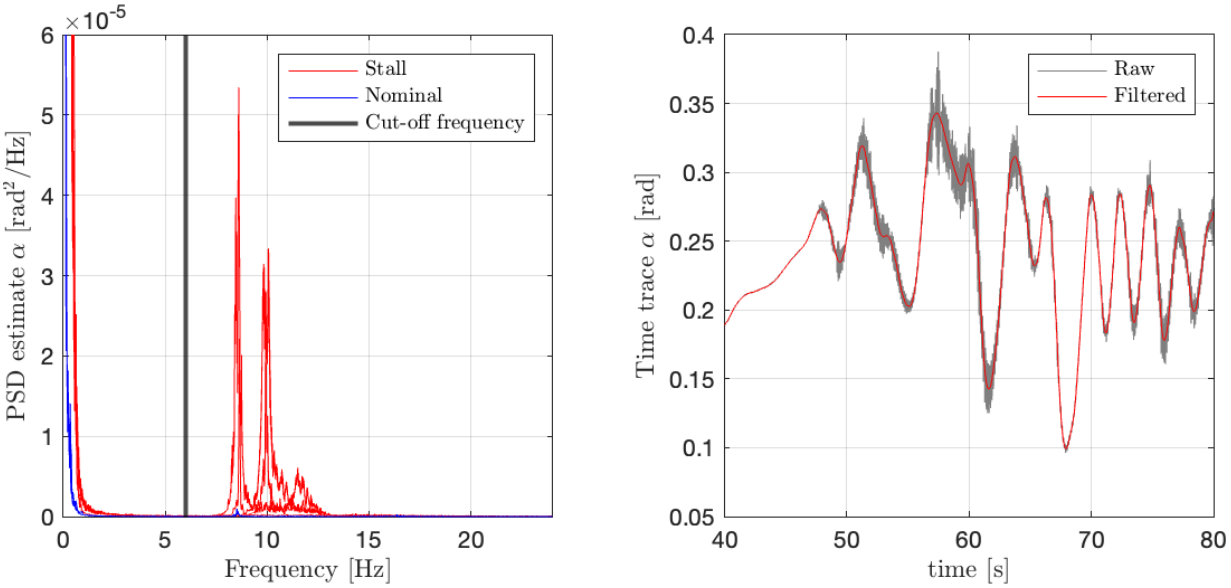

Figure 6.10: Analysis of the cut-off frequency for α. Left: Power spectral density estimates for stall and nominal flights. Right: Raw and filtered time trace

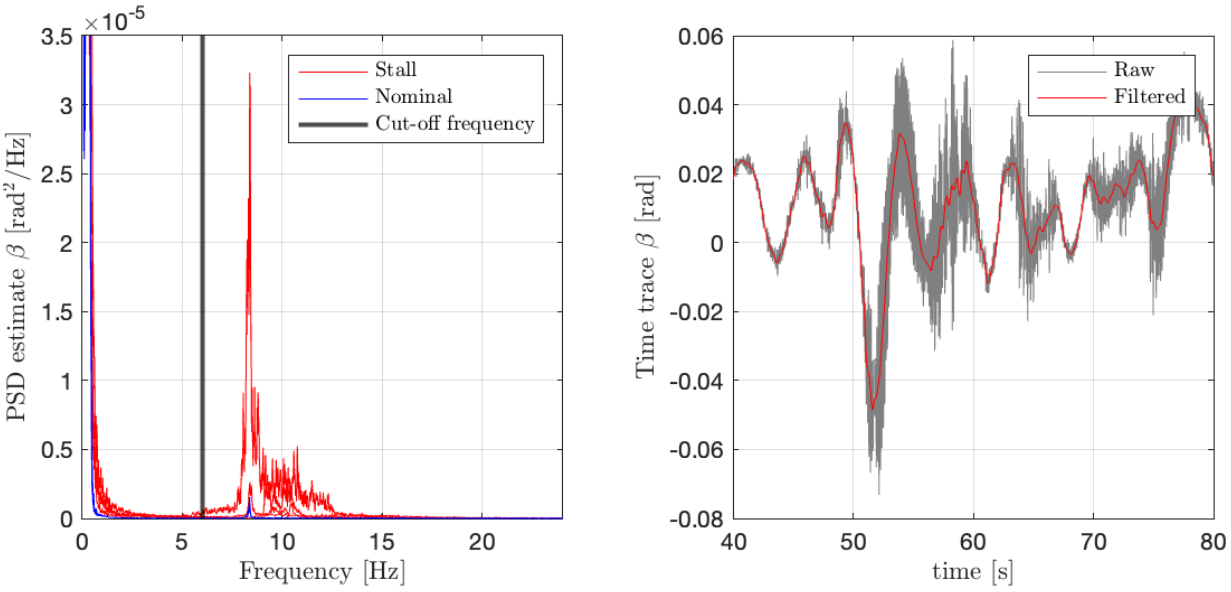

Figure 6.11: Analysis of the cut-off frequency for β. Left: Power spectral density estimates for stall and nominal flights. Right: Raw and filtered time trace

7

Center of Gravity Correction

During the research, it was observed that the center of gravity calculated in previous work did not fall within the stable envelope. The problem lies with the initial step. The first step to calculate the aircraft's center of gravity is the determination of the aircraft's basic empty weight (BEW) properties. In the past, these measured the weight on each landing gear. Currently, three jack points are used as these give more reliable results. The location at which the weight was measured is summarized in Table 7.1. The mass model uses the weight measured at these three points to determine the x and y position of the center of gravity at BEW. The z position is not measured but assumed, the assumption is that the z position is located at 125 in.

Table 7.1: Positions at which the aircraft weight was measured in the past (**Scales**) and currently (**Jacks**)

	Scales		**Jacks**	
Measuring point	$x\ [in]$	$y\ [in]$	$x\ [in]$	$y\ [in]$
Nose	82.01	0	93.70	8.60
Left	300.21	211.08	315.50	121.67
Right	300.21	−211.08	315.50	−121.67

Previous calculations were done with the values presented in the old segment of Table 7.2. It shows that the BEW center of gravity arm, which refers to x, is determined at 275.87 inches. When compared with the center of gravity envelope in Appendix A, it is outside of the stable range. When the aircraft is loaded that problem would only become larger. The only logical explanation is that the values are off. Appendix B shows an official mass and balance sheet checked by a Part 66 certified technician. A summary of the calculation done in the appendix is also presented in the new segment of Table 7.2. Note that this value also falls outside the center of gravity envelope, however, once fuel and payload are added the center of gravity shifts forward into the envelope.

Table 7.2: Comparison between BEW balance calculation in previous work versus corrected in this work

	Old			**New**		
	Mass [lbs]	Arm [in]	Moment [lbs in]	Mass [lbs]	Arm [in]	Moment [lbs in]
Nose	1085	82.01	88981	1447	93.70	135584
Left	4490	300.21	1347942.9	5200	315.50	1640600
Right	4495	300.21	1349444	5278	315.50	1665209
Fuel	-900	285.16	-256644	-2760	285.16	-787041
Extra	N/A	N/A	N/A	88	420	36960
Total	9170	275.87	2529724	9253	290.86	2691311

The mass model requires the BEW to be provided in three separate weights for nose, left, and right. As can be seen in Table 7.2, extra ballast is added to the aircraft. To take that into account the nose, left, and right mass values can be adjusted to retain the same balance. Note, this is just a workaround to comply with the input of the code. The final inputs to the mass model are presented in Table 7.3.

Table 7.3: Corrected input values for the mass model

	Corrected		
	Mass [lbs]	Arm [in]	Moment [lbs in]
Nose	1405.54	93.70	131699
Left	5264.25	315.50	1660870
Right	5343.21	315.50	1685783
Fuel	-2760	285.16	-787041.6
Total	9253	290.86	2691311

This correction has been performed for the dataset used in the final paper. For any further analysis, it is advised to start with the raw flight data and apply the corrections mentioned in this chapter. Furthermore, it is observed that the mass model uses a different frame of reference than the body frame. Especially for the y position this may make a difference. For now, it is assumed that the absolute value of y is small, but in the future, it must be verified that the correct conversion of the reference frame is made.

8

Development of Separable Nonlinear Least Squares

This chapter guides the reader through the development of a separable nonlinear least squares routine for system identification of an aircraft in stall conditions. It starts by identifying the limitations in the current routine and how SNLS could solve this in Section 8.1. Section 8.2 explains how SNLS is implemented in practice, covering the application to stall models, necessary adaptations, and MATLAB implementation. Lastly, the developed methods are tested for their correct implementation in Section 8.3.

8.1. Limitations in Current Methodology

This section aims to define the limitations of the existing non-linear parameter estimation routine. This is a key step to guide the definition of a new routine. It starts by analyzing the implementation of the method and looking for the thought process behind certain choices. Next,

The current method employs a series of flight maneuvers to determine optimal parameter values for the separation equation. A least squares cost function is minimized 300 times for each maneuver to mitigate the effects of local minima and reduce parameter variance. The choice to minimize the cost function independently for each maneuver appears to result from the absence of a covariance metric. Instead, parameter variance is inferred by treating the individual parameter estimates as samples from the true distribution, effectively applying a bootstrap approach for statistical variance estimation.

The least squares cost function minimizes the sum of squared residuals of C_L or C_l. The parameters to be estimated include the separation parameters (τ_1, τ_2, a_1, α^*) and the aerodynamic derivatives (C_{L_0}, C_{L_α}, $C_{L_{\alpha 2}}$). The cost function is optimized using the MATLAB function fmincon[1], which supports the minimization of constrained multi-variable functions. However, after this initial estimation, an ordinary least squares (OLS) method is applied to re-estimate the aerodynamic coefficients. This secondary step is necessary because the non-linear estimation fails to yield satisfactory results. While the outcomes of both approaches are correlated, the non-linear estimation routine exhibits noticeable deficiencies, as illustrated in Fig. 8.1.

A significant bottleneck is the runtime of the optimization process, which typically takes an entire day per iteration. This long runtime severely limits the pace of innovation for refining model structures. Furthermore, independently minimizing each maneuver's cost function does not yield a global minimum across the entire dataset. A more effective approach would involve optimizing the cost function across all maneuvers simultaneously, necessitating the development of a covariance matrix computation method. Lastly, the inability of the non-linear estimation to achieve an optimal solution for the aerodynamic coefficients raises concerns about the reliability of the separation parameter estimates. In summary, the methodology faces three primary limitations:

- **Extended runtime**, impeding the rapid iteration of model structures.
- **No covariance matrix**, forcing separate identification for each maneuver.

[1] `https://nl.mathworks.com/help/optim/ug/fmincon.html`

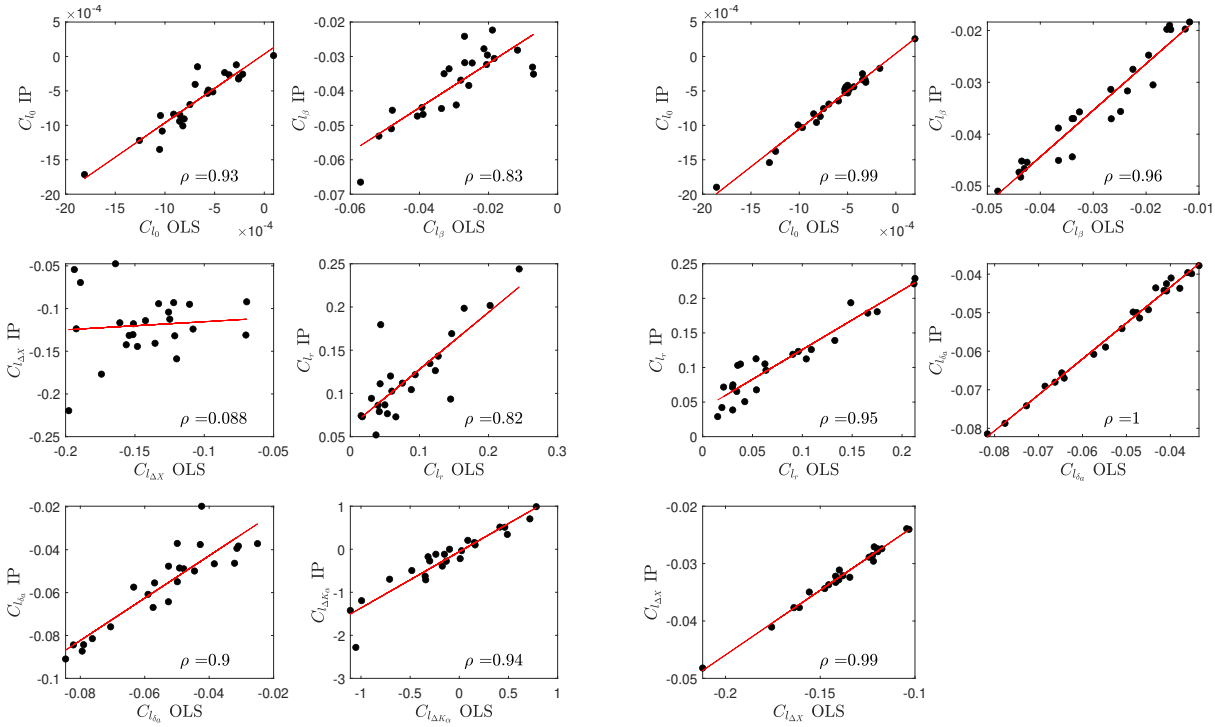

Figure 8.1: Relationship between aerodynamic coefficients estimated via the non-linear routine and the subsequent ordinary least squares estimation. Adapted from [29]

- **Suboptimal aerodynamic coefficient estimates**, which bring into question the validity of the separation parameters.

Using these limitations, some early research into alternative methods led to separable non-linear least squares. SNLS guarantees an optimum value for the aerodynamic coefficients as it internalizes an OLS method for the linear parameters [42]. This directly solves the third limitation. Furthermore, SNLS reduces the dimension of the non-linear parameter estimation problem, which should decrease the computational load [41]. Lastly, covariance matrix estimates have been defined for SNLS [44].

8.2. Implementation

As SNLS is a nonlinear least squares method, it is chosen to use the MATLAB method lsqnonlin[2]. For this method, it is necessary to define an objective function that returns a vector of residuals as its first output. More details on the calculation of the residuals are given in Subsection 8.2.1. The second output of the objective function must be the residual sensitivity matrix. This matrix provides the gradient of the residuals with respect to the parameters, the calculation of this matrix is elaborated on in Subsection 8.2.2. A boilerplate code for the function is given in Listing 8.1.

Listing 8.1: General objective function for lsqnonlin Matlab function

```
function [r,J] = objective(p)
    % [r,J] = objective(p) Returns the residuals and objective gradient
    %
    % p = [k x 1] column vector of nonlinear parameters
    %
    % r = [m x 1] column vector of residuals
    % J = [m x k] sensitivity matrix of the residuals with respect to the
        parameters
     ...
```

[2] https://nl.mathworks.com/help/optim/ug/lsqnonlin.html

```
9 end
```

8.2.1. Objective

As explained before, the objective for SNLS is to minimize the squared residuals. In the case of stall model identification, the residuals can be defined as the difference between a measured aerodynamic coefficient and the predicted aerodynamic coefficient. To keep it general, in this work all equations refer to C_X. The residuals can be defined as:

$$\boldsymbol{r} = \boldsymbol{C_X} - \hat{\boldsymbol{C}}_{\boldsymbol{X}} \tag{8.1}$$

where $\boldsymbol{C_X} \in \mathbb{R}^m$ is the measured aerodynamic coefficient and $\hat{\boldsymbol{C}}_{\boldsymbol{X}} \in \mathbb{R}^m$ is the estimated aerodynamic coefficient. Furthermore, the estimated model can be defined as:

$$\hat{C}_X = \begin{bmatrix} \Phi_1 & \cdots & \Phi_n \end{bmatrix} \cdot \boldsymbol{c} = \boldsymbol{\Phi} \cdot \boldsymbol{c} \tag{8.2}$$

where Φ_i are the regressors and $\boldsymbol{c}$ is a column vector with the aerodynamic derivatives. The aerodynamic coefficients, the linear parameters in the context of SNLS, can be estimated using OLS.

$$\hat{\boldsymbol{c}} = \boldsymbol{\Phi}^+ \cdot \boldsymbol{C_X} \tag{8.3}$$

Note that the order of operations becomes important. This is due to the matrix multiplication of $\boldsymbol{\Phi}$ and $\boldsymbol{\Phi}^+$. A naive implementation results in the formation of that multiplication directly, which leads to a matrix in $\mathbb{R}^{(m \times m)}$. For large problems, this matrix explodes and RAM storage will run out. A quick calculation shows, assuming 16 GB of RAM and the standard double number format in MATLAB, this matrix will run out of storage at $m = 44721$. The dataset, used in previous work, contained 243055 observations, which exceeds what is possible with this naive implementation. Luckily, a simple solution exists. By changing the order of operations, the maximum matrix size becomes $(m \times n)$ and considering $n << m$, the storage problem is solved.

$$\boldsymbol{r} = \boldsymbol{C_X} - \boldsymbol{\Phi} \cdot \boldsymbol{\Phi}^+ \boldsymbol{C_X} = \boldsymbol{C_X} - \boldsymbol{\Phi} \cdot (\boldsymbol{\Phi}^+ \cdot \boldsymbol{C_X}) \tag{8.4}$$

8.2.2. Objective Gradient

The objective gradient is defined using the formulation given by Golub and Pereyra [42]. This formula as defined in Subsection 2.5.2, is restated here:

$$\boldsymbol{D r_2}(\boldsymbol{\theta}) = \boldsymbol{D P^{\perp}_{\Phi(\alpha)} y} = -(\boldsymbol{P^{\perp}_{\Phi} D \Phi}) \boldsymbol{\Phi}^+ \boldsymbol{y} - (\boldsymbol{\Phi}^+)^\top (\boldsymbol{P^{\perp}_{\Phi} D \Phi})^\top \boldsymbol{y} \tag{2.40}$$

$$\mathbf{D}\boldsymbol{r} = -J_1 - J_2 \tag{8.5}$$

Similar to the previous section, a naive calculation leads to $(m \times m)$ storage constraints. However, the equation can be refactored to avoid this. To do this, consider the equation as two parts, J_1 and J_2, these can be refactored independently. Starting with J_1:

$$\begin{aligned}
J_1 &= (\boldsymbol{P^{\perp}_{\Phi}} \cdot \mathbf{D}\boldsymbol{\Phi}) \cdot \boldsymbol{\Phi}^+ \cdot \boldsymbol{Y} \\
J_1 &= (\boldsymbol{P^{\perp}_{\Phi}} \cdot \mathbf{D}\boldsymbol{\Phi}) \cdot \hat{\boldsymbol{c}} && (\hat{\boldsymbol{c}} = \boldsymbol{\Phi}^+ \cdot \boldsymbol{Y}) \\
J_1 &= ((I - \boldsymbol{\Phi} \cdot \boldsymbol{\Phi}^+) \cdot \mathbf{D}\boldsymbol{\Phi}) \cdot \hat{\boldsymbol{c}} && (\boldsymbol{P^{\perp}_{\Phi}} = I - \boldsymbol{\Phi} \cdot \boldsymbol{\Phi}^+) \\
J_1 &= \mathbf{D}\boldsymbol{\Phi} \cdot \hat{\boldsymbol{c}} - \boldsymbol{\Phi} \cdot (\boldsymbol{\Phi}^+ \cdot (\mathbf{D}\boldsymbol{\Phi} \cdot \hat{\boldsymbol{c}})) && \text{(refactor)}
\end{aligned}$$

here, the following steps were taken. First, the product $\boldsymbol{\Phi}^+ \cdot \boldsymbol{Y}$ is reduced to $\hat{c}$. Then, $\boldsymbol{P^{\perp}_{\Phi}}$ is expanded. Lastly, by refactoring the parentheses and order of multiplication the formation of an $(m \times m)$ array is avoided. Moving on to J_2, this refactoring is more complex. It requires multiple double transpositions, expansion of $\boldsymbol{P^{\perp}_{\Phi}}$ and the pseudo-inverse property $(\boldsymbol{\Phi} \cdot \boldsymbol{\Phi}^+) = \boldsymbol{\Phi} \cdot \boldsymbol{\Phi}^+$ [45]. The full derivation follows:

$$
\begin{aligned}
J_2 &= (\mathbf{\Phi}^+)^\top \cdot (\boldsymbol{P}_{\mathbf{\Phi}}^\perp \cdot \mathbf{D\Phi})^\top \cdot \boldsymbol{Y} && \\
J_2 &= (\boldsymbol{Y}^\top \cdot \boldsymbol{P}_{\mathbf{\Phi}}^\perp \cdot \mathbf{D\Phi} \cdot \mathbf{\Phi}^+)^\top && \text{(double transpose)} \\
J_2 &= (\boldsymbol{Y}^\top \cdot (I - \mathbf{\Phi} \cdot \mathbf{\Phi}^+) \cdot \mathbf{D\Phi} \cdot \mathbf{\Phi}^+)^\top && (\boldsymbol{P}_{\mathbf{\Phi}}^\perp = I - \mathbf{\Phi} \cdot \mathbf{\Phi}^+) \\
J_2 &= ((\boldsymbol{Y}^\top - \boldsymbol{Y}^\top \cdot \mathbf{\Phi} \cdot \mathbf{\Phi}^+) \cdot \mathbf{D\Phi} \cdot \mathbf{\Phi}^+)^\top && \text{(refactor)} \\
J_2 &= ((\boldsymbol{Y} - (\mathbf{\Phi} \cdot \mathbf{\Phi}^+)^\top \cdot \boldsymbol{Y})^\top \cdot \mathbf{D\Phi} \cdot \mathbf{\Phi}^+)^\top && \text{(double transpose)} \\
J_2 &= ((\boldsymbol{Y} - \mathbf{\Phi} \cdot \mathbf{\Phi}^+ \cdot \boldsymbol{Y})^\top \cdot \mathbf{D\Phi} \cdot \mathbf{\Phi}^+)^\top && ((\mathbf{\Phi} \cdot \mathbf{\Phi}^+)^\top = \mathbf{\Phi} \cdot \mathbf{\Phi}^+) \\
J_2 &= (\boldsymbol{r}^\top \cdot \mathbf{D\Phi} \cdot \mathbf{\Phi}^+)^\top && (\boldsymbol{r} = \boldsymbol{Y} - \mathbf{\Phi} \cdot \mathbf{\Phi}^+ \cdot \boldsymbol{Y}) \\
J_2 &= (\mathbf{\Phi}^+)^\top \cdot (\mathbf{D\Phi})^\top \cdot \boldsymbol{r} && \text{(refactor transpose)}
\end{aligned}
$$

Using the previous two derivations, the function can be refactored to avoid the formation of large matrices. This results in the following formula:

$$\mathbf{D}\boldsymbol{r} = -\mathbf{D\Phi} \cdot \hat{\boldsymbol{c}} + \mathbf{\Phi} \cdot (\mathbf{\Phi}^+ \cdot (\mathbf{D\Phi} \cdot \hat{\boldsymbol{c}})) - (\mathbf{\Phi}^+)^\top \cdot (\mathbf{D\Phi})^\top \cdot \boldsymbol{r} \tag{8.6}$$

where, the calculation of $\hat{\boldsymbol{c}}$ has been covered in Subsection 8.2.1. The last remaining piece of the puzzle is the Frechet derivative $\mathbf{D\Phi}$. The three-dimensional tensor contains the partial derivatives of the regressors with respect to the nonlinear parameters for each observation. In stall modeling, the nonlinear parameters refer to the separation parameters. An entry of the tensor looks as follows:

$$\boldsymbol{D\Phi} = \frac{\partial \Phi_{ij}}{\partial \theta_k} \tag{8.7}$$

A product rule must be used to define the partial derivative. First, the derivative of the regressor with respect to the separation state X is calculated. Then, the derivative of the separation state with respect to the nonlinear parameters is calculated. Furthermore, depending on the equation, multiple separation states may exist which can be a function of the same parameters. To account for this, a summation is introduced.

$$\frac{\partial \Phi_{ij}}{\partial \theta_k} = \sum_{X=\{X_1,\dots X_2\}} \frac{\partial \Phi_{ij}}{\partial X} \cdot \frac{\partial X}{\partial \theta_k} \tag{8.8}$$

For unsteady separation models, the separation state is a function of a first order differential equation. To find the state sensitivity to the nonlinear equations Van Ingen [23] defined a procedure taken from Leis and Kramer [46].

Lastly, in the setup of the aerodynamic coefficients not each regressor will be a function of the separation states. Consider, for example, the bias term, pitch rate, or elevator deflection. This means that many entries of $\mathbf{D\Phi}$ will be zero. Inspired by O'Leary and Rust [43] a bookkeeping method is implemented to register the dependency of each regressor on the separation states and the derivative is only stored if necessary.

8.2.3. Statistical Properties

To judge the quality of the model, it is important to define metrics with which to measure the quality. Looking at the model parameters five metrics are defined: the parameter covariance matrix, variance, standard deviation, correlation matrix, and t-test. These are further discussed below.

Parameter Covariance Matrix

First and foremost, the parameter covariance matrix can be defined. As mentioned in Subsection 2.5.3, the parameter covariance matrix for SNLS can be defined as:

$$Cov[\boldsymbol{c}, \boldsymbol{\theta}] = \left[\nabla f_m^\top \cdot \nabla f_m\right]^{-1} \left[\nabla f_m^\top \cdot \Lambda_m \cdot \nabla f_m\right] \left[\nabla f_m^\top \cdot \nabla f_m\right]^{-1} \tag{8.9}$$

However, this equation cannot directly be implemented. Λ_m is in $\mathbb{R}^{(m\times m)}$, which becomes too large for storage. However, Λ_m is a Toeplitz matrix built from the auto-correlation series λ_m. The Toeplitz matrix connects to discrete convolution which can be used here. For convolution, efficient algorithms have been implemented in MATLAB. In this case, cconv[3] is used. Note that Λ_m is a full matrix, which means it does not calculate the tails of the convolution and only the central part. This is easily extracted from the results of cconv.

Parameter Variance and Standard Deviation
From the covariance matrix, it is easy to derive the parameter variance. The parameter variance is simply the diagonal of the covariance matrix. Furthermore, the standard deviation can be derived by taking the square root of the variance [47].

$$Var[\theta] = Diag[C_\theta]; \quad \sigma_\theta = \sqrt{Var[\theta]} \tag{8.10}$$

where $Diag$ refers to taking the diagonal elements of a matrix.

Parameter Correlation Matrix
The correlation matrix can be seen as a normalized version of the covariance matrix. It can be calculated by forming a diagonal matrix with the parameter standard deviation and doing a left and right multiplication with the covariance matrix.

$$Cor[\theta] = Diag[1/\sigma_\theta] \cdot Cov[\theta] \cdot Diag[1/\sigma_\theta] \tag{8.11}$$

where $Diag$ refers to a matrix with the diagonal filled with the elements of a vector.

Student's T-test
Using the two-sided t-test it can be determined if a parameter is significantly different from zero [48]. This is done by setting the null hypothesis as the parameter has a value of zero. The alternative hypothesis then naturally becomes that the value cannot be zero.

$$H_0: \quad \theta_i = 0 \tag{8.12}$$
$$H_1: \quad \theta_i \neq 0 \tag{8.13}$$

Using a significance level α, the null hypothesis is rejected if:

$$\frac{\hat{\theta}_i}{\sigma_{\theta_i}/\sqrt{m}} > t_{\alpha/2} \tag{8.14}$$

where $\hat{\theta}_i$ is the estimated parameter value, σ_{θ_i} is the estimated parameter variance, m is the number of observations and $t_{\alpha/2}$ is the point where the tail of the distribution has a remaining probability of $\alpha/2$, for a t-distribution with $m-p$ degrees of freedom. p here is the number of regressors.

8.3. Verification and Validation

In this chapter, multiple steps will be performed to verify the correct implementation of the SNLS method. Important for all steps is a data set with a known model structure. In this way, the results of the SNLS method can be compared to the known values. The model structure chosen for these verification steps is that of the roll moment coefficient of De Fuijk [29]:

$$C_l = C_{l_0} + C_{l_\beta}\beta + C_{l_r}r + C_{l_{\delta_a}}\delta_a + C_{l_{\Delta X}}\Delta X\frac{y_w}{b}, \tag{8.15}$$

$$\tau_1\frac{dX_{l,r}}{dt} + X_{l,r} = \frac{1}{2}\left\{1 - \tanh\left(a_1\left[\alpha_{l,r} - \tau_2\dot{\alpha}_{l,r} - \alpha^*\right]\right)\right\}. \tag{8.16}$$

The inputs used by the tests in this chapter are taken from the *asym* dataset used by De Fuijk [29]. The model parameters are those found by De Fuijk [29].

[3] https://nl.mathworks.com/help/signal/ref/cconv.html

Table 8.1: Comparison of the true model parameters and those estimated by the SNLS method

Parameter	θ	$\hat{\theta}$
τ_1	0.0971	0.0971
τ_2	0.5526	0.5526
a_1	16.865	16.865
α^*	0.1730	0.1730
C_{l_0}	−0.0006	−0.0006
C_{l_β}	−0.0279	−0.0279
C_{l_r}	0.0661	0.0661
$C_{l_{\delta_r}}$	−0.0501	−0.0501
$C_{l_{\Delta X}}$	−0.1274	−0.1274

8.3.1. Convergence

As a first verification step, it is tested if the SNLS method can find the parameter values of a known model. The model can be visualized as in the top part of Fig. 8.2, where $\alpha_{l,r}, \dot{\alpha}_{l,r}, \beta, r$ and δ_a are the inputs to the model, θ_X and θ_l are the model parameters and C_l is the model output. The blocks C_l-model and X-model refer to Eq. (8.15) and Eq. (8.16) respectively. Next, the input and output of the model can be used by the SNLS method to estimate the model parameters, this is visualized in the bottom of Fig. 8.2, where $\hat{\theta}_X$ and $\hat{\theta}_l$ are the model parameter estimates.

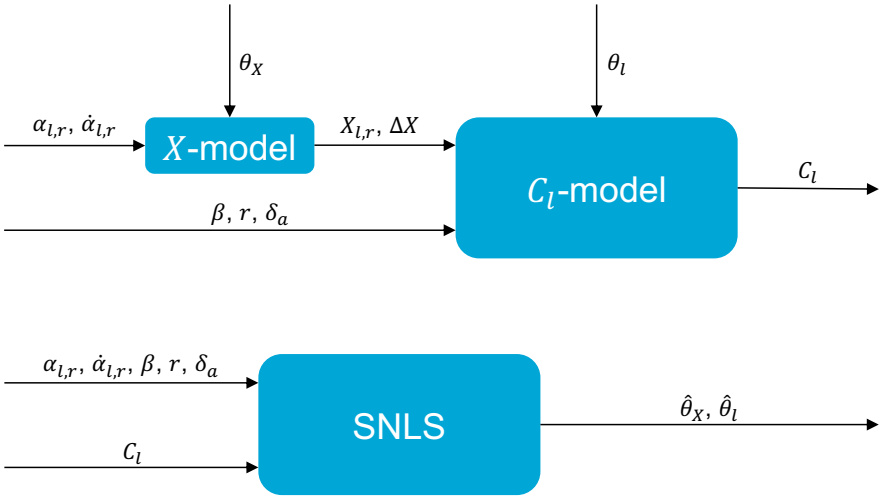

Figure 8.2: Workflow for the verification of convergence for the SNLS method

Applying the described workflow creates a set of parameter estimates. These estimates can be directly compared to the true parameters. The result of this verification step is summarized in Table 8.1. It can be seen that the SNLS method successfully finds the true parameter values.

8.3.2. Monte-Carlo Simulation

A Monte-Carlo simulation is performed to verify the correct implementation of the covariance matrix by Mahata and Söderström [44], which has been restated in Eq. (8.17) for ease of reference.

$$C_{\boldsymbol{\theta}} = \left[\nabla f_m^\top \cdot \nabla f_m\right]^{-1} \left[\nabla f_m^\top \cdot \Lambda_m \cdot \nabla f_m\right] \left[\nabla f_m^\top \cdot \nabla f_m\right]^{-1}, \tag{8.17}$$

For Monte Carlo simulation, white Gaussian noise is added to C_l before it is used as input to the SNLS method, as can be seen in Fig. 8.3. This noise emulates the residual noise when the parameters are

Table 8.2: Results of the Monte Carlo simulation

	SNLS		Monte-Carlo	
Parameter	$\hat{\theta}$	$\sigma_{\hat{\theta}}$	$\mu_{\hat{\theta}}$	$\sigma_{\hat{\theta}}$
τ_1	9.17×10^{-2}	8.74×10^{-3}	9.72×10^{-2}	8.66×10^{-3}
τ_2	5.42×10^{-1}	3.16×10^{-2}	5.53×10^{-1}	3.15×10^{-2}
a_1	1.66×10^{1}	9.91×10^{-1}	1.69×10^{1}	9.70×10^{-1}
α^*	1.72×10^{-1}	1.89×10^{-3}	1.73×10^{-1}	1.83×10^{-3}
C_{l_0}	-5.66×10^{-4}	3.45×10^{-5}	-5.93×10^{-4}	5.15×10^{-5}
C_{l_β}	-3.13×10^{-2}	1.77×10^{-3}	-2.79×10^{-2}	1.72×10^{-3}
C_{l_r}	6.87×10^{-2}	8.17×10^{-3}	6.63×10^{-2}	9.27×10^{-3}
$C_{l_{\delta_r}}$	-5.15×10^{-2}	1.43×10^{-3}	-5.01×10^{-2}	1.70×10^{-3}
$C_{l_{\Delta X}}$	-1.27×10^{-1}	3.34×10^{-2}	-1.28×10^{-1}	5.29×10^{-3}

identified using real data. The magnitude of the noise was calculated using the residuals of the model identification performed by De Fuijk [29] and equal to -36 dB. For each noise realization, the parameters were estimated and stored. The resulting collection of parameter estimates has a distribution of which the mean and standard deviation can be calculated. The calculated standard deviations are compared with those calculated from the covariance matrix.

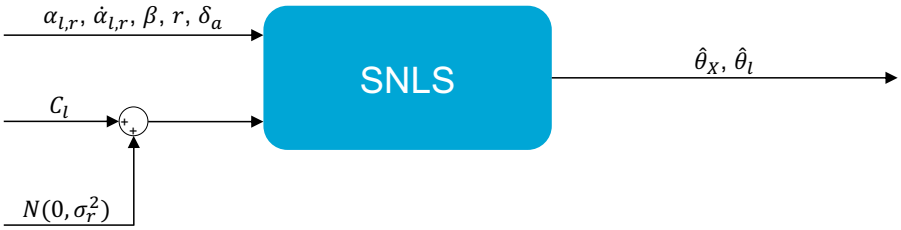

Figure 8.3: Injection of noise on the input of the SNLS method.

The final results of this verification step are presented in Table 8.2. The SNLS column presents statistics for one estimate, including noise. It can be seen that the introduced noise affects the parameter estimates, which start to deviate from their value. Looking at the standard deviation estimates, which are determined by taking the square root of the diagonal of the covariance matrix C_θ, it can be seen that they align well with those estimated using the Monte Carlo method. As the covariance matrix is based on asymptotic assumptions, the true variance cannot be achieved. Similarly, the Monte Carlo method is statistical and does not produce the true variance. For this reason, the results are considered an acceptable verification step.

9

Initial Results

In this chapter, initial research is shown for the creation of a new stall model. It is not the final result of this paper, refer to Part II for this. However, it can serve as a tool to understand how an iteration of the model can be initiated, what steps are required, and on what grounds a model might be accepted as an improvement.

9.1. Lift Coefficient

The optimization of the X-parameters in the work by Van Ingen [23] was done through the lift coefficient model. To compare the SNLS method to previous optimizers, it is chosen to compare to this result. The model identified by Van Ingen [23] has the structure of *Model I* in Eq. (9.1).

$$\begin{aligned} \textit{Model I}: \quad C_L &= C_{L_0} + C_{L_{K_\alpha}} \left(\frac{1+\sqrt{X}}{2} \right)^2 \alpha + C_{L_{\alpha^2_{+6}}} (\alpha - 6^\circ)^2_+ \\ \tau_1 \frac{dX}{dt} + X &= \frac{1}{2} \left\{ 1 - \tanh \left(a_1 \left[\alpha - \tau_2 \dot{\alpha} - \alpha^* \right] \right) \right\} \end{aligned} \tag{9.1}$$

where the second term is the standard Kirchhoff term and the third term is a squared spline function that starts at angles higher or equal to six degrees. The last term was introduced to improve the behavior at high angles of attack. The parameter values of the *Van Ingen* are summarized in Table 9.3. The model quality metrics mean square error (MSE) and R-square values are presented in Table 9.5.

Using the SNLS method, *Model I* is reidentified. Interestingly, the results differ significantly from those found in earlier work. This is probably attributed to the previous method of optimizing per stall and averaging the values. Identification per stall creates the risk of insufficient data content to find the true parameters. Furthermore, the averaging method implicitly assumes that the confidence in each parameter estimate is equal, which might not be the case. The SNLS method solves both issues by directly identifying the parameters of the entire training set.

Furthermore, looking at Table 9.5, it can be seen that the SNLS method reduces the MSE of the training data and improves the consistency of the R-square values between sets. This comes at the cost of some performance in the MSE of the validation data. The consistency of the R-square values is transferred to the validation data.

Due to the significant changes in parameter values, the addition of the spline function is revisited. The spline term has no physical meaning and should if possible be removed. This leads to the formation of *Model II*.

$$\begin{aligned} \textit{Model II}: \quad C_L &= C_{L_0} + C_{L_{K_\alpha}} \left(\frac{1+\sqrt{X}}{2} \right)^2 \alpha \\ \tau_1 \frac{dX}{dt} + X &= \frac{1}{2} \left\{ 1 - \tanh \left(a_1 \left[\alpha - \tau_2 \dot{\alpha} - \alpha^* \right] \right) \right\} \end{aligned} \tag{9.2}$$

The results of *Model II* parameter estimation using SNLS is presented in Tables 9.3 and 9.5. It can be seen that *Model II* performs almost as well as *Model I*. The marginal differences between the models and the improved phenomenological explanation make *Model II* more desirable.

Looking at the results of *Van Ingen*, *Model I* and *Model II*, it can be seen that all parameter estimations give very different τ_1 and τ_2 values. A likely explanation for this is the existence of a high correlation between the two. For *Model II*, the parameter correlations are presented in Table 9.1. As expected, the correlation between τ_1 and τ_2 is found to be large. This finding is also supported by the literature. Fischenberg [15] describes that quasi-steady stall approaches, which were flown with the Citation II, cannot identify τ_1 without correlation. To identify the effects of τ_1, dynamic stall approaches must be flown as described by Fischenberg and Jategaonkar [18]. This requires more flight test data. For now, an alternative model structure is proposed, which is called *Model III*.

Table 9.1: Parameter correlation matrix for *Model II*

	τ_1	τ_2	a_1	α^*	C_{L_0}	$C_{L_{K_\alpha}}$
τ_1	1	−0.8889	0.3759	−0.4418	−0.4207	0.4299
τ_2	−0.8889	1	−0.3347	0.5921	0.1840	−0.1925
a_1	0.3759	−0.3347	1	0.3292	0.0411	−0.0180
α^*	−0.4418	0.5921	0.3292	1	0.1505	−0.1430
C_{L_0}	−0.4207	0.1840	0.0411	0.1505	1	−1.0003
$C_{L_{K_\alpha}}$	0.4299	−0.1925	−0.0180	−0.1430	−1.0003	1

$$\textit{Model III}: \quad C_L = C_{L_0} + C_{L_{K_\alpha}} \left(\frac{1+\sqrt{X}}{2} \right)^2 \alpha \tag{9.3}$$
$$X = \frac{1}{2}\left\{1 - \tanh\left(a_1\left[\alpha - \tau_2\dot{\alpha} - \alpha^*\right]\right)\right\}$$

Model III is a quasi-steady stall model. The results of parameter estimation using SNLS is presented in Tables 9.3 and 9.5. It can be seen that the performance of the model is not significantly degraded. This confirms that the stalls performed are quasi-steady, as a quasi-steady model can capture them.

Using model term selection procedures developed previously in the stall task force, it is identified that the pitch rate has a positive effect on the model fit. For this reason *Model IV* is created.

$$\textit{Model IV}: \quad C_L = C_{L_0} + C_{L_{K_\alpha}} \left(\frac{1+\sqrt{X}}{2} \right)^2 \alpha + C_{L_q} q^* \tag{9.4}$$
$$X = \frac{1}{2}\left\{1 - \tanh\left(a_1\left[\alpha - \tau_2\dot{\alpha} - \alpha^*\right]\right)\right\}$$

where the extra term dependent on the reduced pitch rate is introduced. The results are presented in Tables 9.3 and 9.5. Small gains are seen in the MSE of the training data and for the validation data the improvement is more significant. In terms of the parameter values, it can be seen that the value of τ_2 is significantly altered. The explanation lies in the added term. Judging from the correlation matrix in Table 9.2, τ_2 and C_{L_q} are correlated. This is not surprising, as these terms scale $\dot{\alpha}$ and q respectively. The correlation between these terms is a well-documented problem in aircraft system identification, and special maneuvers have been designed to separate them [49, 50, 51]. Again, different data are required to identify the effects of the pitch rate.

Next, an analysis of the contribution of the elevator deflection on the lift is performed. The previous results of Van Ingen [23] did not find any contribution. This contradicts the findings made previously in nominal flight by Van Den Hoek [52]. In addition, other researchers have found that the elevator affects the

Table 9.2: Parameter correlation matrix for *Model IV*

	τ_2	a_1	α^*	C_{L_0}	$C_{L_{K_\alpha}}$	C_{L_q}
τ_2	1	−0.3691	−0.3836	0.3168	−0.3440	0.7850
a_1	−0.3691	1	0.6294	0.0405	−0.0143	−0.3171
α^*	−0.3836	0.6294	1	−0.1189	0.1289	−0.3508
C_{L_0}	0.3168	0.0405	−0.1189	1	−0.9998	0.4898
$C_{L_{K_\alpha}}$	−0.3440	−0.0143	0.1289	−0.9998	1	−0.5216
C_{L_q}	0.7850	−0.3171	−0.3508	0.4898	−0.5216	1

lift coefficient during stall [15, 21]. To gain more insight, the power spectrum of the elevator sensor signal is plotted in Fig. 9.1. From this plot, it can be seen that the deflection of the elevator must be relatively constant, judging by the power at 0 Hz. The further signal power seems to be spread mainly between 0 and 3 Hz and a small peak at 4 Hz. In previous work by Van Ingen [23] a filter with a cutoff frequency of 4 Hz was used, which captures most of the power in the signal. However, for the accelerations, which are used to determine the lift coefficient, a cutoff frequency of 1.5 Hz is used. This means that the influence of the elevator might have been filtered out before the system identification. There are two solutions to these problems. Either, slower maneuvers must be performed, for example, a 3211 or doublet instead of the wiggle used as an input to the elevator. Alternatively, the flight path reconstruction has to be redone, using accelerations filtered with a cutoff frequency of 4 Hz instead of 1.5 Hz.

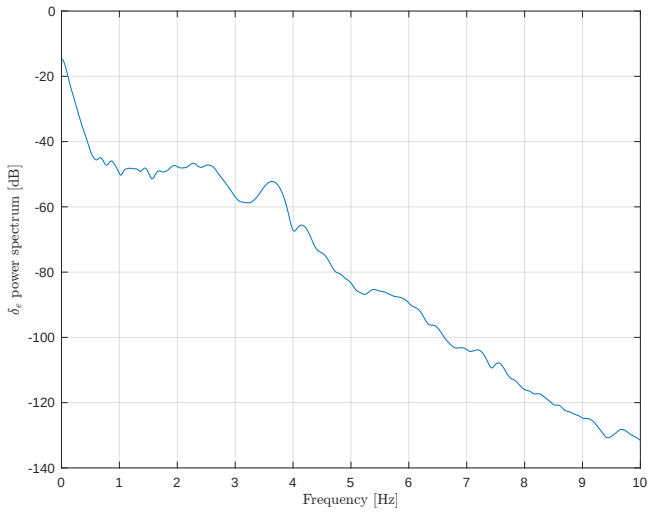

Figure 9.1: Power spectrum of the elevator deflection signal for *Van Ingen* dataset

During a walk-around of the aircraft, a relatively small detail on the wing was noticed. However, the implications on the stall model could be large. On part of the leading edge, stall strips are installed. These strips are used to control the behavior of the stall of the aircraft. They make sure stall is not initiated at the wing tips, where control effectiveness might be compromised. Similarly, stall at the root is prevented, where stall wake could cause adverse effects on the engine. The previous stall models assumed a uniform stall over the wing. The local effects of a stall strip cannot be modeled. The early stall around the stall strips also provides a possible explanation for the low a_1 values that are found. Due to averaging of the flow condition over the whole wing, the local stall can be perceived as a soft stall. To improve the model the effect of the stall strip will be separated. An initial assumption is that the stall takes place only at the stall strip. This leads to *Model V*, which is defined as follows:

$$\textit{Model V}: \quad C_L = C_{L_0} + C_{L_\alpha}\alpha + C_{L_{K_\alpha}} \left(\frac{1+\sqrt{X}}{2}\right)^2 \alpha \tag{9.5}$$
$$X = \frac{1}{2}\left\{1 - \tanh\left(a_1\left[\alpha - \tau_2\dot{\alpha} - \alpha^*\right]\right)\right\}$$

Excluding the bias, the first term accounts for the nonstalled regions, which should behave linearly. The last term is the familiar Kirchhoff term, which accounts for the stalled region of the wing. The results of the model identification using SNLS can be found in Tables 9.3 and 9.5. It can be seen that *Model V* provides a good improvement in MSE, for training and validation data, compared to *Model II*. However, the assumption that no stall takes place outside the stall strips might not be valid. To account for stall outside of the region of the stall strips *Model VI* is created, which looks like this:

$$\textit{Model VI}: \quad C_L = C_{L_0} + C_{L_{K_{\alpha,1}}} \left(\frac{1+\sqrt{X_1}}{2}\right)^2 \alpha + C_{L_{K_{\alpha,2}}} \left(\frac{1+\sqrt{X_2}}{2}\right)^2 \alpha \tag{9.6}$$
$$X_1 = \frac{1}{2}\left\{1 - \tanh\left(a_{11}\left[\alpha - \tau_{21}\dot{\alpha} - \alpha_1^*\right]\right)\right\}$$
$$X_2 = \frac{1}{2}\left\{1 - \tanh\left(a_{12}\left[\alpha - \tau_{22}\dot{\alpha} - \alpha_2^*\right]\right)\right\}$$

Table 9.3: Comparison of parameter estimates for different lift coefficient models

	Van Ingen [23]		*Model I*		*Model II*	
Parameter	$\hat{\theta}$	$\sigma_{\hat{\theta}}$	$\hat{\theta}$	$\sigma_{\hat{\theta}}$	$\hat{\theta}$	$\sigma_{\hat{\theta}}$
τ_1	0.2547	0.1565	0.1554	0.0239	0.0101	0.0202
τ_2	0.0176	0.0819	0.1191	0.0214	0.3354	0.0273
a_1	27.6711	6.7177	15.0111	0.6546	8.7520	0.2765
α^*	0.2084	0.0202	0.2175	0.0019	0.2350	0.0043
C_{L_0}	0.1758	0.0423	0.1274	0.0089	0.1003	0.0088
$C_{L_{K_\alpha}}$	4.6605	0.3965	5.1891	0.0735	5.6523	0.0739
$C_{L_{\alpha^2_{+6}}}$	10.7753	3.8895	5.9746	0.2502	N/A	N/A
C_{L_q}	N/A	N/A	N/A	N/A	N/A	N/A

	Model III		*Model IV*		*Model V*	
Parameter	$\hat{\theta}$	$\sigma_{\hat{\theta}}$	$\hat{\theta}$	$\sigma_{\hat{\theta}}$	$\hat{\theta}$	$\sigma_{\hat{\theta}}$
τ_1	N/A	N/A	N/A	N/A	N/A	N/A
τ_2	0.3619	0.0130	0.2305	0.0302	0.4014	0.0116
a_1	8.9897	0.2614	9.1486	0.2997	20.6430	1.0909
α^*	0.2376	0.0038	0.2433	0.0046	0.2135	0.0016
C_{L_0}	0.1065	0.0088	0.1242	0.0085	0.1438	0.0083
$C_{L_{K_\alpha}}$	5.5633	0.0738	5.3360	0.0720	2.9556	0.0672
$C_{L_{\alpha^2_{+6}}}$	N/A	N/A	N/A	N/A	N/A	N/A
C_{L_q}	N/A	N/A	11.4130	1.3010	N/A	N/A
C_{L_α}	N/A	N/A	N/A	N/A	2.0013	0.0443

Table 9.4: Parameter estimates for a lift model with two quasi-steady separation states

	Model VI	
Parameter	$\hat{\theta}$	$\sigma_{\hat{\theta}}$
τ_{21}	0.4462	0.0126
a_{11}	39.3620	3.2210
α_1^*	0.1989	0.0012
τ_{22}	0.1742	0.0145
a_{12}	14.3940	1.2824
α_2^*	0.3385	0.0046
C_{L_0}	0.1578	0.0078
$C_{L_{K_{\alpha,1}}}$	1.7218	0.0482
$C_{L_{K_{\alpha,2}}}$	3.0739	0.0435

Table 9.5: Comparison of lift coefficient models

	Training data (27 sets)				**Validation data** (7 sets)			
Model	MSE	R^2	min(R^2)	max(R^2)	MSE	R^2	min(R^2)	max(R^2)
Van Ingen	1.65×10^{-3}	0.92	0.71	0.98	1.45×10^{-3}	0.91	0.77	0.96
Model I	1.39×10^{-3}	0.93	0.85	0.98	1.52×10^{-3}	0.91	0.85	0.97
Model II	1.44×10^{-3}	0.93	0.84	0.98	1.63×10^{-3}	0.91	0.84	0.96
Model III	1.46×10^{-3}	0.93	0.82	0.98	1.72×10^{-3}	0.90	0.83	0.96
Model IV	1.42×10^{-3}	0.93	0.80	0.98	1.54×10^{-3}	0.91	0.84	0.97
Model V	1.34×10^{-3}	0.93	0.83	0.98	1.46×10^{-3}	0.92	0.86	0.96
Model VI	1.23×10^{-3}	0.94	0.84	0.98	1.42×10^{-3}	0.92	0.85	0.96

9.2. Normal Force Coefficient

The normal force coefficient C_Z is defined in the body reference frame and points downwards. This coefficient is an alternative to the lift coefficient in modeling aircraft motion. For nominal stall models, this coefficient is used [52, 53].

10

Flight Test Design and Identification Set Synthesis

During the research, deficiencies in the data were observed as part of RQ 5. These deficiencies relate to high correlations between unsteady terms in the stall model and high correlations between the pitch rate and angle of attack rate. This chapter presents maneuvers designed to overcome these deficiencies. The maneuvers are presented in Section 10.1. Two flights were performed during the research, in which the designed maneuvers were executed. Section 10.2 performs a reflection on the flights.

10.1. Maneuver Design

To accomplish the goals set, five maneuvers have been designed for the Citation. This section discusses these maneuvers. First, the maneuvers to differentiate unsteady effects are discussed in Subsection 10.1.1. Then, a discussion on the design of maneuvers for pitch rate and angle of attack rate effects follows in Subsection 10.1.2.

10.1.1. Unsteady Stall Effects

During previous flight tests, stall maneuvers were conducted as follows: the aircraft was first trimmed for level flight, and then its airspeed was gradually reduced at a rate of 1 kts/s until stall occurred. This approach is referred to as a quasi-steady stall maneuver, as both airspeed and angle of attack vary slowly throughout the maneuver. However, Fischenberg [15] identified that such maneuvers are insufficient to distinguish between the effects of the parameters τ_1 and τ_2.

To address this limitation, dynamic stall maneuvers were suggested for identifying τ_1 effects. Singh and Jategaonkar [16] describe a procedure for dynamic stall, which served as the baseline for designing a maneuver for the Citation aircraft. This maneuver begins with an angle of attack between 10° and 12°. The angle of attack is then gradually increased while sequential doublet inputs are applied to the control surfaces. Upon reaching buffet onset, oscillating elevator inputs are used to repeatedly drive the aircraft into and out of stall. This process induces repeated flow separation and reattachment over the wing, providing valuable data for identifying flow separation parameters.

For the Citation, this maneuver required several adaptations. Firstly, the initial angle of attack was lowered to 3° to 5°, as the Citation begins buffeting at angles of attack between 10° and 12°. Secondly, the doublet inputs were replaced with step inputs, providing pilots with greater control during the maneuver. As in the original procedure, oscillating elevator inputs are introduced upon reaching buffet onset to induce stall entry and recovery. This maneuver will be referred to as the **Dynamic Stall**.

Dynamic Stall

1. Establish trimmed level flight
2. Smoothly increase angle of attack
3. Apply sequential elevator/aileron/rudder steps
4. When at stall boundary, apply oscillating elevator inputs
5. Repeat entry into stall until altitude or attitude require recovery
6. Recover

However, this approach does not capture the full dynamics of the stall, as the Citation's stall behavior is influenced by its stall strip. To investigate stall effects across the entire wing, an alternative maneuver was developed. This modified maneuver begins in the same manner as the adapted dynamic stall maneuver. Once buffet is reached, however, the aircraft is held in the stall, allowing the angle of attack to increase while remaining stalled. At approximately $20°$ angle of attack, oscillating elevator inputs are applied to induce flow separation and reattachment across the rest of the wing. This provides additional data to better understand stall characteristics over the entire wing surface. This maneuver will be referred to as a **Deep Dynamic Stall**

Deep Dynamic Stall

1. Establish trimmed level flight
2. Smoothly increase angle of attack
3. Apply sequential elevator/aileron/rudder steps
4. Hold stall with increasing angle of attack
5. Give oscillating elevator inputs around $20°$ angle of attack
6. Recover

10.1.2. Pitch Rate versus Angle of Attack Rate

A second objective for the flight tests is to better differentiate between the effects of pitch rate and angle of attack rate. These two terms are typically highly correlated. The relation between the two can be written as:

$$\dot{\alpha} = q - \frac{\bar{q}S}{mV\cos\beta}C_L + \frac{g(\cos\alpha\cos\phi\cos\theta + \sin\alpha\sin\theta)}{V\cos\beta} - \tan\beta(p\cos\alpha + r\sin\alpha) - \frac{X_T\sin\alpha}{mV\cos\beta} \quad (10.1)$$

There exists a direct relationship between the two terms and in general conditions, the later terms have minor contributions causing them to be highly correlated. Using this equation, however, maneuvers can be designed to differentiate the two. This is exactly what Grauer, Morelli, and Murri [50] have done. The **Pushover** and **Pullup** maneuvers have both been designed by them.

Pushover

1. Establish trimmed level flight
2. Pitch up to +25° pitch attitude
3. Release the elevator to pitch down and use the elevator to maintain a constant angle of attack
4. Recover when pitch attitude reaches -20°

Pullup

1. Establish trimmed level flight
2. Pitch up to -10° pitch attitude
3. Release the elevator to pitch up and use the elevator to maintain a constant angle of attack
4. Recover when pitch attitude reaches 30°

Furthermore, through conversations with the test pilots, an alternative idea was formed. The phugoid is also characterized by a relatively constant angle of attack with a varying pitch angle. This maneuver should theoretically also differentiate the two terms.

Phugoid

1. Establish trimmed level flight
2. Establish off-trim airspeed
3. Release the elevator
4. Recover after 3 periods

10.2. Test Flight Reflection

On the 14th and 23rd of October, two flight tests were performed. During the first test seven dynamic stalls, five pullup, three pushover, and three phugoid maneuvers were performed. During the second flight five dynamic stalls, seven deep dynamic stalls, and five pullup maneuvers were performed. To reflect on the goals these maneuvers are meant to achieve this section performs an analysis on the new flight data. First, the effect of the dynamic stalls is explored in Subsection 10.2.1. Then, a reflection on the maneuvers to identify angle of attack rate effects is performed in Subsection 10.2.2.

10.2.1. Unsteady Stall Effects

To show the impact of the dynamic stalls mentioned in Subsection 10.1.1, two identification exercises are performed. For both, the following model is used:

$$C_L = C_{L_0} + C_{L_{\alpha,ss}} \left(\frac{1+\sqrt{X_{ss}}}{2} \right)^2 \alpha + C_{L_{\alpha,w}} \left(\frac{1+\sqrt{X_w}}{2} \right)^2 \alpha + C_{L_{q^*}} \frac{q\bar{c}}{V} + C_{L_{\delta_e}} \delta_e \tag{10.2}$$

where X_{ss} is governed by an unsteady stall model and X_w is governed by a steady stall model. Two different datasets are used. First, the dataset defined in the work of [23] is used. The second set uses the previous as a basis but adds on the dynamic stall maneuvers performed during the flight test on the 23rd of November. The parameters are identified using the new SNLS method and are presented in Table 10.1. Interestingly, for the *Van Ingen* dataset there is no significant contribution from the elevator deflection.

For both datasets, a parameter correlation matrix can be constructed. The results of this are presented in Tables 10.2 and 10.3. The most notable correlations for the *Van Ingen* dataset are between $\tau_{1,ss}$ and $\tau_{2,ss}$, between $\tau_{1,ss}$ and $C_{L_{q^*}}$, and between C_{L_0} and $C_{L_{\alpha,ss}}$. Table 10.3 shows that including dynamic stall maneuvers successfully reduces the first two correlations. However, large correlations still exist between C_{L_0} and $C_{L_{\alpha,ss}}$.

Table 10.1: Comparison of the identification results with and without dynamic stall maneuvers. For the t-test $\circ$ indicates that the null hypothesis is accepted and $*$ that the null hypothesis is rejected.

	Van Ingen + Dynamic stalls				*Van Ingen*			
	Results		t**-test**		**Results**		t**-test**	
Parameter	$\hat{\theta}$	σ_θ	p	h	$\hat{\theta}$	σ_θ	p	h
$\tau_{1,ss}$	**0.4191**	0.0722	0.0000	*	**0.3246**	0.0509	0.0000	*
$\tau_{2,ss}$	**0.3391**	0.0346	0.0000	*	**0.6105**	0.0391	0.0000	*
$a_{1,ss}$	**70.2846**	11.2205	0.0000	*	**49.1520**	5.9537	0.0000	*
α^*_{ss}	**0.1956**	0.0017	0.0000	*	**0.2017**	0.0014	0.0000	*
$a_{1,w}$	**13.9276**	1.4462	0.0000	*	**10.9279**	1.4962	0.0000	*
α^*_w	**0.3267**	0.0056	0.0000	*	**0.3437**	0.0072	0.0000	*
C_{L_0}	**0.2318**	0.0116	0.0000	*	**0.1584**	0.0075	0.0000	*
$C_{L_{\alpha,ss}}$	**1.3851**	0.1061	0.0000	*	**1.7115**	0.0711	0.0000	*
$C_{L_{\alpha,w}}$	**2.5961**	0.0536	0.0000	*	**2.8433**	0.0513	0.0000	*
$C_{L_{q^*}}$	**8.0747**	1.3881	0.0000	*	**8.7946**	1.3948	0.0000	*
$C_{L_{\delta_e}}$	**−0.3403**	0.0681	0.0000	*	**−0.0845**	0.0596	0.1561	$\circ$

Table 10.2: Parameter correlation matrix for identification using *Van Ingen* dataset

	$\tau_{1,ss}$	$\tau_{2,ss}$	$a_{1,ss}$	α^*_{ss}	$a_{1,w}$	α^*_w	C_{L_0}	$C_{L_{\alpha,ss}}$	$C_{L_{\alpha,w}}$	$C_{L_{q^*}}$	$C_{L_{\delta_e}}$
$\tau_{1,ss}$	1.00	0.73	0.59	-0.17	0.08	-0.25	-0.27	0.15	0.19	-0.67	0.09
$\tau_{2,ss}$	0.73	1.00	0.37	-0.44	0.06	-0.40	-0.16	-0.06	0.36	-0.37	0.11
$a_{1,ss}$	0.59	0.37	1.00	0.15	-0.11	-0.11	-0.12	0.21	-0.16	-0.40	-0.02
α^*_{ss}	-0.17	-0.44	0.15	1.00	-0.06	0.21	-0.03	0.23	-0.40	0.00	-0.20
$a_{1,w}$	0.08	0.06	-0.11	-0.06	1.00	0.61	0.05	-0.12	0.22	0.23	0.13
α^*_w	-0.25	-0.40	-0.11	0.21	0.61	1.00	0.14	-0.03	-0.12	0.35	0.01
C_{L_0}	-0.27	-0.16	-0.12	-0.03	0.05	0.14	1.00	-0.80	-0.14	0.58	-0.08
$C_{L_{\alpha,ss}}$	0.15	-0.06	0.21	0.23	-0.12	-0.03	-0.80	1.00	-0.38	-0.59	0.07
$C_{L_{\alpha,w}}$	0.19	0.36	-0.16	-0.40	0.22	-0.12	-0.14	-0.38	1.00	0.13	0.56
$C_{L_{q^*}}$	-0.67	-0.37	-0.40	0.00	0.23	0.35	0.58	-0.59	0.13	1.00	0.06
$C_{L_{\delta_e}}$	0.09	0.11	-0.02	-0.20	0.13	0.01	-0.08	0.07	0.56	0.06	1.00

Table 10.3: Parameter correlation matrix for identification using *Van Ingen + Dynamic stalls* dataset

	$\tau_{1,ss}$	$\tau_{2,ss}$	$a_{1,ss}$	α^*_{ss}	$a_{1,w}$	α^*_w	C_{L_0}	$C_{L_{\alpha,ss}}$	$C_{L_{\alpha,w}}$	$C_{L_{q^*}}$	$C_{L_{\delta_e}}$
$\tau_{1,ss}$	1.00	0.06	0.21	0.10	0.15	0.03	0.16	-0.35	0.33	0.06	-0.08
$\tau_{2,ss}$	0.06	1.00	-0.07	-0.35	0.09	0.36	0.09	-0.27	0.40	0.51	0.16
$a_{1,ss}$	0.21	-0.07	1.00	0.36	-0.08	0.03	0.07	0.04	-0.07	0.05	0.13
α^*_{ss}	0.10	-0.35	0.36	1.00	-0.04	0.04	0.17	-0.10	-0.26	-0.03	-0.21
$a_{1,w}$	0.15	0.09	-0.08	-0.04	1.00	0.30	0.00	-0.05	0.14	0.29	0.10
α^*_w	0.03	0.36	0.03	0.04	0.30	1.00	0.07	-0.16	0.28	0.46	0.21
C_{L_0}	0.16	0.09	0.07	0.17	0.00	0.07	1.00	-0.87	-0.27	0.58	-0.12
$C_{L_{\alpha,ss}}$	-0.35	-0.27	0.04	-0.10	-0.05	-0.16	-0.87	1.00	-0.11	-0.61	0.23
$C_{L_{\alpha,w}}$	0.33	0.40	-0.07	-0.26	0.14	0.28	-0.27	-0.11	1.00	0.25	0.49
$C_{L_{q^*}}$	0.06	0.51	0.05	-0.03	0.29	0.46	0.58	-0.61	0.25	1.00	0.30
$C_{L_{\delta_e}}$	-0.08	0.16	0.13	-0.21	0.10	0.21	-0.12	0.23	0.49	0.30	1.00

10.2.2. Pitch Rate versus Angle of Attack Rate

During the first flight on October 14th, eleven flight maneuvers were performed to study the distinction between pitch rate and angle of attack rate. Five pullups, three pushovers, and three phugoids were performed. Using the MATLAB function corrplot[1] plots of the correlation were generated, these are presented in Fig. 10.1.

From the figure, it is immediately clear that all three methods significantly reduce the correlation between q and $\dot{\alpha}$. This analysis shows, however, that the correlation is lowest for the pullup maneuver. This is most likely attributed to the ease of performing this maneuver for the pilots. However, no further analysis has been performed into the proficiency of the pilots.

When combining the data, problems are observed. It turns out that the excursions made during the defined maneuvers are not large enough to eliminate the highly correlated excursions made during stall maneuvers. This is visible in Fig. 10.2. Although the correlation has been reduced from 0.82 to 0.71, it is an avenue that requires more research to give a useful contribution to stall modeling.

[1] `https://nl.mathworks.com/help/econ/corrplot.html`

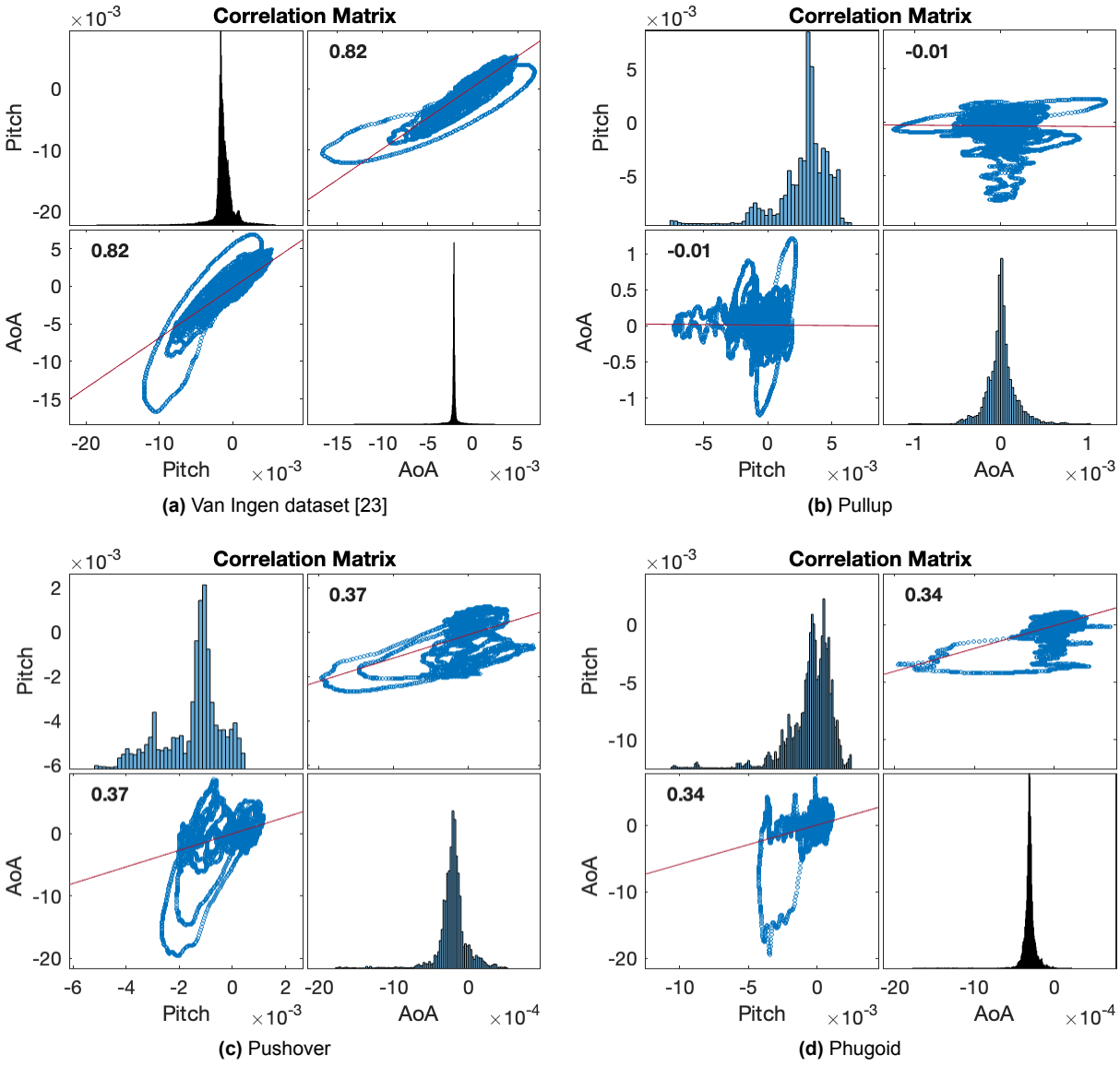

(a) Van Ingen dataset [23]

(b) Pullup

(c) Pushover

(d) Phugoid

Figure 10.1: Correlation plots for the pitch rate and angle of attack rate for different datasets, with different maneuvers.

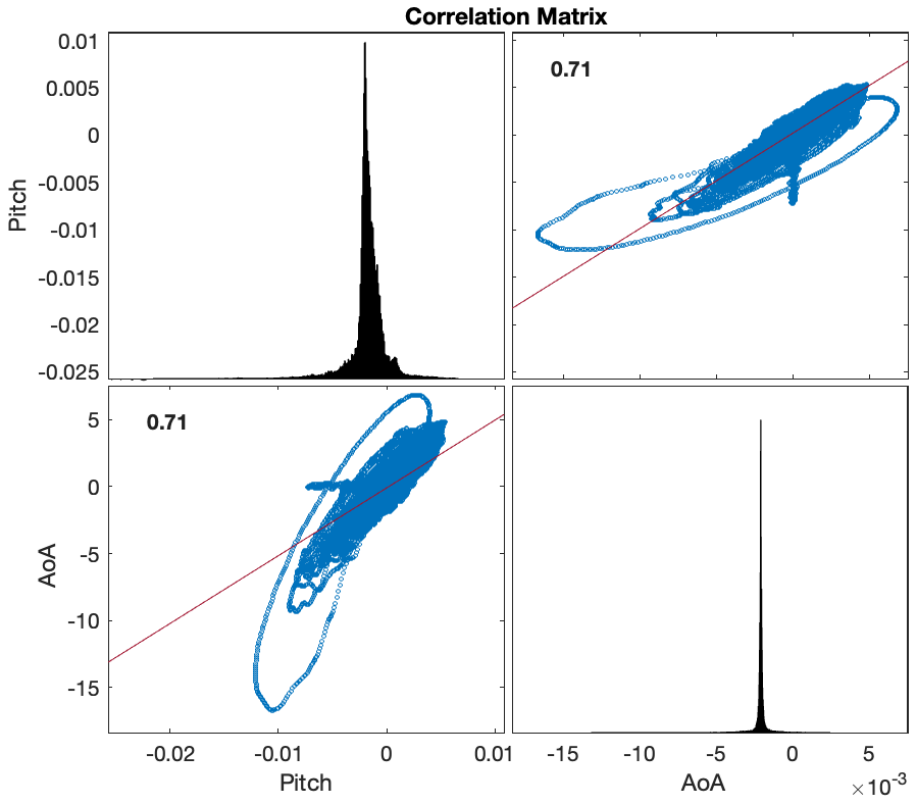

Figure 10.2: Correlation plot for the ensemble of Van Ingen dataset, pullup, pushover and phugoid maneuvers.

Part IV

Closure

11

Conclusions & Recommendations

11.1. Conclusions

To conclude this research, a reflection on the original research objective and questions is performed. The research objective posed in Chapter 3 is repeated below for convenience.

Research Objective

To improve the Citation II aerodynamic stall model accuracy by developing an improved nonlinear system identification routine.

To reach the objective six research questions were defined. Leading up to the objective, an answer to these questions is provided in this section.

Research Question 1

What are the limitations and potential improvements of the current nonlinear system identification routine used for aerodynamic stall modeling?

In Chapter 8, the limitations of the previous nonlinear system identification routine have been determined. Three main limiting factors were identified. First, the method lacked a proper definition of the parameter covariance matrix. Due to this limitation, the previous method had to rely on a bootstrap method to create an estimate of the covariance matrix. However, this was based on the assumption that the parameter estimate for each maneuver had the same statistical properties. The second limitation relates to the linear parameters present in the model. Using least squares theory, optimal estimates can be found for these parameters. The fact that these optimal estimates do not align with the results of the nonlinear estimation method directly indicates that the nonlinear estimation method has difficulty converging. The last and perhaps most significant limitation relates to the method's runtime, which was found to be one day. This has been a long-standing bottleneck in the stall identification pipeline. This has limited experimentation and innovation of stall models.

Research Question 2

How can separable nonlinear least squares eliminate the limitations imposed by the current nonlinear system identification routine?

The idea of SNLS stems directly from the model structure, common to most stall models proposed at the stall task force in Delft. The structure extends the regular linear aerodynamic models with underlying separation equations that introduce nonlinearities. SNLS makes use of the linear part of the model to reduce the complexity of optimization. This is achieved by using the OLS estimate of the linear parameters. The optimality of the linear parameters is thus built into the algorithm, solving the second limitation. Through practical experience with the new method, it is observed that the runtime is significantly reduced,

taking less than a minute on average. This is seen as proof that the third limitation is reduced. Lastly, methods have been developed for SNLS to determine the parameter covariance, removing the first limitation.

Research Question 3

How does the output of the new nonlinear system identification routine compare to that of the current routine?

In Chapter 9, an early analysis is performed on the lift model. It is here that a direct comparison is made between the results of the previous nonlinear parameter optimization method and SNLS. Compared with Van Ingen [23], the same dataset and model structure are chosen. When SNLS is used a 16% decrease in training MSE is achieved. Furthermore, the minimum R^2 value is increased from 0.71 to 0.85, which points to better consistency across maneuvers. In Part II, the developed SNLS method is applied to find an improved longitudinal stall model. Again, it is observed that the SNLS method provides more consistent results. These two cases are good indications that the SNLS method is more efficient and robust.

Research Question 4

What new model components can be identified using the new nonlinear system identification routine?

This research has focused on the identification of a new longitudinal stall model. During the study, multiple new model components have been found. First, a new stall parameter was introduced to model the local effects of the stall strip. This extra stall parameter distinguishes well between an abrupt low angle of attack stall, characteristic of the stall strip, and a subtle high angle of attack full-wing stall. Furthermore, additional elevator deflection and pitch rate contributions were uncovered for the lift model. The drag model has incorporated a new lift-induced drag term. Lastly, the pitch moment was completely overhauled. Pitch rate contributions are added, an alternative method to model the elevator control effectiveness is presented, and a new internal model for the aircraft center of pressure is added.

Research Question 5

What additional flight test data is required to enhance the Citation II aerodynamic stall model?

During this research, two flight tests have been performed. For these flights the goals were to lower correlations in the current dataset. Firstly, a high correlation existed between τ_1 and τ_2 parameter estimates. To overcome this deficiency the **Dynamic Stall** and **Deep Dynamic Stall** maneuvers were designed. These were very effective and reduced the correlation from 0.73 to 0.06. The second correlation that was aimed to be reduced is that between the pitch rate and angle of attack rate. To achieve this, three maneuvers were selected: **Pullup**, **Pushover**, and **Phugoid**. Although all three maneuvers proved to reduce the correlation during the maneuver, it was observed that the magnitude of the excursions was too low in comparison to the magnitudes observed in the stall. For this reason, the separation of pitch rate and angle of attack rate was unsuccessful.

Research Question 6

How does the identified stall model compare to the current stall models?

The result of this thesis is a new longitudinal stall model for the Cessna Citation II. Enabled by improved nonlinear parameter estimation methods, new model structure elements, and additional flight data. These factors culminated in consistent reductions of the MSE for all models, C_L, C_D and C_m, as well as derived coefficients, C_X and C_Z, summarized in Table 11.1. Additionally, the consistency of the models is improved by increasing the minimum R^2 value. With that in mind, it can be stated that the research objective is met.

Table 11.1: Summary of the global training and validation model statistics. Green indicates better results in this work, orange means no difference and red indicates worse results. Table adapted from the paper.

Model		Training Data				Validation Data			
		MSE	R^2	min(R^2)	max R^2)	*MSE*	R^2	min(R^2)	max R^2)
This work	C_L	3.55×10^{-3}	0.89	0.82	0.95	3.38×10^{-3}	0.91	0.81	0.95
	C_D	1.68×10^{-4}	0.91	−1.31	0.96	1.75×10^{-4}	0.86	0.75	0.92
	C_X	1.20×10^{-4}	0.94	0.79	0.99	1.53×10^{-4}	0.92	0.66	0.97
	C_Z	3.60×10^{-3}	0.89	0.82	0.95	3.38×10^{-3}	0.91	0.81	0.95
	C_m	1.43×10^{-4}	0.79	0.16	0.92	1.86×10^{-4}	0.71	0.18	0.88
Van Ingen [54]	C_L	5.23×10^{-3}	0.84	0.63	0.96	4.09×10^{-3}	0.89	0.59	0.96
	C_D	2.35×10^{-4}	0.87	−1.53	0.95	1.90×10^{-4}	0.85	0.76	0.91
	C_X	4.13×10^{-4}	0.79	−2.86	0.98	1.98×10^{-4}	0.89	0.60	0.97
	C_Z	5.04×10^{-3}	0.85	0.66	0.96	4.07×10^{-3}	0.89	0.57	0.96
	C_m	1.96×10^{-4}	0.72	−0.37	0.89	2.52×10^{-4}	0.61	−0.03	0.88

11.2. Recommendations

Using the knowledge built during this project, recommendations can be given for future work. The recommendations can be roughly divided into four categories. First, relating to the nonlinear parameter estimation methodology:

- The SNLS method provides effective results within a short time. This opens up the opportunity to develop a framework for the exploration of different model structures. This can be done in multiple ways, such as exhaustive search methods or genetic algorithms.
- The advancements in nonlinear parameter estimation also enable the method to simultaneously use data from different aerodynamic coefficients. This should help with the consistency of the estimation.
- The improved nonlinear parameter estimation method is able to process larger data sets simultaneously, ensuring an optimal model across multiple maneuvers. This is seen as a potential solution for merging the stall models with nominal models by combining stall and non-stall data into one identification routine.
- More research should be performed to quantify the uncertainty of the model. An initial sensitivity study has been initiated using the parameter variance. Further work should propagate model uncertainties to the output to determine confidence bands.
- Accuracy of the model may also be judged by the ability to predict aircraft states. Applying the aerodynamic model in forward simulation may give further insights into model performance.

Moving on from the system identification methodology. The next category of recommendations relates to the structure of models that are used:

- This work has shown that two stall parameters are effective. This is based on a hypothesis, one stall parameter relates to the stall strips and one to the rest of the wing. Future work should investigate the validity of this hypothesis, by mapping the flow field around the wings using tufts.
- The effect of stall strips on stall behavior is not well documented in the literature. It would be interesting to study the effects of stall strips on 2D wing sections in the wind tunnel.
- An assumption has been made that Kirchhoff's theory of flow separation is able to model a leading-edge stall at the stall strips. It has shown effective in modeling, but more research must be performed to understand the leading edge stall behavior.
- An initial assumption is made for the model structure of the static separation characteristics. It is advised to explore different model structures.
- A model for the center of pressure has been created. However, the model includes a term relating to the center of gravity. This added term should be understood better and if possible removed.

- The current model, models the forces and moments at the center of gravity. However, this shifts during the flight. For aerodynamic modeling, it might make sense to create a model around a fixed point on the aircraft. This is a possible new route for exploration.

Next, recommendations for a new identification dataset are given. In part, the existing database of flight tests should be explored for the necessary data. However, these could also be potential avenues for new flight test campaigns:

- Continue research into the angle of attack rate effects and suitable methods for the identification of them during stall.
- A high correlation between the angle of attack and elevator deflection is observed. New data is required to remove that correlation.
- A high correlation between bias and lift curve slope is observed. Further research is required to understand where this comes from and how this can be reduced.

Lastly, some recommendations that did not fit in any of the above categories:

- It is advised to revisit the engine and mass model as these are likely introducing undesired effects to the aerodynamic model.
- It is advised to research the effectiveness of using DADC data for the dynamic pressure.
- The effectiveness of the model must be tested with pilot-in-the-loop experiments. These tests may research if parameter variances are low enough through just-noticible-difference experiments. Furthermore, they might shed light on the necessity of adding complexity to the model.

References

[1] Mike A. Bromfield et al. “Loss of Control In Flight – time to re-define?” In: *AIAA Aviation 2019 Forum*. Dallas, Texas: AIAA, June 2019. DOI: 10.2514/6.2019-3612.

[2] *A Statistical Analysis of Commercial Aviation Accidents 1958-2023*. Tech. rep. Airbus, SAS, X00D17008863, 2024.

[3] *Statistical Summary of Commercial Jet Airplane Accidents*. Tech. rep. Boeing, Co, 326909, 2023.

[4] *Loss of Control In-Flight Accident Analysis Report*. Tech. rep. International Air Transport Association, 2019.

[5] Christine M. Belcastro et al. “Preliminary Analysis of Aircraft Loss of Control Accidents: Worst Case Precursor Combinations and Temporal Sequencing”. In: *AIAA Guidance, Navigation, and Control Conference*. National Harbor, Maryland: AIAA, Jan. 2014. DOI: 10.2514/6.2014-0612.

[6] Steven R Jacobson. “Aircraft Loss of Control Causal Factors and Mitigation Challenges”. In: *AIAA Guidance, Navigation, and Control Conference*. Toronto, Ontario, Canada: AIAA, Aug. 2010. DOI: 10.2514/6.2010-8007.

[7] A. A. Lambregts et al. “Airplane Upsets: Old Problem, New Issues”. In: *AIAA Modeling and Simulation Technologies Conference and Exhibit*. Honolulu, Hawaii: AIAA, Aug. 2008. DOI: 10.2514/6.2008-6867.

[8] Dennis Crider. “Accident Lessons for Stall Upset Recovery Training”. In: *AIAA Guidance, Navigation, and Control Conference*. Toronto, Ontario, Canada: AIAA, Aug. 2010. DOI: 10.2514/6.2010-8003.

[9] Sunjoo Advani et al. “Upset Prevention and Recovery Training in Flight Simulators”. In: *AIAA Modeling and Simulation Technologies Conference*. Portland, Oregon: AIAA, Aug. 2011. DOI: 10.2514/6.2011-6698.

[10] *Manual on Aeroplane Upset Prevention and Recovery Training*. Tech. rep. International Civil Aviation Organization, Doc 10011 AN/506, 2014.

[11] *Stall Prevention and Recovery Training*. Tech. rep. Federal Aviation Administration, AC 120-109A, 2017.

[12] *Annex I to ED Decision 2019/005/R*. Tech. rep. European Union Aviation Safety Agency, 2019.

[13] Sunjoo K. Advani et al. “Global Implementation of Upset Prevention & Recovery Training”. In: *AIAA Modeling and Simulation Technologies Conference*. San Diego, California, USA: AIAA, Jan. 2016. DOI: 10.2514/6.2016-1430.

[14] N. B. Abramov et al. “Aerodynamic Modeling for Poststall Flight Simulation of a Transport Airplane”. In: *Journal of Aircraft* 56.4 (July 2019), pp. 1427–1440. DOI: 10.2514/1.C034790.

[15] D. Fischenberg. “Identification of an unsteady aerodynamic stall model from flight test data”. In: *20th Atmospheric Flight Mechanics Conference*. Baltimore, MD: AIAA, Aug. 1995, pp. 138–146. DOI: 10.2514/6.1995-3438.

[16] J. Singh et al. “Flight determination of configurational effects on aircraft stall behavior”. In: *21st Atmospheric Flight Mechanics Conference*. San Diego, CA: AIAA, July 1996, pp. 657–665. DOI: 10.2514/6.1996-3441.

[17] J. Singh et al. “Identification of lateral-directional behavior in stall from flight data”. In: *Journal of Aircraft* 33.3 (May 1996), pp. 627–630. DOI: 10.2514/3.46993.

[18] D Fischenberg et al. “Identification of Aircraft Stall Behavior from Flight Test Data”. In: *RTO Meeting Proceedings 11, System Identification for Integrated Aircraft Development and Flight Testing*.

Madrid, Spain: NATO, Research and Technology Organization, 1998, 17(1)–17(8). DOI: 10.14339/RTO-MP-011.

[19] Eugene A. Morelli et al. “Global Aerodynamic Modeling for Stall/Upset Recovery Training Using Efficient Piloted Flight Test Techniques”. In: *AIAA Modeling and Simulation Technologies (MST) Conference*. Boston, MA: AIAA, Aug. 2013. DOI: 10.2514/6.2013-4976.

[20] Joaquim N. Dias. “Nonlinear Lifting-Line Algorithm for Unsteady and Post-stall Conditions”. In: *34th AIAA Applied Aerodynamics Conference*. Washington, D.C.: AIAA, June 2016. DOI: 10.2514/6.2016-4164.

[21] Joaquim N. Dias. “Stall Model Identification Using Flight Path Reconstruction of Multiple Maneuvers”. In: *AIAA Aviation 2023 Forum*. San Diego, CA: AIAA, June 2023. DOI: 10.2514/6.2023-3781.

[22] L J Van Horssen. “Aerodynamic Stall Modeling for the Cessna Citation II”. In: Delft, the Netherlands: M.Sc. Thesis, Control & Operations Department, Faculty of Aerospace Engineering, Delft University of Technology, 2016. URL: http://repository.tudelft.nl/.

[23] Joost Van Ingen. “Dynamic Stall Modeling for the Cessna Citation II”. In: Delft, the Netherlands: M.Sc. Thesis, Control & Operations Department, Faculty of Aerospace Engineering, Delft University of Technology, 2017. URL: http://repository.tudelft.nl/.

[24] Sven Marschalk. “Stall Buffet Modeling using Swept Wing Flight Test Data”. In: Delft, the Netherlands: M.Sc. Thesis, Control & Operations Department, Faculty of Aerospace Engineering, Delft University of Technology, 2019. URL: http://repository.tudelft.nl/.

[25] Peter C Luteijn. “Towards a Stall Model for the Fokker 100”. In: Delft, the Netherlands: M.Sc. Thesis, Control & Operations Department, Faculty of Aerospace Engineering, Delft University of Technology, 2020. URL: http://repository.tudelft.nl/.

[26] E H P De Meester. “Towards an Asymmetric Stall Model for the Fokker 100”. In: Delft, the Netherlands: M.Sc. Thesis, Control & Operations Department, Faculty of Aerospace Engineering, Delft University of Technology, 2021. URL: http://repository.tudelft.nl/.

[27] A Delfosse. “Asymmetric Stall and Control Effectiveness Reduction Modeling for the Cessna Citation II”. In: Delft, the Netherlands: M.Sc. Thesis, Control & Operations Department, Faculty of Aerospace Engineering, Delft University of Technology, 2021. URL: http://repository.tudelft.nl/.

[28] P A R Brill. “Improving Stall Model Accuracy through Optimal Data Slicing by Analyzing Kirch-hoff Stall Parameter Estimate Behaviour”. In: Delft, the Netherlands: M.Sc. Thesis, Control & Operations Department, Faculty of Aerospace Engineering, Delft University of Technology, 2023. URL: http://repository.tudelft.nl/.

[29] D De Fuijk. “Asymmetric Cessna Citation II Stall Model Identification using a Roll Moment-based Kirchhoff Method”. In: Delft, the Netherlands: M.Sc. Thesis, Control & Operations Department, Faculty of Aerospace Engineering, Delft University of Technology, 2023. URL: http://repository.tudelft.nl/.

[30] Dennis Crider. “Need for Upset Recovery Training”. In: *AIAA Modeling and Simulation Technologies Conference and Exhibit*. Reston, Virigina: AIAA, Aug. 2008. DOI: 10.2514/6.2008-6864. URL: https://arc.aiaa.org/doi/10.2514/6.2008-6864.

[31] D. A. Crider. “Upset recovery training: Lessons from accidents and incidents”. In: *The Aeronautical Journal* 114.1160 (Oct. 2010), pp. 629–636. DOI: 10.1017/S0001924000004103. URL: https://www.cambridge.org/core/product/identifier/S0001924000004103/type/journal_article.

[32] John D. Anderson. *Fundamentals of Aerodynamics*. 6th ed. New York, NY: McGraw-Hill Education, 2017.

[33] C J Van Wezel. “Modeling of the Nonlinear Unsteady Pitching Moment Stall Characteristics from Cessna Citation II Flight Test Data”. In: Delft, the Netherlands: M.Sc. Thesis, Control & Operations Department, Faculty of Aerospace Engineering, Delft University of Technology, 2024. URL: http://repository.tudelft.nl/..

[34] M. Goman et al. “State-space representation of aerodynamic characteristics of an aircraft at high angles of attack”. In: *Astrodynamics Conference*. AIAA, Aug. 1992. DOI: 10.2514/6.1992-4651.

[35] J. G. Leishman et al. “A Semi□Empirical Model for Dynamic Stall”. In: *Journal of the American Helicopter Society* 34.3 (July 1989), pp. 3–17. DOI: 10.4050/JAHS.34.3.3.

[36] Roelof Vos et al. “Airfoil Aerodynamics”. In: *Introduction to Transonic Aerodynamics*. Ed. by Roelof Vos et al. Dordrecht: Springer Netherlands, 2015, pp. 367–426. DOI: 10.1007/978-94-017-9747-4{_}7. URL: https://doi.org/10.1007/978-94-017-9747-4_7.

[37] Herbert Wagner. “Über die Entstehung des dynamischen Auftriebes von Tragflügeln”. In: *ZAMM □ Journal of Applied Mathematics and Mechanics / Zeitschrift für Angewandte Mathematik und Mechanik* 5.1 (1925), pp. 17–35. DOI: 10.1002/zamm.19250050103.

[38] Amanullah Choudhry et al. “An insight into the dynamic stall lift characteristics”. In: *Experimental Thermal and Fluid Science* 58 (2014), pp. 188–208. DOI: 10.1016/j.expthermflusci.2014.07.006.

[39] P.F. Melani et al. “The Beddoes-Leishman dynamic stall model: Critical aspects in implementation and calibration”. In: *Renewable and Sustainable Energy Reviews* 202 (Sept. 2024), p. 114677. DOI: 10.1016/j.rser.2024.114677.

[40] C. C. de Visser et al. “A new approach to linear regression with multivariate splines”. In: *Automatica* 45.12 (Dec. 2009), pp. 2903–2909. DOI: 10.1016/j.automatica.2009.09.017.

[41] Gene Golub et al. “Separable nonlinear least squares: the variable projection method and its applications”. In: *Inverse Problems* 19.2 (Feb. 2003), R1–R26. DOI: 10.1088/0266-5611/19/2/201.

[42] G H Golub et al. “The Differentiation of Pseudo-Inverses and Nonlinear Least Squares Problems Whose Variables Separate”. In: *SIAM Journal on Numerical Analysis* 10.2 (Apr. 1973), pp. 413–432. DOI: 10.1137/0710036.

[43] Dianne P. O’Leary et al. “Variable projection for nonlinear least squares problems”. In: *Computational Optimization and Applications* 54.3 (Apr. 2013), pp. 579–593. DOI: 10.1007/s10589-012-9492-9.

[44] Kaushik Mahata et al. “Large sample properties of separable nonlinear least squares estimators”. In: *IEEE Transactions on Signal Processing* 52.6 (June 2004), pp. 1650–1658. DOI: 10.1109/TSP.2004.827227.

[45] Adi Ben-Israel et al. *Generalized Inverses*. Ed. by Jonathan Borwein et al. 2nd ed. Springer, 2002.

[46] Jorge R. Leis et al. “The simultaneous solution and sensitivity analysis of systems described by ordinary differential equations”. In: *ACM Transactions on Mathematical Software* 14.1 (Mar. 1988), pp. 45–60. DOI: 10.1145/42288.46156. URL: https://dl.acm.org/doi/10.1145/42288.46156.

[47] V. Klein et al. *Aircraft System Identification Theory and Practice*. Tech. rep. AIAA, 2006.

[48] D. B. Owen. “The Power of Student’s t-test”. In: *Journal of the American Statistical Association* 60.309 (1965), pp. 320–333. DOI: 10.1080/01621459.1965.10480794.

[49] Ravindra V. Jategaonkar et al. *Two complementary approaches to estimate downwash lag effects from flight data*. 1991. DOI: 10.2514/3.46060.

[50] Jared A. Grauer et al. “Flight-Test techniques for quantifying pitch rate and angle-of-Attack rate dependencies”. In: *Journal of Aircraft*. Vol. 54. 6. American Institute of Aeronautics and Astronautics Inc., 2017, pp. 2367–2377. DOI: 10.2514/1.C034407.

[51] Richard E. Maine et al. “Maximum Likelihood Estimation of Translational Acceleration Derivatives from Flight Data”. In: *Journal of Aircraft* 16.10 (Oct. 1979), pp. 674–679. DOI: 10.2514/3.58588. URL: https://arc.aiaa.org/doi/10.2514/3.58588.

[52] M A Van Den Hoek. *Design, Identification and Implementation of a High-Fidelity Cessna Citation II Flight Simulation Model*. Tech. rep. 2016.

[53] C C De Visser. “Global Nonlinear Model Identification with Multivariate Splines”. PhD thesis. Delft, the Netherlands, July: Delft University of Technology, 2011.

[54] Joost B. Van Ingen et al. “Stall Model Identification of a Cessna Citation II from Flight Test Data Using Orthogonal Model Structure Selection”. In: *AIAA Scitech 2021 Forum*. AIAA, 2021. DOI: 10.2514/6.2021-1725.

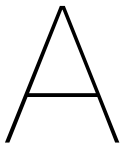

Aircraft Center of Gravity Envelope

UNIT NUMBER _____ REGISTRATION NUMBER _____ DATE _____

SERIAL NUMBER _____

CENTER-OF-GRAVITY LIMITS ENVELOPE GRAPH

AIRPLANES -0627 AND ON

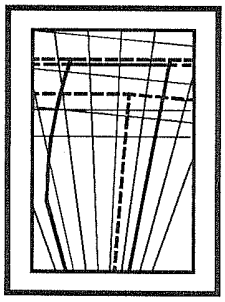

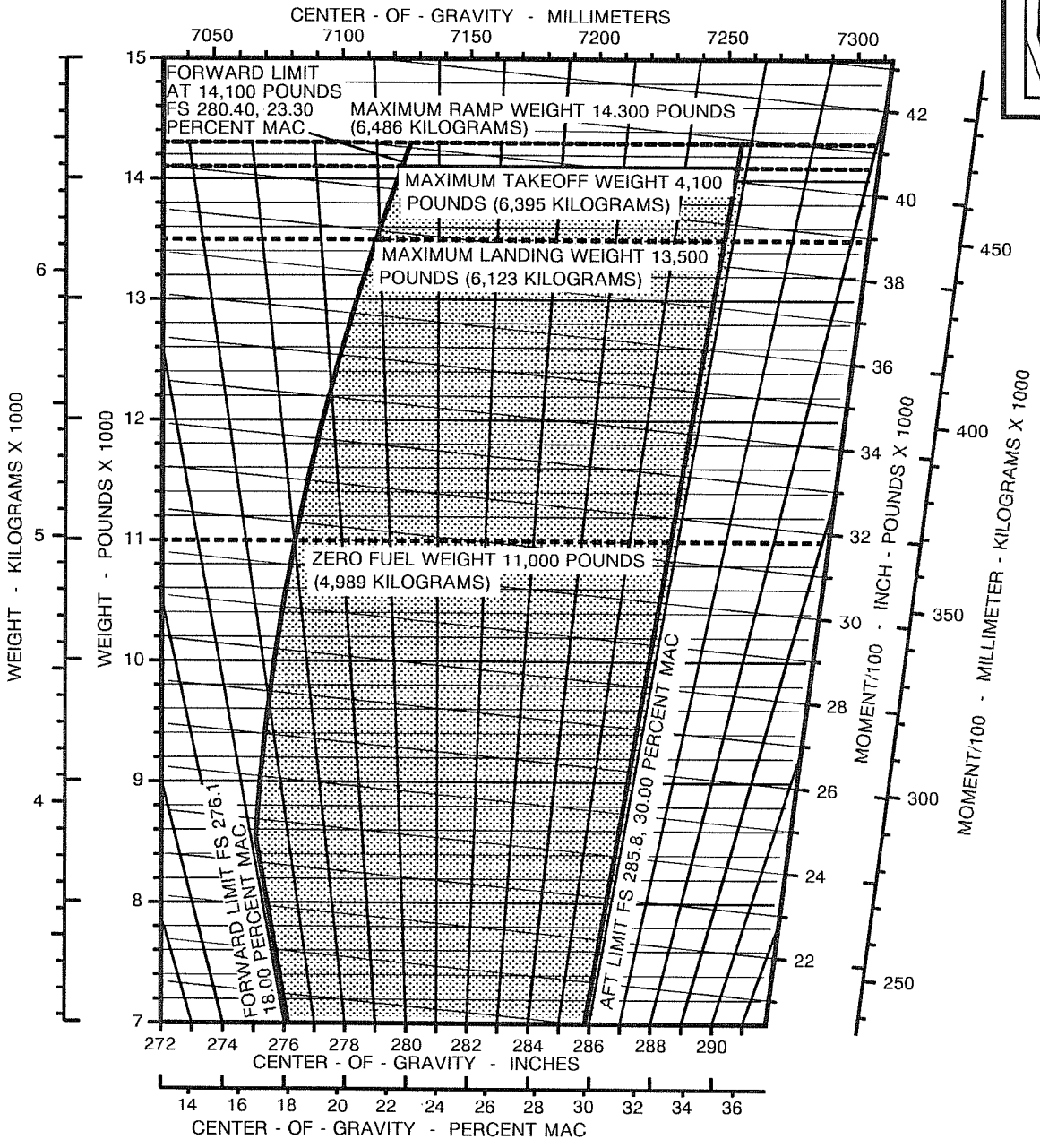

B

Aircraft Mass and Balance

Dedicated to innovation in aerospace
Continuing Airworthiness Management Organisation

MASS AND BALANCE REPORT

CAME form 1.3i

revision 3

AIRCRAFT

Registration	PH-LAB
Make	Cessna
Model	C550
Serial	550-712
TC	A22CE (FAA)

OWNER

Name	National Aerospace Laboratory
Address	Anthony Fokkerweg 2
City	Amsterdam
Postal Code	1059 CM

GENERAL DATA WEIGHING DD: 03-08-2023

Aircraft configuration:	WR-C-1017, CCR-2023-008 FTIS-FBW
Levelling means:	Longitudinal: inboard seat track. (Center level over FS206)□ Lateral: Inboard seat track at FS206
Datum point :	Reference Datum Line
Weighting point:	Jack Stand

Conditions during weighing:

Balance weights installed (Aft Bagage Compartment)		220 LBS
Cabin Seat #8	FS288	Installed
Cabin Seat #7	FS288	Installed
Cabin Seat #6	FS250	Installed
Cabin Seat #5	FS250	Installed
Cabin Seat #4	FS216	Installed
Cabin Seat #3	FS216	Installed
Cabin Seat #10	FS170	Installed
Cabin Seat #9	FS170	Installed
Weight/arm/moment		lbs/inch/lbsinch
Fuel on Board		2760
Flight Bag on board		17 inch rack

WEIGHING RECORD

Description	Scale reading	Tare	Net	Arm	Moment
L/H Main	5200	0	5200	315.5	1640600
R/H Main	5278	0	5278	315.5	1665209
Tail or nose	1447	0	1447	93.7	135583.9

Amendments to General Data

Removed items:

Description	Weight	Arm	Moment
Fuel on Board	-2760.0	285.16	-787041.6

Added items:

Description	Weight	Arm	Moment
4 Balance Plates (total of 10 plates 220LBS)	88.0	420.0	36960.0

Basic Empty Weight	**9253.0**	**290.86**	**2691311.3**

Date: 10/10/2024 Sign: Name: G.F. den Toom License no.: NLR 2010-1

VALID FOR AIRCRAFT CONFIGURATION ACCORDING CCR-2024-016

C

Flight Test Cards

TU Delft
Flight Department

FLIGHT TEST CARD

PROJECT	:	Dynamic Stall Modeling for the Cessna Citation II
TEST CARD NUMBER	:	1
SUBJECT	:	Dynamic stall maneuvers w. air data boom & angular accelerometers
REFERENCE	:	
NOTES	:	14/10/2024
EST. DURATION OF TEST POINT	:	120 seconds
HAZARD CATEGORY	:	ROUTINE / ~~LOW~~ / ~~MEDIUM~~ / ~~HIGH~~

INITIAL CONDITIONS

ALT/FL	:	FL150-FL200	ENGINE SETTING	:	As required
IAS	:	As required	FLAP SETTING	:	Clean
MACH	:	As required	LANDING GEAR	:	Up
MASS	:		OTHER	:	
C.G.	:				

EXPERIMENT PROCEDURE

Checklist:

Nr.		Maneuver	ALT/FL	Flap setting	Landing gear
1	☐	Dynamic Stall	FL150-FL200	Clean	Up
2	☐	Dynamic Stall	FL150-FL200	Clean	Up
3	☐	Dynamic Stall	FL150-FL200	Clean	Up
4	☐	Dynamic Stall	FL150-FL200	Clean	Up
5	☐	Dynamic Stall	FL150-FL200	Clean	Up
6	☐	Dynamic Stall	FL150-FL200	Clean	Up
7	☐	Dynamic Stall	FL150-FL200	Clean	Up
8	☐	Dynamic Stall	FL150-FL200	Clean	Up
9	☐	Dynamic Stall	FL150-FL200	Clean	Up
10	☐	Dynamic Stall	FL150-FL200	Clean	Up
11	☐	Pullup	FL150-FL200	Clean	Up
12	☐	Pullup	FL150-FL200	Clean	Up
13	☐	Pullup	FL150-FL200	Clean	Up
14	☐	Pullup	FL150-FL200	Clean	Up
15	☐	Pullup	FL150-FL200	Clean	Up
16	☐	Pushover	FL150-FL200	Clean	Up
17	☐	Pushover	FL150-FL200	Clean	Up
18	☐	Pushover	FL150-FL200	Clean	Up
19	☐	Pushover	FL150-FL200	Clean	Up
20	☐	Pushover	FL150-FL200	Clean	Up
...	☐	Dynamic Stall	FL150-FL200	Clean	Up
21	☐	Phugoid 120kts	FL150-FL200	Clean	Up
22	☐	Phugoid 120kts	FL150-FL200	Clean	Up
23	☐	Phugoid 160kts	FL150-FL200	Clean	Up
24	☐	Phugoid 160kts	FL150-FL200	Clean	Up

Note 1: If time permits, repeat dynamic stall maneuver.
Note 2: See test card 2 and 3 for procedures for chosen maneuvers.

TU Delft
Flight Department

FLIGHT TEST CARD

PROJECT	:	Dynamic Stall Modeling for the Cessna Citation II
TEST CARD NUMBER	:	2
SUBJECT	:	Dynamic stall maneuvers w. air data boom & angular accelerometers
REFERENCE	:	
NOTES	:	14/10/2024
EST. DURATION OF TEST POINT	:	120 seconds
HAZARD CATEGORY	:	ROUTINE / ~~LOW~~ / ~~MEDIUM~~ / ~~HIGH~~

INITIAL CONDITIONS

ALT/FL	:	FL150-FL200	ENGINE SETTING	:	As required
IAS	:	As required	FLAP SETTING	:	Clean
MACH	:	As required	LANDING GEAR	:	Up
MASS	:		OTHER	:	
C.G.	:				

EXPERIMENT PROCEDURE	**REC. NRS**
Dynamic stall procedure: 1. Establish trimmed level flight 2. Increase AoA with ~X* deg/sec 3. Apply sequential elevator/aileron/rudder doublets 4. When at stall boundary, apply oscillating elevator inputs 5. Maintain stall for "X"** seconds 6. Recover * Finetune to achieve good entry into stall ** As long as possible	1-10 + left over time
Phugoid procedure: 1. Establish trimmed level flight at 120-160 kts 2. Push/Pull elevator to establish off-trim airspeed 3. Make as large as possible deviations	21-24

TU Delft
Flight Department

FLIGHT TEST CARD

PROJECT	:	Dynamic Stall Modeling for the Cessna Citation II
TEST CARD NUMBER	:	3
SUBJECT	:	Dynamic stall maneuvers w. air data boom & angular accelerometers
REFERENCE	:	
NOTES	:	14/10/2024
EST. DURATION OF TEST POINT	:	120 seconds
HAZARD CATEGORY	:	ROUTINE / ~~LOW~~ / ~~MEDIUM~~ / ~~HIGH~~

INITIAL CONDITIONS

ALT/FL	:	FL150-FL200	ENGINE SETTING	:	As required
IAS	:	As required	FLAP SETTING	:	Clean
MACH	:	As required	LANDING GEAR	:	Up
MASS	:		OTHER	:	
C.G.	:				

EXPERIMENT PROCEDURE	**REC. NRS**
Pullup maneuver procedure: 1. Establish trimmed level flight at 120-160 kts 2. Set power to XX%* 3. Pitch down to -XX** deg pitch attitude 4. Apply elevator input to maintain 6*** deg AoA 5. Recover when pitch attitude reaches XX** deg * Set power to throttle percentage lower/higher than trim ** Set pitch range as large as possible *** Value from Grauer (2017), tune for Citation; assumed to be near the trim AoA	11-15
Pushover maneuver procedure: 1. Establish trimmed level flight at 120-160 kts 2. Set power to XX%* 3. Pitch up to XX** deg pitch attitude 4. Apply elevator input to maintain 4.5*** deg AoA 5. Recover when pitch attitude reaches -XX** deg * Set power to throttle percentage lower/higher than trim ** Set pitch range as large as possible *** Value from Grauer (2017), tune for Citation; assumed to be near the trim AoA	16-20

TU Delft
Flight Department

FLIGHT TEST CARD

PROJECT	:	Dynamic Stall Modeling for the Cessna Citation II
TEST CARD NUMBER	:	1
SUBJECT	:	Dynamic stall maneuvers w. air data boom & angular accelerometers
REFERENCE	:	
NOTES	:	23/10/2024
EST. DURATION OF TEST POINT	:	120 seconds
HAZARD CATEGORY	:	ROUTINE / ~~LOW~~ / ~~MEDIUM~~ / ~~HIGH~~

INITIAL CONDITIONS

ALT/FL	:	FL150-FL200	ENGINE SETTING	:	As required
IAS	:	As required	FLAP SETTING	:	Clean
MACH	:	As required	LANDING GEAR	:	Up
MASS	:		OTHER	:	
C.G.	:				

EXPERIMENT PROCEDURE

Checklist:

Nr.		Maneuver	ALT/FL	Flap setting	Landing gear
1	☐	Dynamic Stall	FL180-FL190	Clean	Up
2	☐	Dynamic Stall	FL180-FL190	Clean	Up
3	☐	Dynamic Stall	FL180-FL190	Clean	Up
4	☐	Dynamic Stall	FL180-FL190	Clean	Up
5	☐	Dynamic Stall	FL180-FL190	Clean	Up
6	☐	Pullup	FL180-FL190	Clean	Up
7	☐	Pullup	FL180-FL190	Clean	Up
8	☐	Pullup	FL180-FL190	Clean	Up
9	☐	Pullup	FL180-FL190	Clean	Up
10	☐	Pullup	FL180-FL190	Clean	Up
11	☐	Deep Dynamic Stall	FL180-FL190	Clean	Up
12	☐	Deep Dynamic Stall	FL180-FL190	Clean	Up
13	☐	Deep Dynamic Stall	FL180-FL190	Clean	Up
14	☐	Deep Dynamic Stall	FL180-FL190	Clean	Up
15	☐	Deep Dynamic Stall	FL180-FL190	Clean	Up
16	☐	Dynamic Stall	FL180-FL190	Clean	Up
17	☐	Deep Dynamic Stall	FL150-FL200	Clean	Up
18	☐	Dynamic Stall	FL150-FL200	Clean	Up
19	☐	Deep Dynamic Stall	FL150-FL200	Clean	Up
20	☐	Dynamic Stall	FL150-FL200	Clean	Up
21	☐	Deep Dynamic Stall	FL150-FL200	Clean	Up
22	☐	Dynamic Stall	FL150-FL200	Clean	Up
23	☐	Deep Dynamic Stall	FL150-FL200	Clean	Up
24	☐	Dynamic Stall	FL150-FL200	Clean	Up
...					

Note 1: If time permits, repeat (deep) dynamic stall maneuver.
Note 2: See test card 2 for procedures for chosen maneuvers.

TU Delft
Flight Department

FLIGHT TEST CARD

PROJECT	:	Dynamic Stall Modeling for the Cessna Citation II
TEST CARD NUMBER	:	2
SUBJECT	:	Dynamic stall maneuvers w. air data boom & angular accelerometers
REFERENCE	:	
NOTES	:	23/10/2024
EST. DURATION OF TEST POINT	:	120 seconds
HAZARD CATEGORY	:	ROUTINE / ~~LOW~~ / ~~MEDIUM~~ / ~~HIGH~~

INITIAL CONDITIONS

ALT/FL	:	FL150-FL200	ENGINE SETTING	:	As required
IAS	:	As required	FLAP SETTING	:	Clean
MACH	:	As required	LANDING GEAR	:	Up
MASS	:		OTHER	:	
C.G.	:				

EXPERIMENT PROCEDURE	**REC. NRS**
Dynamic stall procedure: 1. Establish trimmed level flight 2. Smoothly increase angle of attack 3. Apply sequential elevator/aileron/rudder steps 4. When at stall boundary, apply oscillating elevator inputs 5. Repeat entry into stall until altitude or attitude require recovery 6. Recover	1-5, 16, 18, 20, 22, 24, ...
Deep dynamic stall procedure: 1. Establish trimmed level flight 2. Smoothly increase angle of attack 3. Apply sequential elevator/aileron/rudder steps 4. Hold stall with increasing angle of attack 5. Give oscillating elevator inputs around 20 degrees AoA 6. Recover	11-15, 17, 19, 21, 23, ...
Pullup maneuver procedure: 1. Establish trimmed level flight at 120-160 kts 2. Pitch down to low pitch attitude 3. Smoothly pitch up while maintaining constant AoA 4. Recover when pitch attitude becomes too high	6-10